Hierarchical TiO$_2$ Nanostructures Based on TiO$_2$ Nanotube Arrays for Superhydrophobic Coatings and Photocatalysts

By

Arezoo Hosseini

A thesis submitted in partial of fulfillment of the requirements of the degree of

Master of Science

In

Photonics and Plasmas

Department of Electrical and Computer Engineering

University of Alberta

Abstract

n-type, wide bandgap titanium dioxide (TiO$_2$) nanostructures have a great number of engineering applications such as electron transport layers in solar cells and light emitting diodes, photocatalysts, filtration membranes, biomedical implants, drug eluting coatings, superhydrophobic coatings, self-cleaning coatings and chemical sensors. The high surface area ordered architecture and vertical orientation of TiO$_2$ nanotube arrays (TNTAs) and TiO$_2$ nanowire arrays (TNWAs) are particularly attractive characteristics for use in the aforementioned applications. Several of these applications would benefit from a hierarchical nano-architecture wherein at least two size scales are important. The work described in this thesis was directed towards the achievement of three different types of hierarchical nanostructures: (i) Filamentary TiO$_2$ nanowires grown on TiO$_2$ nanotubes (ii) TiO$_2$ nanotubes grown in solid electrolytes containing anodically formed macropores and tube walls with mesoscopic surface roughness, and (iii) PbS quantum dots decorated on TiO$_2$ nanotubes. These nanostructures are either fabricated as thin films on native and/or non-native substrates or as membranes based on the nature of the application. TNTAs and TNWAs are fabricated by electrochemical anodization and solvothermal growth methods respectively.

In the first part of this thesis, the novel hierarchical structure of TNTAs/TNWAs was fabricated by decorating rutile phase TiO$_2$ NWAs in and on the top of anatase phase TiO$_2$ NTAs prepared by anodic oxidation of Ti foil. Later the surface was modified by means of self-assembled monolayers (SAM) of ODPA, and the resultant structure presented superhydrophobicity with exceptionally high contact angle (CA≈180°).

The second part of this thesis presents the facile, compact and novel fabrication of TiO_2 nanotube arrays (TNTAs) by a fluoride-free solid-state anodization process using $LiClO_4$ containing solid polymeric electrolyte. The prepared TNTAs by using the less toxic inorganic salts exhibited comparable morphological and crystalline feature as for TiO_2 nanotubes grown in a solution-based electrolyte. The resulting nanotubes were tested for photoelectrochemical water splitting and confirm the viability of solid-state anodization process for future applications.

The last phase of the thesis focuses on the PbS quantum dot growth on different nanostructures of TiO_2 by the SILAR method. The electronic properties of the interface were studied using photocatalytic dye degradation as a model reaction to evaluate interfacial charge separation. The photocatalytic behavior of fabricated heterojunction consisting of TiO_2 nanotubes decorated with PbS quantum dots was studied by observing the degradation of rhodamine B and crystal violet as a function of time under visible light illumination.

Preface

This Master thesis includes the result of my research, which is carried out at University of Alberta, Department of Electrical and Computer Engineering. Certainly, this research would not go further without the non-stop help of Professor Karthik Shankar, who supervised me during this period. I also thank Dr. Pawan Kumar who co-supervised my thesis and helped me in the last year of my master studies.

Each chapter of this paper-based thesis is either published or prepared as a manuscript draft for submission to a journal. Results of the research presented in Chapter 2 were presented as a poster at the ATUMS annual meeting, Jasper, 12-17 November 2017and at Photonics North, Montreal, June 2012 respectively. A more detailed manuscript of this study titled, "*TiO$_2$ Nanotube-Seeded TiO$_2$ Nanowires: Hierarchical Structures for Stable Wetting & Antifouling Studies*" has been generated containing Arezoo Hosseini as first author.

Chapter 3 is published as A. Hosseini, P. Kumar, N. Mahdi, Y. Zhang, and K. Shankar, "*All-Solid-State formation of titania nanotube arrays and their application in photoelectrochemical water splitting*", Journal of Materials 2018. Chapter 4 is a manuscript draft titled "*Investigation of PbS quantum dot thin films grown by SILAR method on TiO$_2$ nanotubes for photocatalytic dye degradation*". The KPFM measurements in this chapter are carried out by Dr. Ankur Goswami.

"The primary objective of science and technology is to create a society where people can have healthy, comfortable and long lives. The crucial thing in science and technology is to develop a new concept that can be applied to actual products and services, and these new products and services will eventually make people happy"

Akira Fujishima

Acknowledgements

I am grateful to all members of my family for their continual encouragement and support, understanding and unconditional love in every stage of the entire of my life. Finally, I

want to dedicate my sincerest gratitude to my husband for his continual love and support. It would not be possible for me to achieve this goal without his patience, understanding and unconditional support.

Table of Contents

List of Figures

List of Abbreviations and Symbols

Abbreviation	Description
TiO_2	Titanium Oxide
Ti	Titanium
FTO	Florine-doped Tin Oxide
PbS	Lead Sulfide
SAED	Selected Area Electron Diffraction
HRTEM	High Resolution Transmission Electron Microscope
ABPC	Applied Bias Photoconversion Efficiency
ODPA	Octadecylphosphonic Acid
PEC	Photoelectrochemical
SAM	Self-Assembled Monolayer
NP	Nanoparticle
ED	Electrodeposition
WF	Work Function
WCA	Water Contact Angle
SEM	Scanning Electron Microscopy
CVD	Chemical Vapor Deposition
PVD	Physical Vapor Deposition
TNTAs	Titanium Oxide Nanotube Arrays
ALD	Atomic Layer Deposition
DC	Direct Current
TNWAs	Titanium Oxide Nanowire Arrays
DSSC	Dye-Sensitized Solar Cells
DI	De-ionized
HCL	Hydrochloric Acid
Ti-Bu	Titanium (IV) Butoxide
XRD	X-Ray Diffraction
UV-Vis	Ultraviolet-Visible
DR UV-Vis	Diffuse Reflectance UV-Vis
DRIFTS	Diffuse Reflectance Infrared Fourier Transform Spectroscopy
PbI_2	Lead (II) iodide
Na_2S	Sodium Sulfide
NH_4F	Ammonium Fluoride
MeOH	Methanol
FE-SEM	Field Emission Scanning Electron Microscope
Cut-off Energy	$E_{cut-off}$
AOPs	Advanced Oxidation Process
VB	Valence Band
PVA	Polyvinyl Alcohol
PVP	Polyvinyl Pyrrolidone
$LiClO_4$	Lithium Perchlorate
PEO	Polyethylene Oxide

OER	Oxygen Evolution Reaction
HER	Hydrogen Evolution Reaction
NHE	Normal Hydrogen Electrode
LED	Light Emitting Diodes
DMF	N,N'-Dimethylfomamide
QD	Quantum Dot
PES	Photoelectron Spectroscopy
KPFM	Kelvin Probe Force Microscopy
AFM	Atomic Force Microscopy
EBIC	Electron Beam Induced Current
CBD	Chemical Bath Deposition
SILAR	Successive Ionic Layer Adsorption and Reaction
CV	Crystal Violet
RhB	Rhodamine B
UPS	Ultra Violet Photoelectron Spectroscopy

Chapter 1 Introduction

1.1 Overview to Titanium Dioxide (TiO$_2$)

Titanium dioxide, one of the top 20 inorganic chemicals of industrial importance, was discovered in 1821 [1] and its commercial manufacture began by 1916; resulting in a tremendous increase of research into TiO$_2$ [2-4].

Wide bandgap (3.0-3.2 eV) titanium dioxide is a semiconductor, which has different applications owing to its earth abundance, low cost, solution processability, ease of surface functionalization and excellent photoconversion features in the ultraviolet (UV) spectral region. TiO$_2$ has three crystalline phases named anatase, rutile, and brookite. Anatase and rutile are the common and commercially used phases. Each phase demonstrates unique physical properties such as bandgap [5-8] and unique chemical properties resulting in different applications. Both anatase and rutile phase have tetragonal crystal structure while brookite has an orthorhombic unit cell.

In all three phases of TiO$_2$; six oxygen atoms surround one Ti atom sitting at the center (TiO$_6$), which forms an octahedral shape. The only difference among these three phases is the way in which the octahedra are packed and the average distance between titanium atoms and oxygen atoms. In brookite phase, the octahedron shares the edges and/or apex with neighboring ones, whereas in rutile and anatase the apex and edges are shared respectively. This distance is respectively greater for the anatase phase compared to rutile [9]. This results in less thermodynamic stability for anatase and brookite compared to

rutile in bulk form unless the grain sizes are smaller than 14 nm in diameter for nanoparticles which leads to anatase to be the most stable one. Figure 1.1 shows the geometric structures for all three phases.
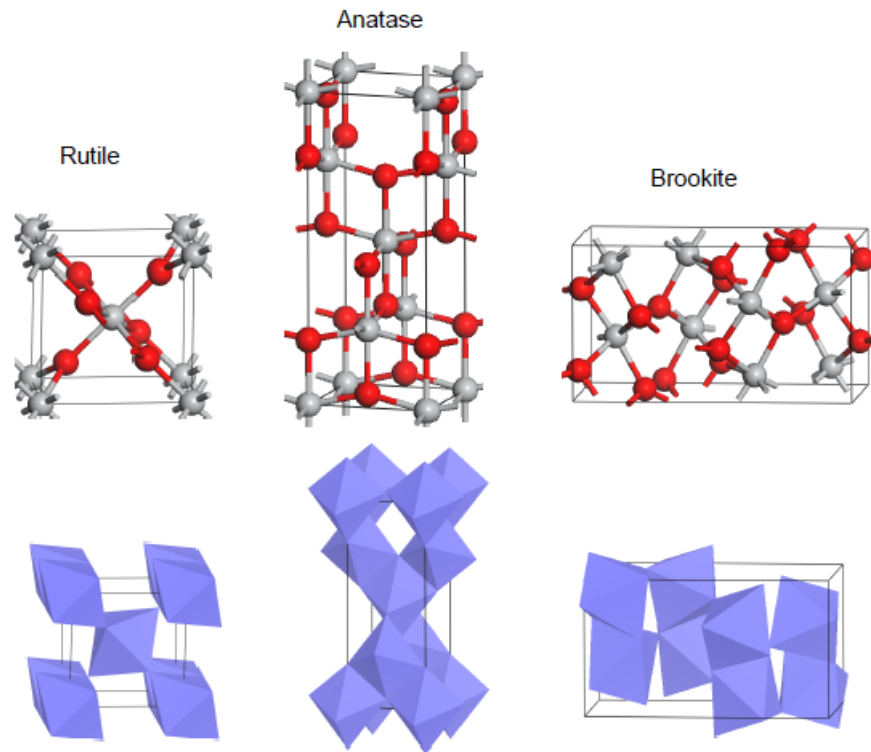
Figure 1. 1 Unit cells of TiO_2: Anatase, rutile and brookite, the upper part is the atomic structure (grey and reds represent the Ti and oxygen atoms respectively), the lower part represents the packing of the octahedral. [10]

Synthesizing TiO_2 by hydrolysis of inorganic or metal-organic titanium compounds results in mainly anatase and rutile phases whereas brookite is generally a by-product presented together with anatase and rutile [11]. It is difficult to get the pure anatase phase and usually a mixture of anatase, rutile and amorphous phases are observed in most of the synthesis protocols. For example, Degussa P25 which is one of the most used titania

products consists of approximately 80% anatase and 20% rutile. Anatase phase TiO_2 has an indirect bandgap of around 3.2 eV [5, 7], whereas rutile phase shows both direct and indirect bandgap of 3.06 eV and 3.10 eV respectively [6]. Anatase and rutile phases are being used for photocatalytic applications [12] and gas sensing [13] owing to their metastable phase and stable phases respectively. For brookite, there is no commercial interest found yet except in dye-sensitized solar cells [14].

TiO_2 is a suitable material for optical applications due to its properties including transmittance in the visible region and having high refractive index. The electrical conductivity of TiO_2 is dependent on the oxygen partial pressure and porosity, which makes it a good candidate for many applications such as gas sensing and photocatalysis [13, 15-17]. Nontoxicity, stability over a wide pH range under irradiation conditions [18], and chemical inertness are some distinct features, which makes it the most extensively used photocatalytic material.

TiO_2 has high wettability owing to photoinduced superhydrophobicity by trapping the holes in its surface [19]. Artificial heart valve and dental implants are some other examples of recent medical application for titania [20, 21]. A great number of TiO_2 applications are based on its nanostructured forms owing to their high surface area. Fig 1.2 shows various applications of TiO_2 in different fields.
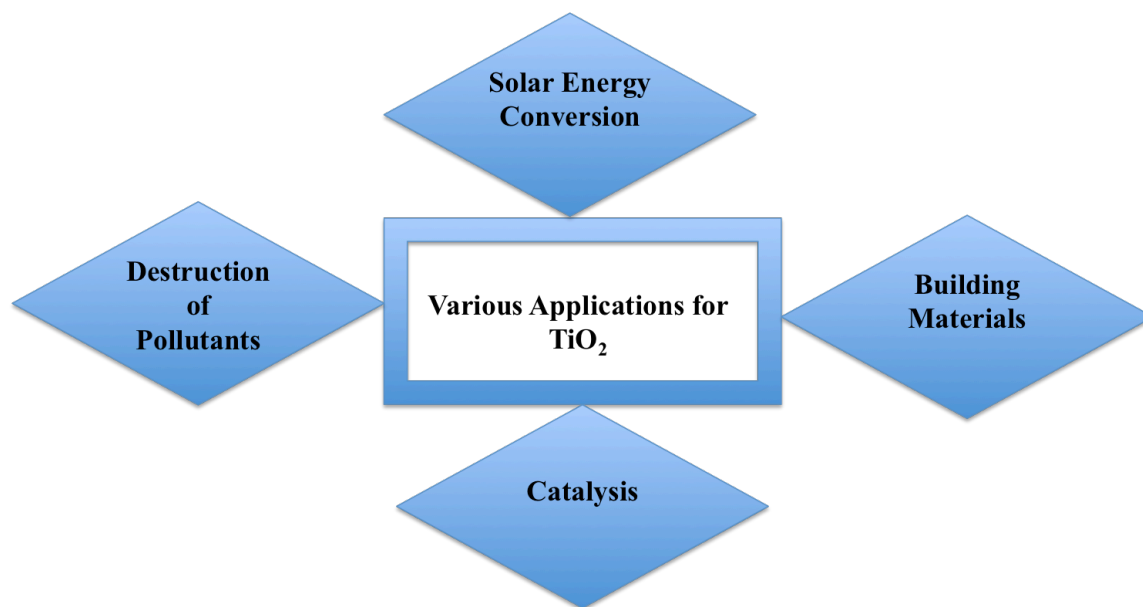
Figure 1. 2 Different applications of TiO$_2$.

TiO$_2$ has numerous applications based on its morphology, crystal structure, crystal size, surface area and porosity. It can be architectured into various morphologies such as thin film, powder, nanoparticles [22], nanorods [23], nanowires [24], nanotubes [25] and nanoribbons [26, 27] and single crystals etc. with high surface area and remarkably tuned pore structures.

A variety of organic and inorganic semiconductors perform photoinduced electron transfer to the conduction band of TiO$_2$ which forms the basis for the use of TiO$_2$ in excitonic and perovskite solar cells, sensitized photoanodes and heterojunction photocatalysts [28]. Chemical vapor deposition (CVD) [29], spray pyrolysis [30], thermal oxidation of titanium [31], physical vapor deposition (PVD) [12, 32], ion beam sputtering [33], electron beam vacuum deposition [34] and sol-gel process [35] are examples of different methods used to prepare TiO$_2$ films.

1.1.1 Phase Transformation

The phase structure of TiO_2 and their transformation among different phases could be affected by the synthesis conditions. Temperature, particle size, dopants, impurities, pressure and hydrothermal conditions are some of the factors that influence the transformation among different phases. Annealing the amorphous TiO_2 up to 400 °C turns the structure into anatase while annealing at elevated temperatures (600-1100 °C) promotes formation of rutile phase [36, 37]. Further, anatase phase gets transformed into rutile phase at temperatures of 700-800 °C [38], and annealing increases the particle size for both anatase and rutile. Brookite can transform directly into rutile [39] or can transform first into anatase and then rutile [40].

Additives are the other factor, playing a role in phase transformation by forming oxygen deficiencies or lattice defects of Ti in the crystal structure [41]. Different metal ions result in different transition temperatures. Some additives such as sulphate ions, silica and alumina stabilize the anatase phase [42-44], and others such as chloride ions further speed up the phase transformation of anatase to rutile under hydrothermal conditions [45, 46]. It is confirmed that the metastability of the anatase phase as a function of pressure is size dependent, leading structures with small particles to be conserved under high pressure conditions [47].

1.1.2 Nanomaterials

As the significant dimension of matter shrinks to the micro- and nanoscale, coulombic, Van der Waals and capillary forces become stronger relative to magnetism, gravity and

torque due to scaling laws. Furthermore, quantum confinement effects became increasingly important by decreasing the system size. Consequently, the structural, mechanical, electrical, optical and chemical properties of materials change when reducing the feature size to the nanometer range. The dramatic increase in the surface-to-volume ratio accompanying size reduction to the nanoscale results in surface- and interface phenomena becoming progressively more important than bulk phenomena. For TiO_2 particles about or less than 1 nm in size, charge carriers act as particles in a box. The mentioned effect which is quantum mechanical confinement leads to an increase in the bandgap [48]. By changing the structure and size, the optical and electronic properties of TiO_2 nanostructures can be manipulated. The nanostructures include rods, wires, tubes and fibers. Porous structures including micropores (< 2 nm), mesopores (2 –50 nm), and macropores (> 50 nm) are being used in catalytic applications. TiO_2 has the potential of being used in both micro- and nano- scale applications. It is also low cost, stable under illumination and deployable in environment friendly applications, which brings TiO_2 into attention [2, 49, 50].

1.2 TiO_2 Synthesis and Growth

Various synthesis protocols of TiO_2 such as solution based and gas phase-based methods have been described in the literature, which lead to different crystallinity and morphology of TiO_2. Solvothermal, electrochemical, and sol-gel processes are some examples for solution-based methods while chemical vapor deposition (CVD), physical vapor deposition (PVD) and spray pyrolysis are classified as gas phase methods. The synthesis

method can be adopted depending on the material properties, equipment conditions and desired properties for the material. Furthermore, one can change the properties to be suitable for different applications by adding various metals into TiO_2 and varying different factors such as the volume and diameter of the nanostructure. Below are some of the most commonly used techniques to synthesize TiO_2.

1.2.1 Chemical Vapor Deposition (CVD)

CVD is a technology whereby a solid material is coated on the heated substrate material. In CVD the material is deposited from the vapor phase due to a chemical reaction, and the resultant material could be in the form of powder, single crystal or thin film [51].

Substrate temperature and material, reaction gas, composition, gas pressure are some parameters, which could lead to a change in the physical and chemical properties of the grown material. Uniformly coated film with low porosity on any kind of substrate is one of the advantages of CVD.

Different types of CVD processes are available such as plasma-enhanced chemical vapor deposition, photochemical vapor deposition, metal-organic chemical vapor deposition, low-pressure chemical vapor deposition, chemical vapor infiltration, chemical beam epitaxy, plasma-assisted chemical vapor deposition, laser chemical vapor deposition, atmospheric pressure chemical vapor deposition and metal-organic chemical vapor deposition etc.

1.2.2 Physical Vapor Deposition (PVD)

Physical vapor deposition method is a family of processes including vacuum evaporation, sputtering and ion plating, which is used to coat thin films on different substrates such as glass, metal and plastics. In a PVD process, the material inside the vacuum chamber is changed into the vapor phase and then thickens on a substrate. The coated material in a PVD process could be a metal, ceramic, alloy or any other inorganic compound. Each process in CVD method has some advantages and disadvantages. Sputtering leads to obtain coatings with better adhesion and slow deposition rate. Although vacuum evaporation is cost-effective and simple, the coating adhesion is not comparable with other PVD methods. The best adhesion and coverage with more deposition rate than sputtering are some important points to be considered for ion plating. Even though PVD is more complex compared to CVD, purer and smoother TiO_2 films with higher conductivity and crystallinity are some advantages of PVD [19].

1.2.3 Sol-Gel Method

Sol-gel processing is a well-established approach to synthesize metal oxides and categorized into aqueous and non-aqueous methods depending on the nature of the employed solvent. The process includes, the hydrolysis and polycondensation reactions of a molecular precursor in a liquid and a final step of drying. Different steps for metal oxide formation include fast hydrolysis of the metal precursor to yield the metal hydroxide solution proceeding by instant condensation leading to form the three-dimensional gel. In the final step, the gel will be converted to xerogel or aerogel

depending on the applied drying mode. The method has better control over the complete reaction as well as the textural and surface characteristic of the material. The enhancement of material properties and the formation of new materials could be mentioned as the significance of this method [52]. Different applications of the sol-gel method would be categorized as optical and photonic, thermal, mechanical, electronic, chemical, biochemical and biomedical functions.

1.2.4 Electrodeposition and Electrochemical Anodization Methods

Electrodeposition (ED) is the process of forming a film on the electrode by applying electricity as the external source. The process consists of a working electrode, a counter electrode and a reaction vessel for the two-electrode electrodeposition setup, where the applied current conducts the reaction through the chemical and forms the film. The reference electrode is added to the setup mentioned above for the three-electrode setup, which is responsible for controlling the absolute potential of the working electrode. For the three-electrode setup, the substance is deposited by modifying the applied current through the potential scan.

Electrochemical anodization is the most common electrochemical method of forming an oxide layer on the substrate. The setup is like the two-electrode setup ED, where the material deposits on anode reverse to ED and that is why it is named as anodization.

 The mentioned methods are reliable, simple, cost-effective, and highly controllable using parameters such as pH, bath temperature, deposition time, deposition potential and electrolyte concentration.

1.2.5 Hydrothermal Method

The hydrothermal or solvothermal method is being used to synthesize or fabricate a nanomaterial with different morphologies. The common explanation expresses any heterogeneous chemical reaction in the presence of aqueous or nonaqueous solvent, with all the reactants being located inside an autoclave. The pressure and temperature of the reaction in the closed system should be kept above room temperature and 1 atm respectively. The method is named solvothermal or hydrothermal based on the reaction medium. If the medium is water the method is hydrothermal, else it is being named as solvothermal [53].

The method has some disadvantages such as the usage of an expensive autoclave. Strong controllability in composition and the material quality on a large area, are some advantages to be mentioned.

1.2.6 Successive Ionic Layer Adsorption and Reaction (SILAR) Method

Successive ionic layer adsorption and reaction (SILAR) method is a facile fabrication process with different advantages in comparison to the other thin film fabrication methods [54, 55], including obtaining uniforms films, independent of the substrate material, great control over the deposition rate and film thickness, being non-vacuum, cost-effective and low temperature. It happens by the metathesis reaction occurring between adsorbed cations and anions, which results in thin film formation of the desired material. The basic idea behind the SILAR method is adsorption, which is collecting the material on the surface of the other material, which happens by contacting two materials

of different phase. Rinsing is the other important step, by which the excess species, unreacted species and byproducts would wash away from the surface. The SILAR method will be explained in detail in chapter 4.

1.3 Thesis Scope

Each chapter in this thesis, which is based on the different classification of TiO_2 nanostructure and their applications, has its own introduction and list of references.

Chapter 2 reviews background information, experimental methods, surface modifications, characterizations and hydrophobicity tests for the TiO_2 nanotube arrays/TiO_2 nanowire arrays (TNTAs/TNWAs) hierarchical structure on Ti foil.

In chapter 3 the new solid-state method for TiO_2 nanotube preparation as well as its characterization and applications are presented. Chapter 4 includes the SILAR method for the fabrication of lead sulfide (PbS) quantum dot on TiO_2 nanotubes/nanowires and their application in dye degradation.

Finally, in chapter 5, remarks of previous chapters, along with the recommendations for further work will be given.

Chapter 2 TiO$_2$ Nanotube-Seeded TiO$_2$ Nanowires: Hierarchical Structures for Stable Wetting and Antifouling Studies

In Chapter 2, background information, experimental methods and characterizations for the TiO$_2$ nanotube arrays/TiO$_2$ nanowire arrays (TNTAs/TNWAs) hierarchical structure on Ti foil, together with surface modifications to adjust the wetting properties of material and superhydrophobic applications are presented.

2.1 Introduction

As mentioned earlier in the previous chapter, numerous methods are used to grow TiO$_2$ films such as physical vapor deposition [1], thermal oxidation [1], sol-gel method [2, 3], electrochemical anodization, [4] and hydrothermal method [5]. Among the mentioned methods, electrochemical anodization and hydrothermal methods are the most appealing approaches due to their low cost, ease of fabrication, and control over nanostructure morphology of TiO$_2$.

TiO$_2$ nanotubes grown by the electrochemical anodization method can be formed on the surface of sputtered Ti [4], evaporated Ti [6] and Ti foil [7]. Hydrothermally grown TiO$_2$ nanowires can also grow on different substrates such as glass or FTO [8]. Both TNTAs and TNWAs with nanostructured morphologies can be used for super anti-wetting

applications due to their superhydrophobic surfaces.

Superhydrophobic surfaces with low water adhesive forces, high roughness, and high contact angle are best for self-cleaning and anti-icing applications [9, 10]. Wetting behavior, which is an important characteristic of a solid surface, greatly depends on the surface roughness and composition. The most typical test for measuring these adhesive forces, roughness, and composition is a contact angle (CA) measurement. Surfaces with contact angle less than/ larger than 90° are called hydrophilic/ hydrophobic; whereas those with a contact angle less than 10°/ larger than 150° are named superhydrophilic and superhydrophobic, respectively [11]. There has been vast research on superhydrophobic and superhydrophilic surfaces and their applications such as waterproofing [12], self-cleaning [13] anti-corrosion [14] and antifrosting [15]. Highly rough superhydrophobic surfaces owe their self-cleaning mechanism, which is called the Lotus-Effect, to their anti-adhesive and water-repellent characteristics. This effect can be used for different surfaces on consumer products like cars, windows, and clothes. Contact angle measurements of a surface depend on different factors such as morphology and chemical composition of the surface [16, 17]. Even though the nanostructures of both nanotubes and nanowires have rough surfaces, the nature of TiO_2 is hydrophilic [18]. The best way to alter the surface to attain hydrophobic behavior is to functionalize the nanostructures with various organic molecules using self-assembled monolayer (SAM) formation methods [19-22]. Commonly, SAMs have polar head groups which get interact with -OH groups on the surface of TiO_2, and tails composed of a long carbon chain, with or without substituted hydrogen atoms with fluorine atoms.

There are numerous studies, which coat another nanostructured material on top of the

13

other to obtain a rougher structure and make the surface more hydrophobic. Chu *et al* [23] studied the wetting behavior of porous titania micro-holes/ZnO nanorods and they showed that the presence of ZnO nanorods increases the surface roughness and improve the surface hydrophobicity. Later Ottoneet *et al.* [7] prepared hierarchical nanostructures of TNTAs/ZnO (nanoparticles, nanowires) and got a water contact angle of 130° for TNTAs/ ZnO nanowires, where the TNTAs and ZnO nanowires have 24° and 92° water contact angle, respectively.

To the best of our knowledge, there is no study on hierarchical TiO_2 nanowires decorated on TiO_2 nanotubes surface in literature, which studies the wetting behavior of the unique surface. Lv *et al*. [24] prepared TNWAs/TNTAs where the TNWAs were treated by wet-chemical reaction (WCR) method with an alkaline solution. They showed that this structure utilizes the light very efficiently and enhances the photoelectrochemical (PEC) performance.

Herein, we fabricated the hierarchical structures of TNWAs/TNTAs, where the TNWAs are grown hydrothermally and subsequently functionalized with octadecylphosphonic acid (ODPA) SAMs.

2.1.1 Introduction to Superhydrophobic Surfaces

The physical phenomenon of the Lotus effect, which is used by Professor Wilhelm Barthlott from the University of Bonn for the aim of technical applications, [1] got scientist's diligence even after hundreds of years. This effect signifies two unique properties of self-cleaning and hydrophobicity. Here, the self-cleaning effect means rolling off the surface dirt particles by water droplet by small tilting angles (<10˚),

whereas it would not happen for the common surface. This hydrophobicity relates to the roughness of the surface, which could be applied to manufacture surfaces on consumer products such as cars, windows, and clothes. Lotus leaves have rough surfaces due to their fine surface structure coated with hydrophobic wax crystals with diameters of several nanometers. The surfaces with nanoscale roughness are more likely hydrophobic than smooth surfaces. This could be due to the reduced contact area among solid and water droplet. The diagram in Fig. 2.1 shows the relationship between surface roughness and self-cleaning, with rough surfaces the polluting particles adhere to the water droplets and remove them from the surface by rolling the water droplet off the surface. For smooth surfaces, the water moves over the surface but does not remove the polluting particles.
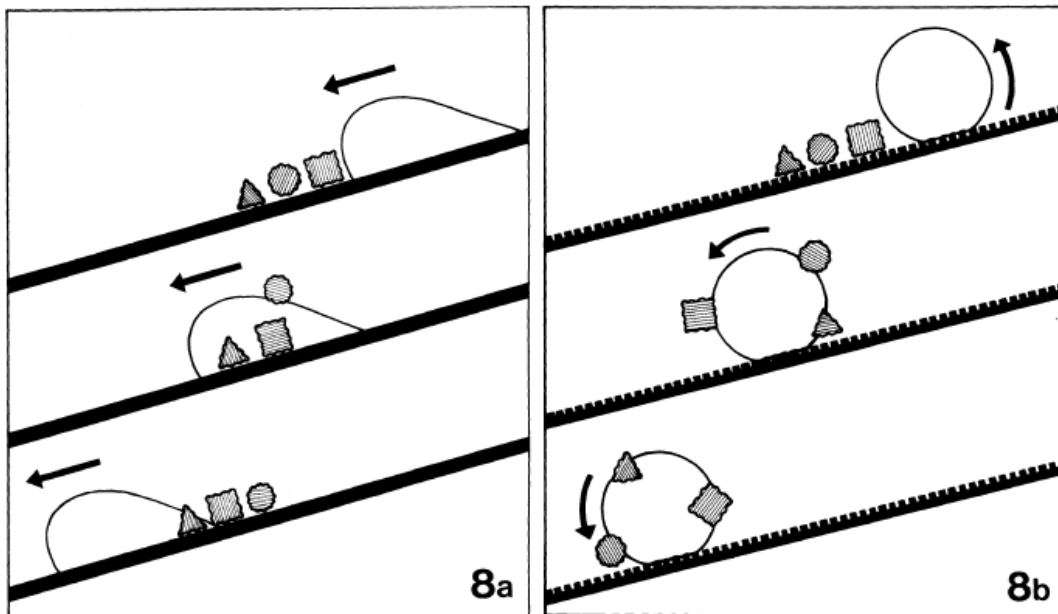
Figure 2. 1 Connection between roughness of surface and self-cleaning. Reprinted with permission from ref. [25] Elsevier 2013.

There are plenty of plants and animals such as spider's leg, butterfly wings and cicada's wings [2], which repel water due to their hydrophobic surface components. All these imply that micro and nanoscale hierarchical structures with low surface energy lead to superhydrophobic and self-cleaning surfaces [3].

2.1.2 Introduction to Contact Angle

One important characteristic of solid material is surface wettability, which is the balance between cohesive and adhesive forces [2, 3]. This can be measured by the angle of the liquid/vapor interface with the solid named by "contact angle". The line at which the interface contacts the solid material is defined as the three-phase contact line. In order to drive the contact angle thermodynamically using Fig. 2.2, one should minimize the free energy. All three interfaces of liquid-vapor, solid-liquid, and solid-vapor with interfacial free energies of γ_{LV}, γ_{SL} and γ_{SV} respectively and their areas are responsible for the change in free energy of the overall system. This can be shown as
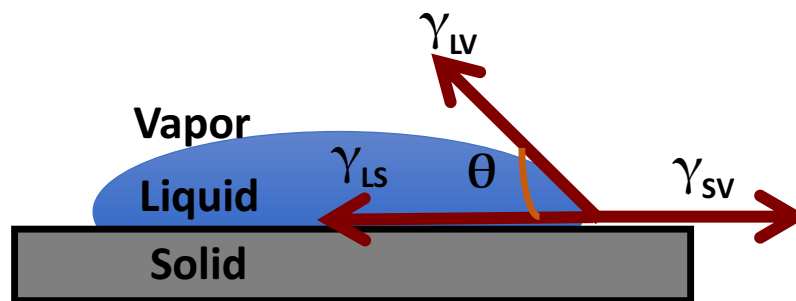
Figure 2. 2 Contact angle for a liquid droplet on a solid surface.

$$G = (\gamma_{LS} - \gamma_{SV})dx + \gamma_{LV}\cos(\theta)\,dx \tag{1}$$

At equilibrium condition dG is zero which leads to the equation:

$$\gamma_{LV}\cos(\theta) = \gamma_{SV} - \gamma_{SL} \tag{2}$$

The equation above is named Young equation [16]. Contact angle, which is the magnitude of θ, is defined in terms of the interaction terms in the equation as follow.

$$\cos(\theta) = \frac{\gamma_{SV} - \gamma_{SL}}{\gamma_{LV}} \tag{3}$$

If the θ is smaller than 90°, the surface is determined as wetting and the free energy for the solid-liquid system is smaller than the free energy for the solid-vapor system. By maximizing the solid area covered with liquid the overall free energy of the system will be lowered and the system will get closer to equilibrium. If the θ satisfies the condition $90 < \theta \leq 180$, the system is called non-wetting and in order to minimize the overall energy of the system, the liquid is pushed back from the system. In the case the liquid is water, the surfaces are called hydrophilic and hydrophobic for wetting and non-wetting cases. It should also be mentioned classification, also have ratios inside, for instance, the system with contact angle of 50° is more hydrophilic compared to one with contact angle of 70°, even though both are classified as hydrophilic.

2.1.2.1 Wenzel and Cassie-Baxter Wetting

The total area of the solid material has a direct relation with the surface roughness. The maximum surface area increases the interfacial free energy and causes a change in

contact angle. Figure 2.3 shows the Young's, Wenzel and Cassie–Baxter models, which are employed to define and explain the homogeneous and heterogeneous wetting regimes [26].

The following equation represents the Wenzel model, which estimates the effect of surface roughness on wettability [16]:

$$\cos \theta^* = r \cos \theta_Y \tag{4}$$

Where θ^* is the expected angle for rough surfaces that correlate with the stable equilibrium state, θ_Y is the local angle for the comparable smooth surface. r is the rugosity factor and is shown below.
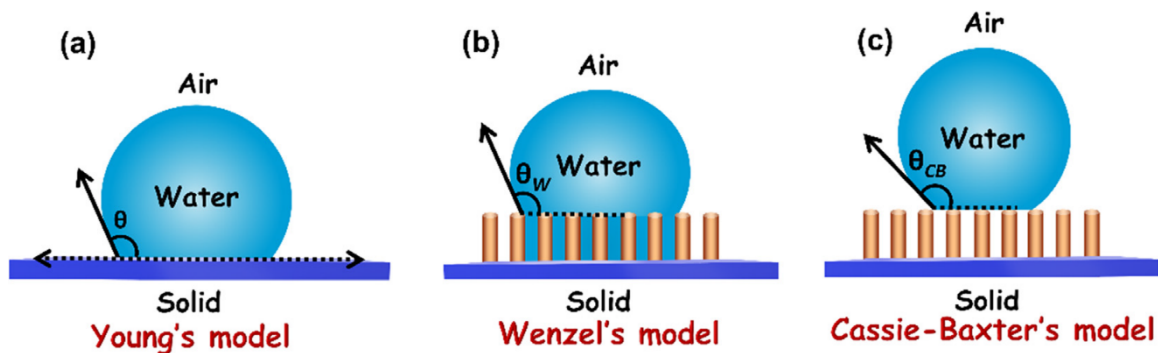
Figure 2. 3 Young's (a) Wenzel (b) and Cassie-Baxter (c) illustrations. Reprinted with permission from ref. [27] Elsevier 2019.

$$r = \frac{A_{true}}{A_0} \tag{5}$$

Where, A_{true} is the actual surface area for rough material and A_0 denotes the apparent surface area. If the roughness ratio is larger than 1, the hydrophilic and hydrophobic surfaces will be more hydrophilic and hydrophobic respectively.

It worth to be mentioned that in equation 5, if the value for the right side is greater than +1 then the system is fully wetting and if it is less than -1 is the non-wetting system. If the roughness or hydrophobicity of the surface increases, then the air would be placed between the solid material surface and water and the probability that the water could meet the solid surface and wet it decreases. This case is specified by Cassie model, which is represented by the equation below:

$$\cos\theta^* = f(\cos\theta_Y + 1) - 1 \qquad (6)$$

Where, f is the portion of the solid material surface, which is wetted with the liquid on top. f has a reverse effect on the θ^* and decreasing the f cause the increase of θ^* leading in obtaining superhydrophobic surface. As the example for the model is Lotus effect, which the water spreads onto the nanostructured surface in a way that air but not water is trapped among the holes with nanosize [28]. Even though the surface, which water contacts is not hydrophobic, the whole surface behave as superhydrophobic due to the high contact angle of 180º among the traps air and hole of the surface [29].

Tsujii's group studied Wenzel and Cassie states by investigating the contact angle for a rough surface θ_f and on a flat surface θ_Y [30]. They applied different liquids on the solid surface causing a change on θ. Figure 2.4 shows the plot for $\cos\theta_f$ as a function of $\cos\theta$

to present the surface roughness impact. The curve complies the Cassie Baxter and

Wenzel states, the intersection at the critical angle of θ_c [31, 32] as:

$$\cos\theta_c = \frac{f-1}{r-f} \tag{7}$$

Wenzel and Cassie Baxter are more thermodynamically preferable states for $\theta_Y < \theta_c$ and

$\theta_Y > \theta_c$ respectively.
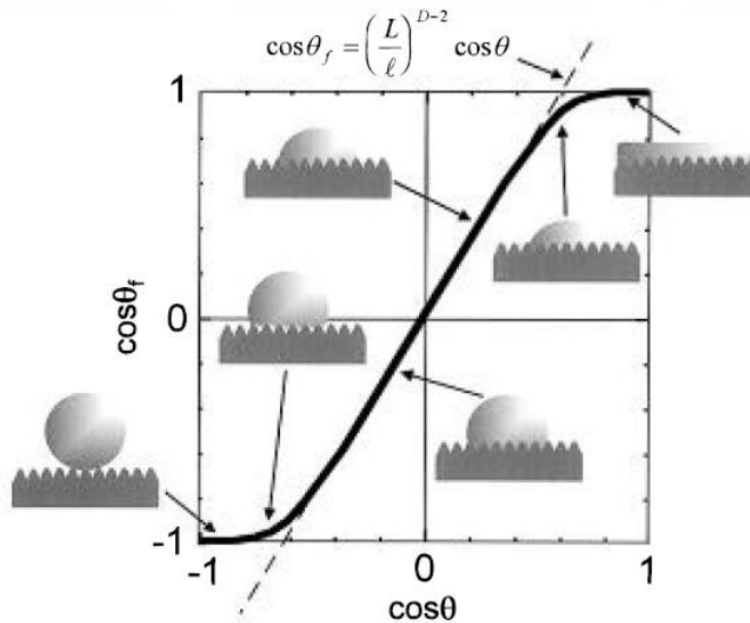
Figure 2. 4 $\cos\theta_f$ as a function of the $\cos\theta$: Considered contact angle on the textured surface, as a function of Young contact angle. Reprinted with permission from ref. [33] Annual Reviews 2008.

2.1.2.2   Contact Angle Hysteresis

Different factor such as change in interfacial energy, roughness and heterogeneity of the

surface affect the contact angle Hysteresis, which is mentioned as below.

Contact Angle Hysteresis=$\theta_A - \theta_R$ (8)

Where θ_A, advancing contact angle and θ_R, receding contact angle, are the angle which the solid makes with the interface and the angle which is relative to the solid on the point of liquid receding.

For structurally or chemically heterogeneous surfaces, the contact line would change depending on whether the contact line is advancing or receding. One other important factor affecting the contact angle hysteresis is molecule adsorption or desorption at the time liquid and solid contact. This cause a change in interfacial energy and getting different θ_A and θ_R [34, 35]. Also, it is worthy to mention that Young's equation is applicable on a specified part of the surface but not for the surface average and it gets more importance when the surface is rough. This is the point the contact angle hysteresis gets more importance.

2.1.3 Introduction to Fabrication of Superhydrophobic TiO₂ Surfaces

In this thesis; TiO₂ nanostructures were fabricated *via* electrochemical anodization and hydrothermal methods. So, these two methods and their mechanisms will be explained in detail here.

2.1.3.1 Electrochemically Anodized Titanium Dioxide Nanotube Arrays (TNTAs)

There are a variety of methods to synthesize TNTAs such as sol-gel, atomic layer deposition (ALD), use of nanoporous alumina templates, hydrothermal and electrochemical anodization methods. All the mentioned methods have some benefits and drawbacks. As an example; using nanoporous alumina templates propose limitations such as not reaching small sized and smooth nanotubes even though the dimension of nanostructure could be controlled [36], whereas the hydrothermal synthesis leads to very small diameter but not ordered nanotubes [37]. Electrochemical anodization has control on both morphology and dimension of nanotubes. The composition, concentration, and viscosity of electrolyte, anodization time/potential and simple set up are key factors leading this method to be widely used for industrial applications. The TiO_2 nanotubes fabricated by anodizing the Ti are studied in detail in the literature [37-39]. The as-fabricated self-organized TiO_2 nanotubes are a perfect choice for Cassie-Baxter state of the superhydrophobic surface due to their "honeycomb" like structure. The as-prepared amorphous TNTAs could be altered to whether anatase or rutile phase based on the annealing temperature being applied to them. In electrochemistry, the electrochemical anodization process includes the dissolution of anode metal and formation of an oxide layer. Figure 2.5 represents the four present processes which are active and compete in electrochemical anodization of TNTAs: field assisted oxidation, field assisted migration, field assisted dissolution, and chemical dissolution.
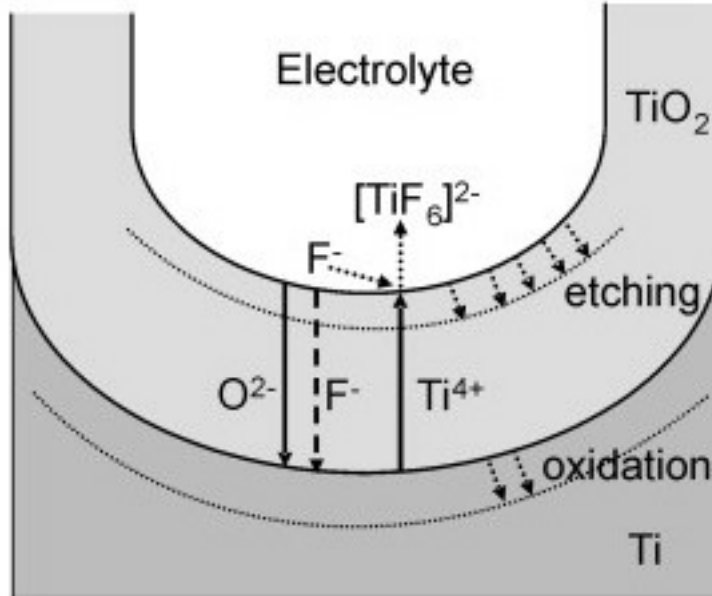
Figure 2. 5 Represents the anodic TNTAs growth in presence of fluorides. Reprinted with permission from ref. [41] Elsevier 2007.

Water is responsible for supplying both O^{2-} and OH^- ions which react with released Ti^{+4} from anode. These reactions provide the anhydrous and hydrated oxides as below:

$$Ti^{+4} + 2O^{-2} \rightarrow TiO_2 \tag{9}$$

$$Ti^{+4} + 4OH^- \rightarrow Ti(OH)_4 \tag{10}$$

During the electrochemical anodization process, $TiO_2.xH_2O$ complex is the introduced product as the gradient of hydration concentration across the film. The inner layer is anhydrous with TiO_2 and outer one is more hydrated due to the $Ti(OH)_4$ resulting from

the excess of hydroxyl ions [42, 43]. Later on the chemical dissolution step occurs which is the probable dissolution of Both TiO_2 and $Ti(OH)_4$ fluoride ions as:

$$TiO_2 + 6F^- + 4H^+ \rightarrow [TiF_6]^{2-} + 2H_2O \qquad (11)$$

$$Ti(OH)_4 + 6F^- \rightarrow [TiF_6]^{2-} + 2H_2O + 4OH^- \qquad (12)$$
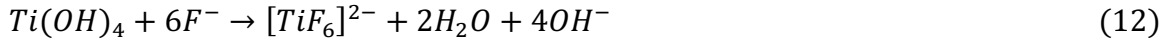
Following step is the field assisted etching process, which moderates the present bond of Ti-O using the applied electric field. This is the beginning of pore creation at the oxide/electrolyte interface [44]. There will be an oxide flow to the cell boundaries, which leads to obtaining a fluoride-rich layer ending in pore to tube alteration. The fluoride and Ti^{+4} ions flow towards the anodic metal and electrolyte respectively due to the applied potential, which forms fluoro-complexes. $[TiF_6]^{2-}$ is the steadiest in the electrolyte.

Figure 2.6 shows the current density (j) plot versus time (t), three steps of TiO_2 nanotube growth, representing the change in anodization current variation with time. Firstly, anodization current undergoes an abrupt decrease. This is due to the introduced diffusion limit on O^{2-} and OH^- ions by the present barrier layer.

Later on, in the second stage, the current density experiences a raise due to the field-assisted and chemical dissolution of the barrier layer. In this step the oxide layer would be porous due to the migration of Ti^{+4} to the electrolyte and reacting with the F^-, leading in formation of soluble $[TiF_6]^2$. In third stage, the F^-ions diffuse more through the oxide layer, promoting the etching process due to the present electric field, leading the tube formation. This step starts with an increase in current density because of tube

formation and gets steady, or drops slowly in another word, once the competition between the oxide layer formation and dissolution gets stable.
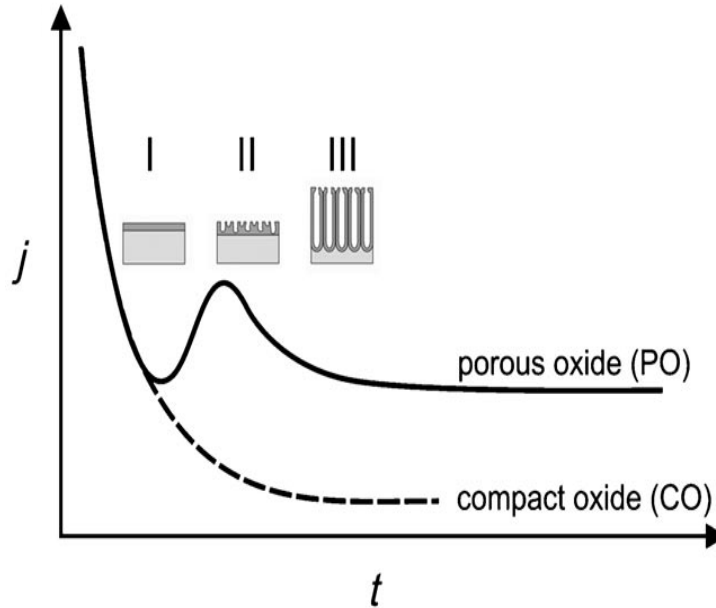
Figure 2. 6 Typical current vs time plot for three stages of electrochemical anodization process. Reprinted with permission from ref. [40] John Wiley and Sons 2011.

2.1.3.2 Hydrothermal Growth of Titanium Dioxide Nanowire Arrays (TNWAs)

Byrappa and Yoshimura were the first ones who used this method for nanomaterial synthesis on 21st century [45]. Later, different groups worked on obtaining TiO_2 nanowire arrays by hydrothermal method on different substrates [46-51]. Pressure is one of the key factors in the hydrothermal process; one can apply different pressures to get various nanostructures for different application. It has the control over the size of nanostructure; higher-pressure results in larger crystal sizes. This could be explained by the major role

of nucleation and crystal growth on the crystal size [52]. Pressure could enhance the solubility, which has a key role in hydrothermal growth [53]. Other additives are also essentially present during the hydrothermal process and have the great impact on parameters like solubility, crystal growth, and oxidation-reduction properties. The additives include capping agents, surfactants or bio-molecules and have control over growth orientation, which results in getting capping agents, surfactants or bio-molecules surfactants or bio-molecules like TNWAs [53].

2.1.3.3 Superhydrophobic Coating Based on Nanoparticles

In some processes, both hydrothermal and electrochemical anodization processes are not enough to obtain nanostructures with superhydrophobic surface, especially in industrial applications where a large surface area is required. Therefore, a coating technique is introduced to diversify the applications of TiO_2 superhydrophobic surfaces; since a coating is also considered a very practical approach for industrial applications due to its adaptability. A common method to obtain a coating is through spraying or brushing of a liquid. In order to obtain roughness and durability, the liquid is usually contained with a mixture of particles and polymers. For example, Steele et al. reported a coating based on ZnO nanoparticles and perfluoracrylic polymer [54]. When applied, the particle formed a self-arranged structure that is rough and has a micro-nano- hierarchy. After drying, the polymer acts as a glue to hold the rough structure and make the coating robust. As shown

in figure 2.7, the process allows the nanoparticles to act as a film-roughening agent, which results in a rough, low energy surface.
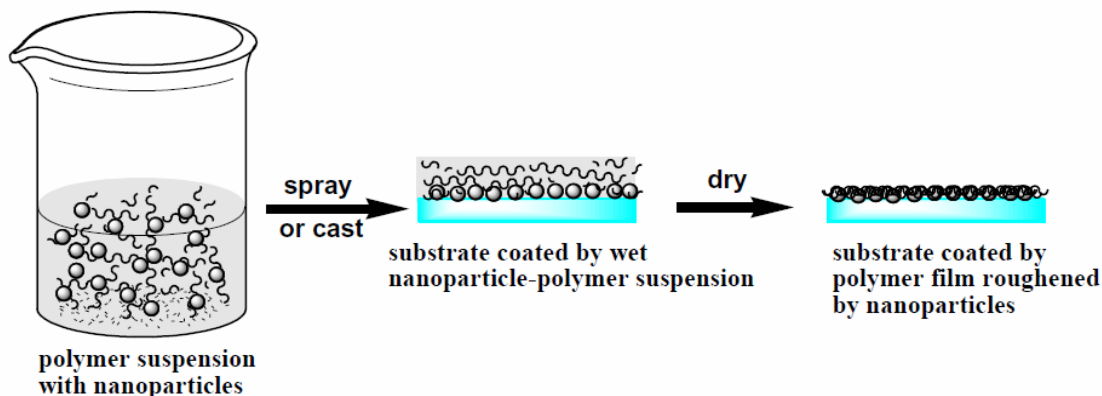
Figure 2. 7 The process of producing the nanoparticle-polymer blend based superhydrophobic coating. Reprinted with permission from ref. [54] American Chemical Society 2009.

2.1.4 Self-Assembled Monolayers (SAMs)

In order to change the surface energy of the material and obtain a Cassie-Baxter state; SAMs monolayer could be applied to the surface. SAMs could be any organic molecule or a single layer on surface of the material and the SAM growth process on the surface is named as functionalization. SAMs include long chains of functional groups such as phosphoric acid, carboxylic acid etc. at one or both ends. What distinguishes SAMs and Langmuir-Blodgett films is that the surfactants are physiosorbed to the surface as a Langmuir-Blodgett film but chemically bond to a surface when it is SAMs, which is also called, functionalized (Figure 2.8).
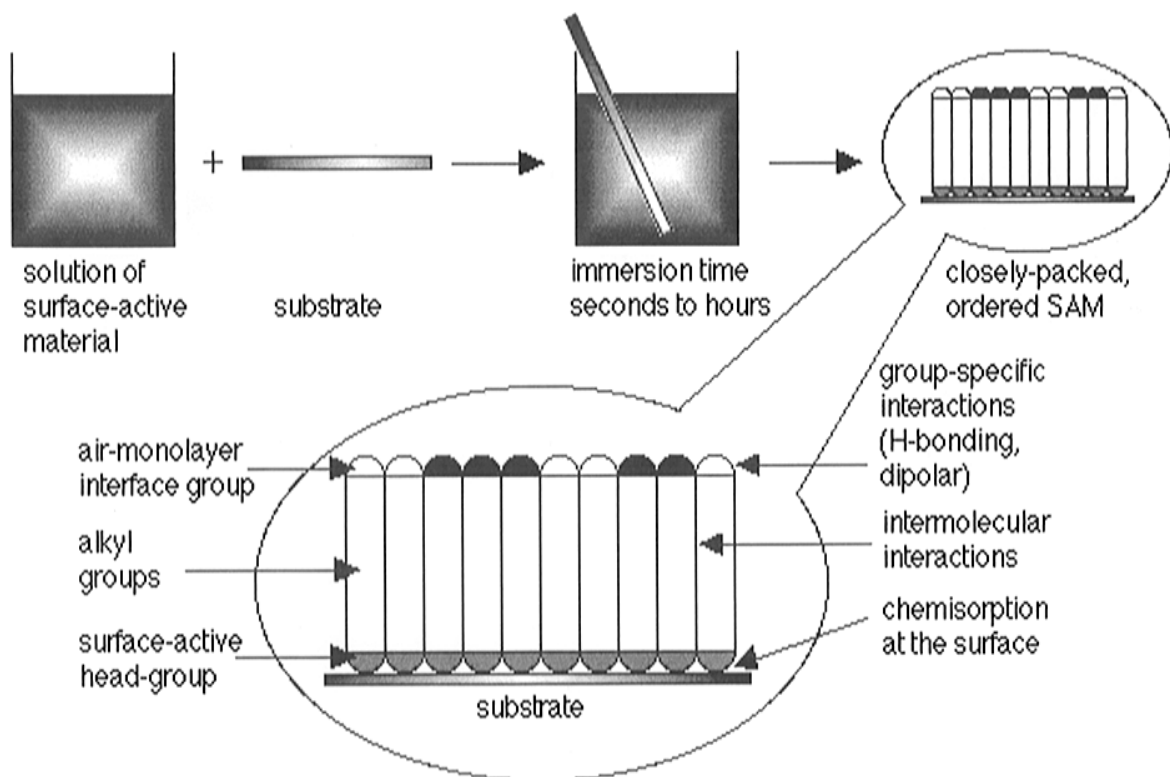
Figure 2. 8 Immersing method formed SAMs. SAMs will be formed on the surface due to spontaneous heat motion when immersed in a non-polar solution. Reprinted with permission from ref. [55]   American Chemical Society 1995.

2.2   Experimental Procedures

Titanium foil (thickness 1 mm, 99% purity,) was cut into 1 cm x 2.5 cm and 0.5 cm x 2.5 cm pieces to be used as anode and cathode respectively for electrochemical anodization growth of TNTAs. The electrodes were cleaned by ultrasonication in water, methanol and acetone for 10 minutes each. The anodization was performed at room temperature for 2 h in an electrolyte containing 0.3 wt. % NH_4F (99.5%, Sigma Aldrich) and 4 vol.% deionized (DI) water in ethylene glycol (98%, Sigma Aldrich). A constant DC voltage of 60 V was applied by a DC power supply (MPJA Inc.). The as-prepared TNTAs were

rinsed in methanol and dried with nitrogen and cleaned with RIE and O_2 plasma for 15 min. Finally, TNTAs was annealed for two hours at 450 ºC in a tube furnace to crystallize into the anatase phase. The prepared anatase phase TiO_2 nanotubes were decorated with hydrothermally grown rutile phase TiO_2 nanowires. Small diameter vertically oriented TNWAs were grown using a solution containing 9.5 mL of de-ionized (DI) water, 0.5 mL hydrochloric acid (HCL), and 0.025 mL titanium (IV) butoxide (Ti-Bu) (97%, Sigma Aldrich), all added to a Parr autoclave followed by heating at 150 ºC for 2 h. After cooling at room temperature samples were taken out, washed with DI water and dried under nitrogen blow. The afforded TiO_2 nanowires decorated TiO_2 nanotubes assemblies (TNWAs/TNTAs) were coated with ODPA (octadecylphosphonic acid, 97%, Sigma Aldrich) self-assemble monolayers (SAMs) by immersing overnight in methanolic solution of ODPA. Figure 2.9 demonstrates schematics diagram of various steps for the synthesis TNWAs/TNTAs nanostructures.
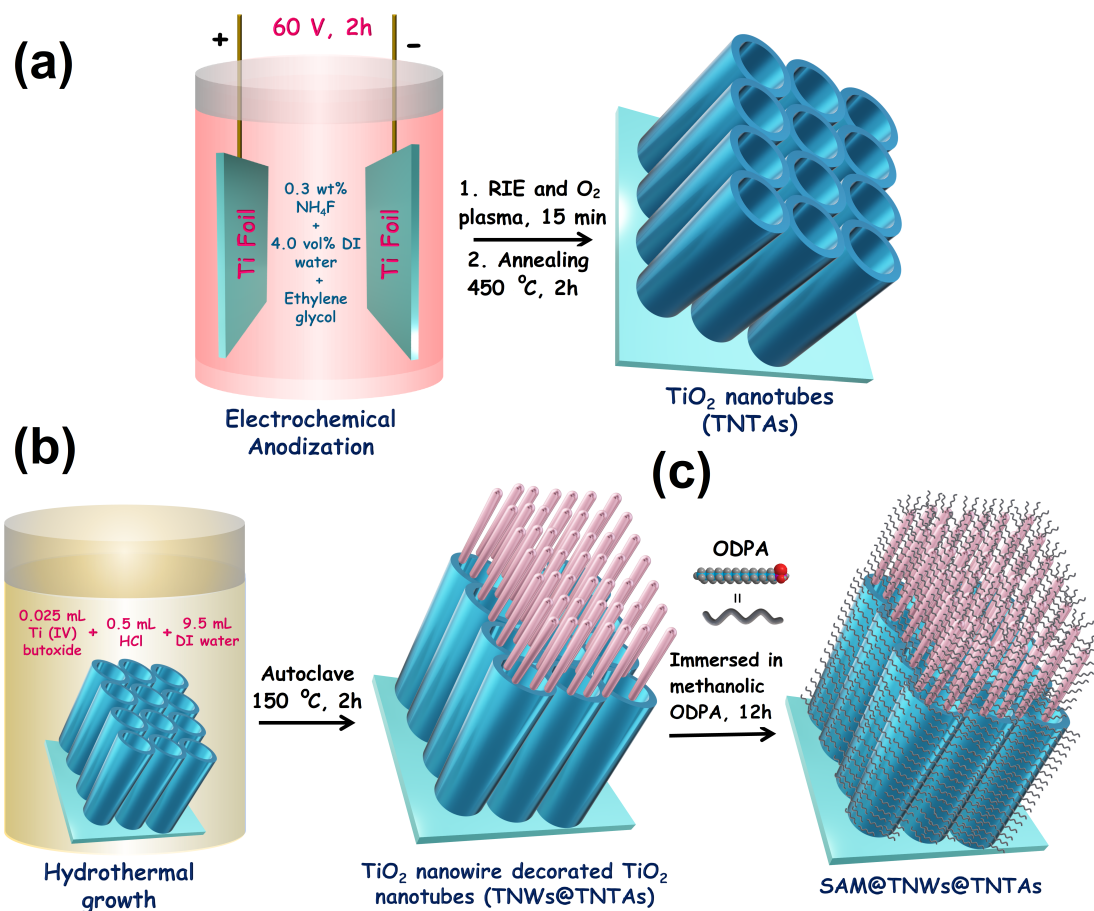
Figure 2. 9 (a) Synthetic scheme of TNTAs nanostructure on Ti foil via electrochemical anodization and (b) hydrothermal growth of TNWAs on TNTAs to form TNWAs/TNTAs assembly and (c) coating of ODPA.

2.3   Physio-Chemical Characterization

The morphological features of TNTAs, TNWAs/TNTAs materials were determined using field emission scanning electron microscope (FE-SEM), on a Zeiss Sigma FESEM equipped with GEMINI in lens detector, operating at an accelerating voltage of 5 keV. The phase structure and crystalline features of materials were executed with X-ray diffraction (XRD) recorded on Bruker D8 Discover instrument using Cu-Kα radiation (40

kV, λ = 0.15418 nm) equipped with a LynxEYE 1-dimensional detector. A scan size of 0.02° was used to measure spectra in the 2θ range of 20–70°. The optical absorption profile of materials in Ultraviolet-Visible (UV-Vis) region was measured by diffuse reflectance UV-Vis (DR UV-Vis) spectra recorded on a Perkin Elmer Lambda-1050 UV–Vis-NIR spectrophotometer equipped with an integrating sphere accessory. To confirm the successful functionalization of TNWAs/TNTAs surface with monolayer diffuse reflectance infrared fourier transform spectroscopy (DRIFTS) was performed on the samples using an iS5 FTIR spectrometer (Thermo Nicolet Nexus 670) equipped with a DRIFTS accessory.   The samples for DRIFTS was prepared by scratching-off materials from the Ti surface with the help of razor and mixing with spectroscopy grade KBr powder followed by pallet formation by the press.

The wetting behavior of the TNTAs/TNWAs samples was evaluated by optical contact angle measurements by the FTA-100 contact angle measurement system in ambient conditions. The image of the drop on the TNTAs/TNWAs/SAMs sample was acquired with the integrated camera. A DI-water drop with a volume of 0.35 μL was dispensed, and its profile was extracted by the software at the liquid-solid interface.

2.4   Results and Discussions

The top-view FE-SEM images of bare TiO_2 nanotubes show their open top end and easily accessible surface for potential TiO_2 nanowire's growth (Figure 2.10(a)). After hydrothermal growth of TNWAs on the surface of TNTAs, a preferred coverage of nanowires network was clearly visible (Figure 2.10(b), 2.10(c)). Figure 2.10(d), 2.10(e)

and 2.10(f) display cross-sectional and side view SEM images of TNWAs/TNTAs structure. It can be observed from Figure 2.10(d), 2.10(e) and 2.10(f) that approximately 100 nm long nanowires were grown primarily on the top of the approx. 12 μm long TNTAs, which was more accessible for the nanowire solution to penetrate.
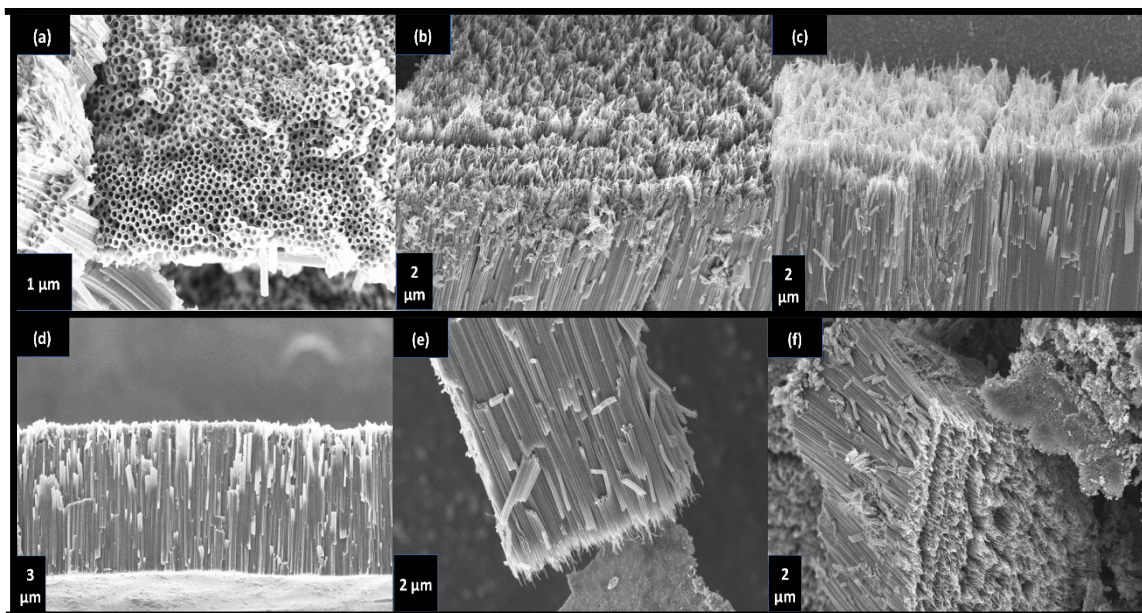
Figure 2. 10 (a) FESEM images of electrochemically anodized TNTAs displaying top view, (b-f) Top and cross-sectional view of hydrothermally grown TiO$_2$ nanowires on TiO$_2$ nanotubes (TNWAs/TNTAs).

Phase structure and crystalline nature of TNTAs and TNWAs/TNTAs nanostructures were determined with X-ray diffraction (XRD) (Figure 2.11(a)). The XRD spectra of bare TNTAs shows various diffraction peaks at 2θ value 25.22º, 36.93º, 37.88º, 38.37º, 47.98º and 54.04º corresponded to (101), (103), (004), (112), (200) and (105) lattice plane of tetragonal anatase phase TiO$_2$ respectively, and well matched with JCPDS file # 21-1272 [56]. The presence of intense (101) peaks in XRD spectrum of TNTAs reveal the preferential (101) growth direction for TNTAs. After hydrothermal decoration of TNTAs

32

with TNWAs (TNWAs/TNTAs) in addition to anatase peaks some new peaks emerged at 2θ value 40.14º, 55.05º, 62.73º and 68.88º corresponded to (111), (211), (002) and (301) crystalline plane of rutile phase TiO_2 was in agreement with JCPDS file # 21-1276 [57]. However, the intensity of rutile phase TNWAs was weaker than anatase peaks, which might be due to low relative thickness of nanowire layer (approx.100 nm) to nanotubes.

The optical absorption properties of TNTAs and TNWAs/TNTAs nanostructures were determined with diffuse reflectance UV-Vis (Figure 2.11(b)). The DR UV-Vis spectra of TNTAs show a characteristic intense peak for anatase phase TiO_2 around 323 nm with an extended band tail up to 382 nm, originated due to transition of electrons from valance to conduction band. For the hierarchal structure of TNWAs/TNTAs, the absorbance was much higher than TNTAs, which was attributed due to the improved absorption *via* low band gap rutile phase TiO_2 NW layer. The presence of sharp band at 318 nm, with a band tail at 410 nm was in well agreement with rutile phase TiO_2. The observed absorption profile demonstrates presence of rutile phase TiO_2 nanowires on the top of anatase phase TiO_2 nanotubes which mainly contributing in UV absorption profile. From UV-Vis of TNWAs/TNTAs, it can be concluded that the hierarchal structure improves the optical absorption profile throughout UV-Vis spectrum, particularly in visible region, which in turn improves the photoactivity of light.

Further, optical band gap of TNTAs and TNWAs/TNTAs was calculated by using Tauc plot. The extrapolation of linear slope on X axis for graph between hν and $(\alpha h \nu)^{1/2}$ gave the value of optical band gap. Where α is absorption coefficient, h is plank constant and ν is frequency of light. The band gap value for TNTAs and TNWAs/TNTAs heterostructure assemblies was found to be 3.24 and 3.10 eV, respectively. The obtained low band gap

value for TNWAs/TNTAs further confirms that formation of nanowires/nanotubes hierarchal nanostructure improves the absorption profile of material.

(a)   (b)
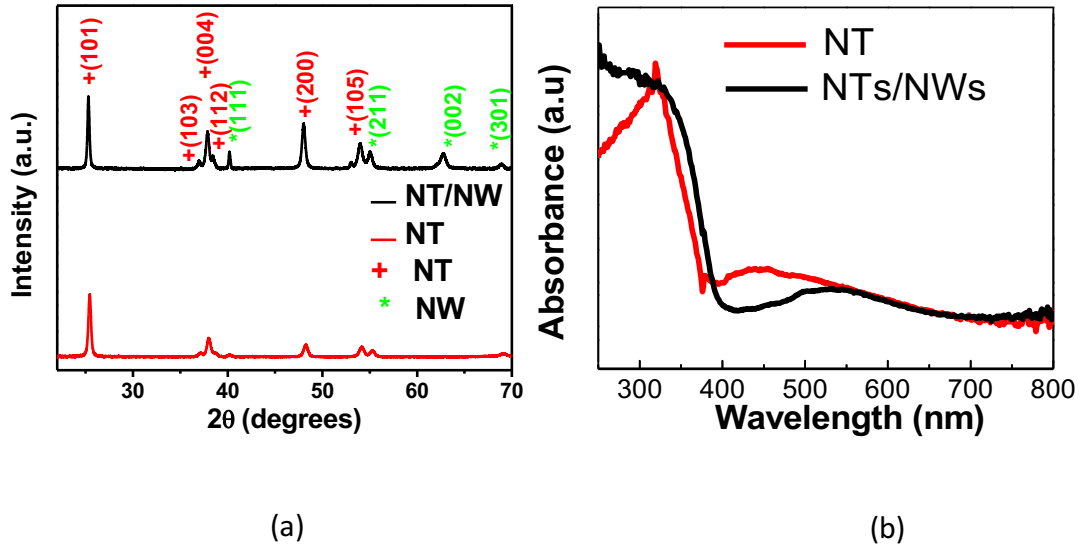
Figure 2. 11 (a) XRD spectra and (b) Diffuse reflectance UV-Vis spectra of bare TNTAs and TNWAs/TNTAs structure.

The presence of rutile and anatase phases in TNWAs/TNTAs nanostructures was further probed by Raman spectra (Figure 2.12(a)). Raman spectra of TNWAs/TNTAs exhibit Raman peaks at 148, 198, 395, 517.5 and 635 cm^{-1}. The Raman peak 198, 395, 517.5 and 635 cm^{-1} was corresponded to the E_g, $B1_g$, $A1_g$ and E_g vibration modes of anatase phase TiO_2 of TNTAs [35]. While weak Raman signal at 148 cm^{-1} might be originated from synergistic contribution of E_g mode of anatase TNTAs and B_{1g} mode of rutile TNWAs. The weak Raman signals for rutile phase TiO_2 and appearance of intense Raman peak for anatase phase implies presence of dense TiO_2 nanotube layer in comparison to TNWAs, which was in well agreement with XRD results.

To elucidate change in vibrational features of bare TNWAs/TNTAs and TNWAs/TNTAs nanostructure after functionalization with ODPA self-assembled monolayer (SAM/TNAWs/TNTAs) FTIR spectra of materials were collected in DRIFTS mode (Figure 2.12(b)). The DRIFT spectra of bare TNWAs/TNTAs nanostructures show IR peak at 840, 1620 and 3280 cm^{-1} assigned to Ti-O-Ti symmetric stretching, H_2O bending and -OH stretching vibration of –OH and surface adsorbed water. The peak at 2340 cm^{-1} was observed due to CO_2 in air. After functionalization with ODPA SAMs, the DRIFT spectra of SAM/TNWAs/TNTAs show signature peaks at 2850 and 2950 cm^{-1} due to CH_2 symmetric and anti-symmetric stretch of ODPA alkyl hydrocarbon chain respectively confirms successful functionalization of TNWAs/TNTAs with ODPA SAMs. Additionally, presence of peaks related to CH_2 bending, wagging and C–C stretching modes of alkyl chains in fingerprint region (500-1500 cm^{-1}) further prove successful grafting of ODPA on the surface of TNWAs/TNTAs. Further, presence of a weak peak at 1500 cm^{-1}, specific to P-O stretch of phosphonate group ($-PO_3$) in ODPA molecule reveals formation of phosphonate ester linkage ($ROPO_2-$) between TiO_2 and ODPA [58].
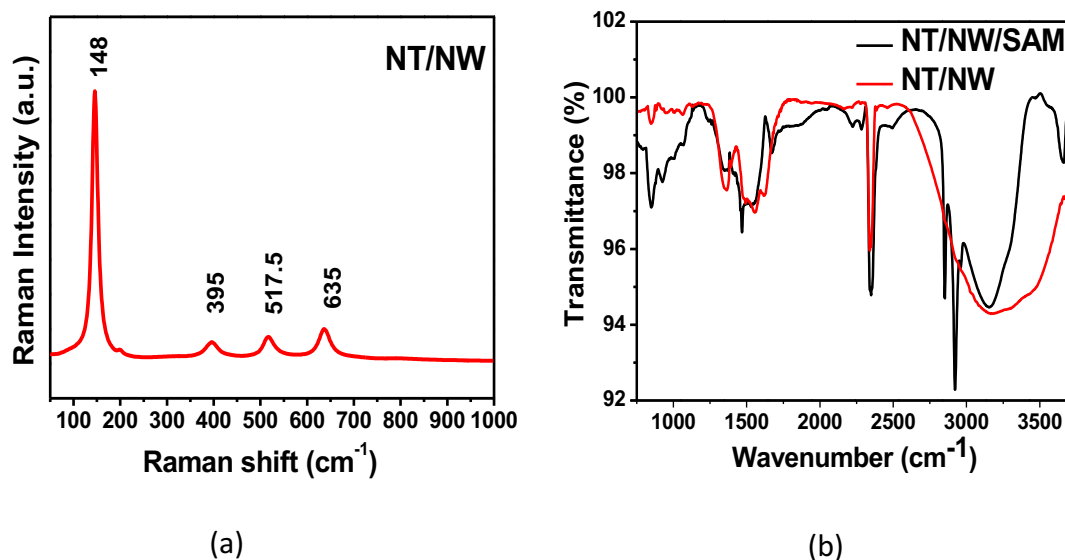
Figure 2. 12 (a) Raman spectra for TNWAs/TNTAs heterostructures (b) Fourier Transform Infrared (FTIR) spectra of the TNWAs/TNTAs and SAMs/TNWAs/TNTAs heterostructures.

Water contact angle (CA) measurement was employed on the surface of the hierarchical SAMs/TNWAs/TNTAs sample to validate their superiority over nanotubes structures. The value of CA is highly dependent on various parameters like morphological and surface characteristics of the material such as the TiO_2 nanotube/nanowire surface energy, roughness, and chemical/physical nature of SAMs *etc*.

 Both TiO_2 nanotube and nanowire surfaces due to hydrophilic surface present low water contact angles, which means high water wettability as reported earlier in the literature [59-61]. As predicted the synthesized hierarchical TNWAs/TNTAs heterostructures showed a low measured contact angle of 20° revealing strong hydrophilic natures.

Figure 2.13(a) and 2.13(b) illustrate the contact angles measured on SAMs/TNWAs/TNTAs immediately after functionalization and after four months of functionalization, respectively. The CA of SAMs/TNWAs/TNTAs just after

functionalization was found to be ≈ 180º much higher than CA value to attain superhydrophobicity (≈ 150º).

In fact, the SAMs/TNWAs/TNTAs structure repels water droplet too strongly that accurate measurement with the integrated camera was not feasible. This implies that SAMs/TNWAs/TNTAs heterostructure was perfect configuration for attaining super-hydrophobicity by forming Cassie Baxter state. The reason of excellent hydrophobicity can be explained based on formation of numerous brushes like nanowires structure, which provide maximum coverage of monolayers on NWAs resulting in minimizing contact between water droplets and TiO_2. Further, to check the longevity and resiliency the contact angle measurement on the surface of SAMs/TNWAs/TNTAs was performed after four months. The functionalized hierarchical structure of SAMs/TNWAs/TNTAs shows the same hydrophobic behavior (≈ 180°), even after the four-month time, reveals robustness of hierarchical structure. The SAM monolayer attached very well on engineered TNWAs/TNTAs heterostructure did not degrade over time, resulting in no change in contact angle over long time. The hierarchical structure mentioned here has a striking shift from NT and NW to the hybrid TNWAs/TNTAs structure, which could be attributed to participation of different features of these two nanostructures resulting in exceptional surface properties.
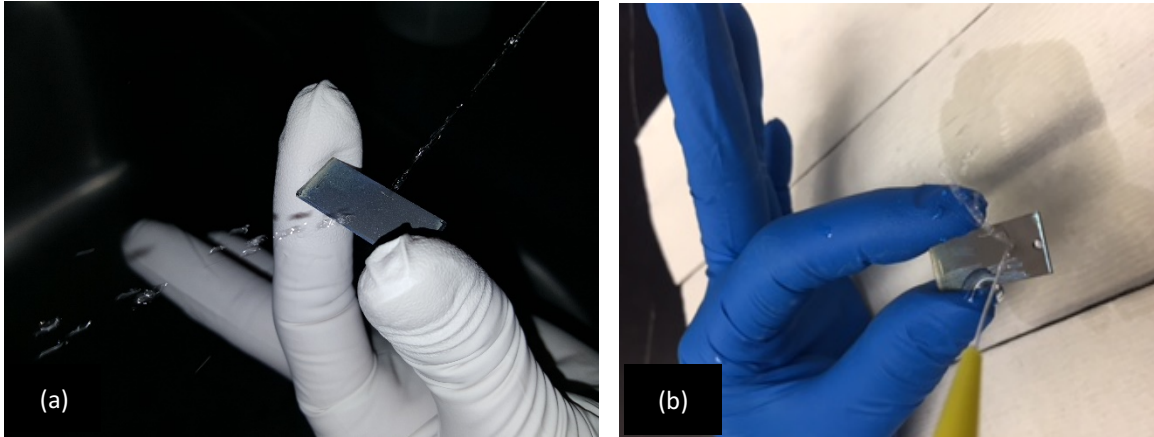
Figure 2. 13 Water contact angle of TNTAs/TNWAs/SAMs (a) immediately after fabrication and functionalization (b) after four months of SAM functionalization, illustrating that water will not pool or otherwise stay on the surface.

2.5 Conclusion

In summary, the hydrothermal method was employed to decorate rutile phase TiO_2 NWAs in and on the top of anatase phase TiO_2 NTAs arrays prepared *via* anodic oxidation of Ti foil. The hierarchical TNWAs/TNTAs nanostructure functionalized with ODPA SAMs presented superhydrophobicity with exceptionally high contact angle ($CA \approx 180°$), while TiO_2 nanotubes and nanowires possess hydrophilic surface behavior.

The method itself in growing nanowires hydrothermally on a TNTAs foundation has not been done previously, and the performed characterization in this study signifies that the resulting nanowires on nanotubes have nearly identical properties as if they were grown on their native substrates. However, the apparent difference in this work is the unexpectedly high contact angle after SAM application.

The samples show the same hydrophobic behavior after four months, which brings the striking possibilities of it being used in different applications due to the stability of

hydrophobicity despite the presence of hydroxyl groups. As a result, the mentioned novel structure has the best contact angle stability of TiO_2 that makes it special for some applications such as self-cleaning, anti-reflecting and anti-fogging surfaces. It is clear that, making the surface nano textured, maximizes the contact angles for wetting by decreasing the contact area and increasing the water repellence, a consequence of the Cassie-Baxter model.

Chapter 3 Fluoride-Free Solid-State Synthesis of TiO₂ Nanotube Arrays for Sunlight Driven Water Splitting Application

In this chapter we bring forward for the first time the facile fabrication of TiO$_2$ nanotube arrays (TNTAs) by a fluoride-free solid-state anodization process using LiClO$_4$ containing solid polymeric electrolyte. We believe; the elimination of liquid electrolytes in electrochemical anodization constitutes a paradigm shift for the formation of nanoporous and nanotubular metal oxides. The results presented in this chapter open a new area of research that uses the distinctive properties of solid polymer electrolytes to achieve targeted doping and nano-morphologies. We tested the resulting nanotubes for photoelectrochemical water splitting.

3.1 Introduction

The exponential rise of global energy demands and heavy reliance of modern civilization on fossil fuel has created serious environment concern and depleted fossil fuel reserves which brings up urgency to search alternative clean energy sources [1, 2]. Sunlight is an inexhaustible and continuous source of energy. Photocatalytic water splitting to generate hydrogen from water is an enticing approach to harvest solar energy in the form of chemical bonds in a sustainable way due to reliance on two most abundant sources, water

and sunlight [3-5]. Numerous, inorganic semiconductor oxides, sulfides, binary and ternary composites materials have been explored to catalyze the process of photocatalytic water splitting [6]. Among them, TiO_2 is most widely explored for the various photocatalytic applications i.e. water splitting, CO_2 reduction, pollutant and dye degradation etc. due to its wide abundance, non-toxic and non-corrosive nature, astonishing charge carrier mobility, appropriate band edge position etc. [7, 8]. As mentioned in previous chapters, TiO_2 exist in several allotropic forms like anatase, rutile and brookites. Anatase and rutile with a band gap of 3.2 and 3.0 eV respectively and corresponding absorption edge 389 and 413 nm respectively, are mainly investigated for photocatalytic applications. In Anatase form Ti^{4+} ions are surrounded by O^{2-} ions in octahedral manner giving rise to tetragonal geometry while rutile form having slightly orthorhombic distortion which is responsible to different band gap of two forms [9]. High temperature promotes transformation of anatase to more stable rutile phase. Surprisingly, even though low band gap of rutile phase, the anatase form exhibit higher photocatalytic performance owing to approximately 10 times slower charge recombination rate in anatase form [10]. Wide band gap and appropriate band edge position (CB, -0.58 V vs NHE at pH-7; VB, +2.52 V vs NHE at pH-7) of anatase TiO_2 produce oxidative holes which facilitate water oxidation (H_2O/O_2, +0.81 V vs NHE at pH-7) and reductive electrons to achieve reduction of protons to hydrogen (H^+/H_2, -0.42 V vs NHE at pH-7) which are prime requirement for sustainable production of hydrogen from water splitting [11, 12]. However, large band gap of TiO_2, which limits absorptions in visible regime, and detrimental charge recombination process are main obstacle to reach higher quantum efficiency. Several approaches like doping with metals, non-metals, sensitization,

heterostructures formation with low band gap semiconductors etc. has been employed to increase performance of TiO_2 [13-15]. In recent years, one dimensional TiO_2 nanostructures i.e. nanotubes and nanorods has gain significant attention in photocatalysis owing to their excellent electron mobility in ordered crystalline lattice, large surface area etc [16-19].

Electrochemical anodization in liquid electrolytes containing fluoride ions is currently used to form vertically oriented, self-organized TiO_2 nanotube arrays (TNTAs) [20]. TNTAs are an exciting nanomaterial platform due to their high surface area, tunable size range of the nanopores, n-type semiconducting behavior and the possibility of introducing periodicity in both the diameter and organization of the nanotubes [21].

TNTAs can be used in the form of discrete nanotubes in liquid suspensions, as thin films on transparent and non-transparent substrates, and as self-standing membranes [22-24]. Consequently, TNTAs have found a wide variety of applications ranging from energy harvesting to photonics to microfluidics to biomedical devices. The high refractive index contrast and periodicity achievable in TNTAs enabled researchers to demonstrate interferometric sensors [25] and photonic crystals [26] using TNTA platforms. The n-type semiconducting nature of TNTAs together with their high surface area renders TNTAs particularly attractive as photocatalysts, ultraviolet photodetectors and chemiresistive gas sensors [27-30]. N-type hollow titania nanotubes also form an excellent scaffold for the construction of heterojunction photovoltaic and photocatalytic devices following infiltration or decoration of the nanotubes by halide perovskites, conjugated organic semiconductors, noble metal nanoparticles and quantum dots [31, 32]. In TNTAs-based photocatalysts and solar cells, the engineering of periodicity in one or

more morphological parameters enables the introduction of nanophotonic enhancements through light trapping and resonant interaction with photons [19, 33-35]. The chemical resilience, biocompatibility, self-cleaning ability and high temperature resistance of TNTAs render them attractive for size-selective applications such as filtration membranes, drug delivery, stem cell differentiation and osseo-integration [36-39]. When we last checked, TNTAs in membrane form were being commercially sold by at least two vendors.

3.1.1 Introduction to the Fluoride-Free Solid-State Formation of Titania Nanotube Arrays

As discussed in chapter two about electrochemically anodized titanium dioxide nanotube arrays, there are variety of methods to synthesize TNTAs such as sol-gel, atomic layer deposition (ALD), use of nanoporous alumina templates, hydrothermal and electrochemical anodization methods. Here, in this thesis we applied electrochemical anodization method to grow titania nanotube arrays due to the great control over morphology and dimension of nanotubes. The TiO_2 nanotubes grown by anodizing the Ti is studied in detail in literature [18, 40, 41]. Chapter 2 explains the electrochemical anodization process and different steps involved in detail, whereas the as-prepared TNTAs are amorphous in nature and could be altered to whether anatase or rutile crystalline phases based on the applied annealing temperature. While numerous solution based anodization recipes have been devised to achieve the controlled growth of TNTAs, most of them rely on toxic and hazardous fluoride etchant. Furthermore, tedious handling and processing of the liquid electrolytic system, and field non-linearities and Debye

length limitations in macroscopic liquid electrochemical cells raise the question of whether the currently used TNTAs fabrication process is compatible with mass-production, scale-up and the extension to highly curved substrates. In this chapter, we demonstrate an all-solid-state process for the formation of titania nanotubes that dispenses with the use of liquid electrolytes. A several micrometer-thick film of a solid polymer electrolyte is used as the anodization electrolyte, thus dramatically simplifying and miniaturizing the growth apparatus and eliminating the need for a conventional electrochemical cell or Haber-Luggin capillary. The solid-state electrolyte we propose consists of less toxic lithium perchlorate dissolved in a hydrophilic polymer; we used PVA and PVP but in principle polyethylene oxide (PEO) and other biodegradable polymers could also be used. A major advantage of our choice of solid-state electrolyte is that $LiClO_4$-containing hydrophilic polymer electrolytes are well-understood, having been used in all-solid-state supercapacitors, lithium-organic batteries, dye sensitized solar cells and electrochromic devices [42-46]. The present work demonstrates a facile solid-state anodization process to synthesize TiO_2 nanotubes arrays (TNTAs) by using PVA and PVP solid matrix and $LiClO_4$ as etchant and subsequent application in sunlight driven water splitting. The obtained TNTAs exhibit robust morphological and crystalline anatase features and well performed in water splitting experiment depicts versatility of solid-state anodization process. To conclude; the solid-state anodization process provides several advantages over conventional solution-based electrolytes such as easy handling and processing, better charge transport, environmentally benign chemicals and methodology.

3.1.2 Introduction to the Photoelectrochemical (PEC) Water Splitting

The striking fossil fuels depletion and concomitant increased carbon emission, excelled research to search clean alternative energy technologies with minimum carbon footprints. Harvesting Sunlight by using photocatalysts to split water into oxygen and hydrogen is most appealing approach to fulfill energy demands in a sustainable way. Water splitting allows transformation and subsequent storage of solar energy into chemical energy [47]. Although photovoltaic devices can convert solar energy to electrical energy with specifically high efficiency, however their high cost due to extensive purification process, high payback period and requirement of grid storage are some associated drawback [48, 49].

The photocatalytic hydrogen production through water splitting relies on two easily accessible resources, Sunlight and water [50]. It can be realized by two different approaches: applying the photoelectrochemical cell by soaking a semiconductor electrode in water and illuminating with light in the presence of other carrier counter electrode (photoelectrochemical water splitting) and secondly applying the photocatalytic reactor by suspending the particles of a semiconductor photocatalyst in water, where the particle behave as micro-photoelectrodes to ease and accelerate the oxidation and reduction reactions of water on their own surfaces with applying any external bias (photocatalytic water splitting).

Fujishima and Honda presented the concept for the PEC water splitting of hydrogen production in 1972 [51]. Later, Khaselev and Turner were able to achieve the PEC solar-to-hydrogen conversion efficiency of 12.4 %. PEC technology, which is a combination of

two process of solar energy harvesting and water electrolysis in a individual device has drawn significant consideration. Fundamentally, the process involves dipping the suitable photoelectrochemical (PEC) semiconductor device in to an aqueous electrolyte followed by illuminating by sunlight. This results in photon energy turning to the electrical energy via generation of electron and holes at the semiconductor electrode, which in turn leads to water splitting to oxygen and hydrogen (chemical energy), a more stable energy form. There are two important factors to attain large-scale hydrogen production through water; visible light absorption and efficient charge separation. Although, numerous inorganic semiconductor photocatalysts has been explored by different groups, but still their quantum efficiency for large-scale hydrogen production in visible light remains too low for successful deployment.

Various criteria defining ideal PEC semiconductor system, to afford efficient PEC decomposition of water, include; generating adequate amount of voltage demanded for water splitting by illumination, small band gap to absorb the major fraction of the solar spectrum, straddling the hydrogen and oxygen redox potentials by the band edge potentials at the surfaces, long lasting stability in aqueous electrolytes for parameters such as corrosion. Finally, the charge transfer from the semiconductor (surface) to the electrolyte should be selective for hydrogen and oxygen evolution reactions and smooth enough to decrease energy losses originating from kinetic overpotential. The fundamentals of PEC are studied deeply in literatures [4, 52-57]. Fig. 3.1 shows the schematic of the photocatalytic water splitting reaction steps [47], where the photogenerated charge carriers (electrons and holes) in the semiconductor photocatalyst

particles move to the active sites in the semiconductor surface and finally they are consumed by surface redox reactions.
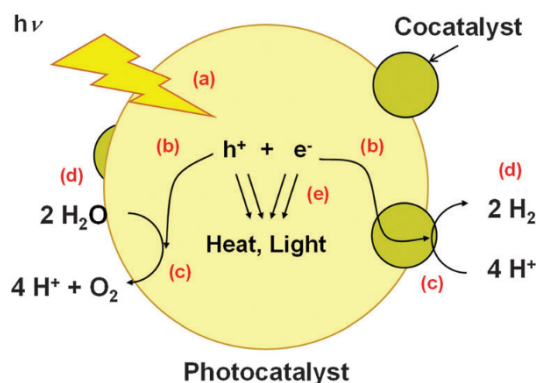
Figure 3. 1 Schematic of the photocatalytic water splitting reaction for a heterogeneous photocatalyst. (a) Light absorption, (b) photogenerated charge transfer, (c) redox reactions, (d) adsorption, desorption, and mass diffusion of chemical species, (e) charge recombination. Reprinted with permission from ref. [47] John Wiley and Sons 2010.

Photoexcited charge carrier recombination also occurs both at the surface and bulk of semiconductor and is the major process in water splitting reaction leading to poor performance. Decorating the surface of semiconductor by noble metal nanoparticles could minimize the surface recombination. The built-in field corresponded to the Schottky barriers [34]; resulted due to the semiconductor-metal heterojunction decrease the recombination happening at the semiconductor surface. As the other option is applying promoters–hole capturing agents [58, 59] or either to fulfill the catalytic reaction by involving the hole scavengers like alcohols. Using semiconductor particle with smaller size [60] or with modified surface morphology in water splitting process, result in decreasing the volume recombination, so the photogenerated electrons and holes can get to the semiconductor surface to be easily accessible to participate in photoreaction. As it

is also mentioned above; the best nanostructure semiconductor for photocatalytic water splitting reaction should have the visible light absorption and excellent charge separation in parallel and the maximum distance for photogenerated carriers to reach the chemical reaction side should be shorter than the recombination length [61, 62].

Creating a type-II p-n heterojunction, with an energy band offset in heterojunction interface, improves the charge separation and attenuates the geminate recombination. This is due to the diving force created in the interface of the p-n junction. In this type of heterojunction the low band gap p-type material is responsible for light absorption and as resulting photogenerated electrons move to the conduction band of n-type material, whereas the photogenerated holes stays in the p-type material reacts through direct mechanism with the reactants present on the semiconductor surface [63].

Z-scheme is another mechanism presents in combination of two low band gap semiconductors. One semiconductor has excess of electron and the other excess of hole, which are responsible for proton reduction and water oxidation respectively, although none of them can individually promote water splitting process. Photogenerated electrons in the oxidative semiconductor conduction band neutralize the photogenerated holes in valence band of in the reductive semiconductor whereas the holes in reductive semiconductor valence band and electrons in reductive semiconductor conduction band assist the water oxidation and proton reduction respectively. For Z-scheme, the presence of two photon is the critical criteria to facilitate water splitting [63]. Figure 3.2 demonstrates the schematics for direct and Z-schemes mechanism of water splitting by applying two different band gap semiconductors.
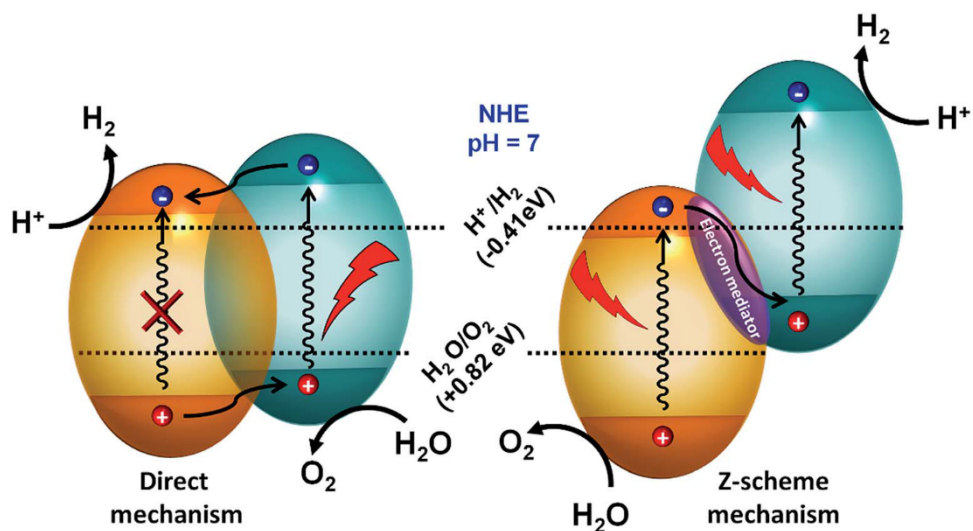
Figure 3. 2 Schematic of direct and Z-schemes mechanism of water splitting by applying two different band gap semiconductors. Reprinted with permission from ref. [57] Royal Society of Chemistry 2018.

Generally, water splitting includes firstly the water oxidation to obtain O_2, protons and electrons (OER) and secondly proton reduction to obtain hydrogen (HER), as depicted in equations 1-3. Both, HER and OER process should proceed together to encircle electrons flow.

$$2H_2O + h\nu \rightarrow 2H_2 + O_2 \tag{1}$$

$$2H_2O \rightarrow 4H^+ + 4e^- + O_2 \quad ; OER \tag{2}$$

$$4H^+ + 4e^- \rightarrow 2H_2 \quad ; HER \tag{3}$$

The principle for the one-step water splitting by using one semiconductor includes different steps; photon absorption for higher energies than semiconductor bandgap, photogeneated electrons transfer from semiconductor valance band to conduction band and as the result last step occurs which is the reduction and oxidation process. For the

one-step water splitting process by applying single semiconductor photocatalyst, the semiconductor band gap should be higher and conduction and valance band position should lie above and below of water reduction (0.00 V vs NHE at pH-0) and oxidation potentials (+1.23 V vs NHE at pH-0), respectively.

3.2 Materials and Methods (Procedure of Solid-State Anodization)

Titanium foil (thickness 0.89 mm, 99% purity, Alfa Aesar) was cut into 1 cm x 2.5 cm pieces to be used as anode, whereas a platinum sputtered glass substrate of the same size was used as the cathode for the growth of TNTAs by electrochemical anodization (Figure 3.3a). The electrodes were cleaned by ultrasonication in acetone, water and then methanol for 10 minutes each. In order to achieve solid state anodization, a solid electrolyte containing PVA (Polyvinyl alcohol with an average molecular weight of 89,000-98,000, procured from Aldrich), PVP (Polyvinyl pyrrolidone with an average molecular weight of 58,000, purchased from Acros organics) and inorganic salt $LiClO_4$ was prepared. $LiClO_4$ works as an etchant to facilitate nanotube growth while PVP also plays the role of a plasticizer. Firstly, PVA and $LiClO_4$ (99% purity purchased from Acros organics) were dried in a vacuum oven at 100 ^{o}C less than 100 mTorr for 5 h to remove moisture. Then PVA, $LiClO_4$ and PVP in a molar ratio of 0.3:1:1 were added to a minimum volume of DMF (N,N'-dimethylfomamide, procured from Aldrich) to obtain a viscous mixture. The obtained mixture was stirred and heated for ca. 1 hour at 120 °C to create a semitransparent gel, which was deposited on the Ti foil whose edges were covered with a Surlyn spacer (25 µm, Solaronix). Galvanostatic anodization was performed at room

temperature using a DC power source as depicted in Figure 3.3b and the instantaneous voltage across the miniature solid-state electrochemical cell was monitored using a Keithley-4200 semiconductor parameter analyzer. The amorphous as-prepared TNTAs on Ti foil with sealed Surlyn window, as observed in Figure 3.3c, were gently rinsed in methanol and dried with nitrogen blow and finally annealed for two hours under 450 ºC in a tube furnace to induce crystallization. Figure 3 provides a schematic illustration of the solid-state electrochemical anodization of TNTAs. For comparison, solution based TiO_2 nanotube arrays were also prepared by following our previous literature procedure [34]. Briefly, a Ti foil of size 1 cm x 2.5 cm assigned as anode and graphite cathode was immersed in an ethylene glycol (EG)-based electrolyte containing 0.3 wt.% NH_4F and 2 vol.% deionized water with the help of O-ring. Next 50 V voltage was applied with the help of a DC power source for initiating anodization process. The synthesized TNTAs surface was cleaned with oxygen plasma treatment for 10 min.
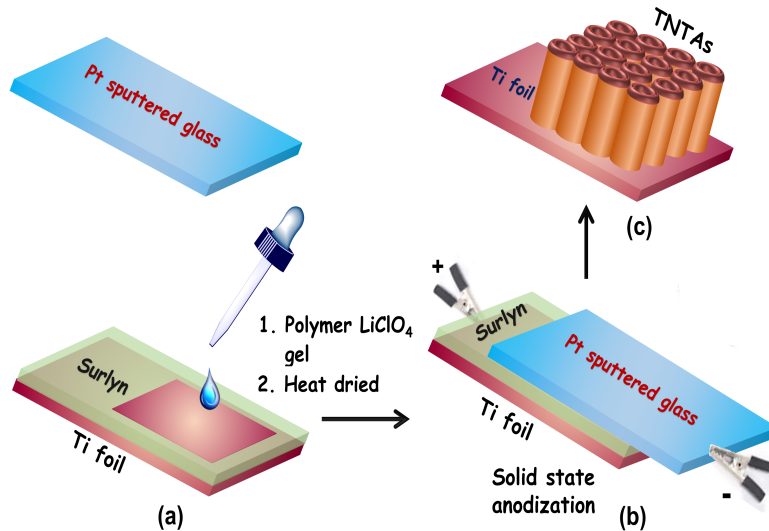
Figure 3. 3 Schematic illustration of solid-state anodization of TNTAs (a) Deposition of $LiClO_4$:PVA:PVP gel over Ti foil having Surlyn window (b) Solid state anodization by applying constant current and (c) Growth of TNTAs on Ti foil.

The microstructure and morphological features of TNTAs samples were determined using a Hitachi S -4800 field emission scanning electron microscope (FESEM). The ultrafine microstructure of TNTAs was evaluated with the help of high resolution transmission electron microscopy (HR-TEM) by using JEOL JEM-ARM200CF S/TEM with EDX working at an acceleration voltage of 200 kV. The samples for the TEM were prepared by scratching the surface of Ti substrate by using a blade to detach the nanotubes. The obtained sample suspended in methanol to make a very dilute solution followed by deposition on carbon coated copper TEM grid and dried. The phase structure and crystalline nature of TNTAs were discerned by X-ray diffraction patterns acquired using a Bruker D8 X-Ray diffractometer (XRD) with a CuKα radiation source ($\lambda =$ 1.5406 Å). The characteristic Raman scattering energies of the TNTAs were collected using a Nicolet Omega XR Raman Microscope with a laser excitation wavelength of 532 nm and an incident power of 24 mW cm^{-2}. To probe the applicability of prepared TNTAs in photoelectrochemical water splitting, experiments were performed on three electrodes system on a CHI600D potentiostat while the photoelectrode was illuminated by near-monochromatic light from light emitting diodes (LEDs). In the three-electrode system, TNTAs grown on Ti foil and a Pt sputtered glass were used as the anode (working electrode) and cathode (counter electrode) respectively, while a saturated KCl solution containing Ag/AgCl glass electrode was the reference electrode. Prior to measurement, the surface of working electrode was sealed with Surlyn in such a manner that only a circle with 0.3167 cm^2 area was exposed for electrochemical measurement. The electrolyte used was an aqueous 0.1 M KOH solution. The TNTA photoanode was irradiated with LED light of different wavelength and the obtained photocurrent was

measured by linear sweep voltammetry by sweeping the bias from –0.8 V to +0.8 V. LEDs of different wavelength were calibrated with the help of a photodiode to determine the photon intensity at the surface of sample and to obtain comparison data under identical irradiation conditions. The distance between LED and TNTAs surface was 5 cm while the measured power of light at the surface of the samples was adjusted to be 47.7 mW cm^{-2} for 365, 410, 425, 450, 505, 585, and 640 nm LEDs by respectively setting their drive current values. The photocurrent density was calculated by dividing the obtained current by the exposed surface area. A measurement in dark was also obtained to compare the observed photocurrent with the dark current.

3.3 Results and Discussion

Field emission scanning electron microscope (FESEM) images of TNTAs cross-section and top-view are displayed in Figs. 3.4 (a and b) in ESM, respectively. The FESEM images show that solid-state anodization triggers the growth of a uniform nanotubular TiO$_2$ layer over Ti foil having a layer of thickness ~ 2 µm and an average diameter ~ 50 to 60 nm. Top view electron micrographs confirm the existence of an open top end. Further, it can be seen from SEM top view that some regions were no fully occupied with nanotubes, which represent imperfect growth in comparison to liquid-based anodization. High resolution transmission electron microscope (HRTEM) images of nanotube samples were collected determine fine structure of TNAs (Figures 3.4c-3.4e).
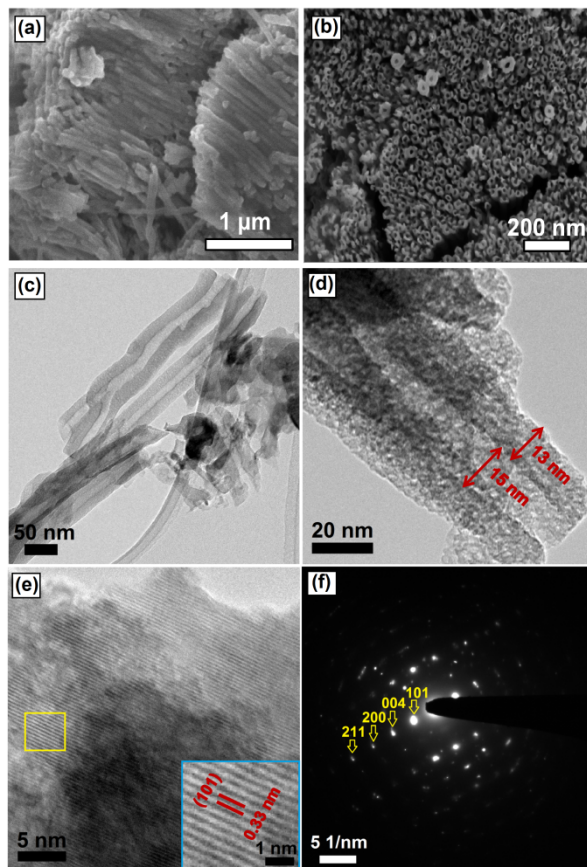
Figure 3. 4 FESEM images of TNTAs showing (a) Cross-section, (b) Top-view and (c), (d), (e) HR-TEM images at scale bar of 50 nm, 20 nm and 5 nm respectively. The inset in (e) shows the interplanar d spacing, and (f) SAED pattern.

The TEM images of TNTAs at 50 nm scale bar show hollow nanotube structures (Figure 3.4c). The external diameter and wall-thickness in the TEM image at 20 nm scale was calculated to be $\sim$ 40-45 nm and $\sim$ 15-16 nm respectively (Figure 3.4d). Further resolution at 5 nm scale reveals lattice fringes possessing interplanar d-spacing of 0.33 nm, corresponding to the (101) plane of anatase TiO_2 (Figure 3.4e and inset). The presence of sharp spots in selected area electron diffraction pattern (SAED) of TNTAs due to (101), (004), (200) and (211) lattice plane confirms the presence of crystalline anatase form TiO_2 (Figure 3.4f).

The crystalline nature and phase structure of solid-state synthesized TiO_2 nanotubes structures was investigated using X-ray diffraction (XRD). The XRD pattern of TNTAs exhibits various diffraction peaks at 25.37°, 48.09°, 53.95° and 55.05° indexed to (101), (200), (105) and (211) planes of tetragonal anatase TiO_2 respectively, consistent with JCPDS# 21-1272 [64] and previously reported literature (Figure 3.5) [65] [66]. The absence of any peak related rutile or brookite phase in XRD of TNTAs confirms phase pure anatase TNTAs. The intense peaks in XRD diffractogram indicate that the TiO_2 nanotubes were well crystallized. The XRD peaks of TNTAs were comparable to those formed by anodization in EG based solution electrolyte [67]. However, the presence of sharp Ti peaks reveals the grown nanotubes structures were incontinuous. Additionally, the average grain size of nanotubes was calculated by using Scherrer equation (eqn. 4).

$$L = K\lambda/\beta \cos\theta \tag{4}$$

Where, L is average crystallite size, K is a dimensionless constant related to crystallite shape (assumed as 0.9), λ is the wavelength of X-ray in nm (0.154 nm, source Cu Kα), β is peak width at half of the maximum intensity in radians (obtained from FWHM of (101) anatase peak), and θ is the Bragg angle. From the expression the average crystallite size of TNTAs was found to be 36.01 nm.
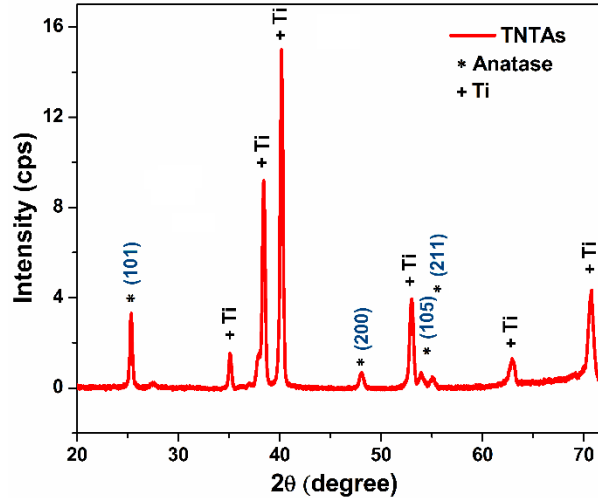
Figure 3. 5 X-ray diffraction pattern of TNTAs.

The Raman spectrum for the TNTAs is shown in Figure 3.6 where characteristic peaks are seen at 157, 207, 402, 514 and 632 cm^{-1} that were indexed to the E_g, E_g, $B1_g$, $B1_g+A1_g$ and E_g active mode vibrations of tetragonal anatase phase TiO_2. No peak for rutile phase TiO_2 was observed [68-73], which indicates the phase purity of the prepared samples, consistent with XRD results. The strongest E_g mode at 157 cm^{-1} originates from the symmetric stretching vibration of the oxygen atoms in O–Ti–O bonds. A small shifting of Raman signal to higher frequencies except for the 514 cm^{-1} peaks was observed for solid state grown TNTAs then solution based TiO_2 nanotubes. These variations in Raman peaks were attributed due to presence of defects originating in solid based electrolyte method, compared to solution-based electrolyte anodization method TiO_2 nanotubes. Further, carbon doping from residual polymeric matrix during annealing process might contribute to slight shift of Raman signal.

56
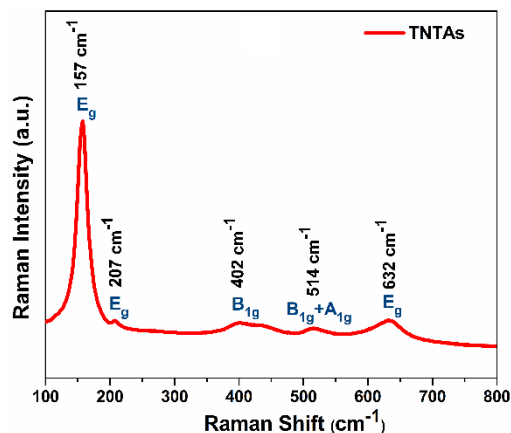
Figure 3. 6 Raman spectra of solid state grown TNTAs.

In conventional aqueous and organic electrolytes, the growth of TNTAs occurs first by oxidation of the Ti to produce a barrier layer (hence decreasing the anodization current), followed by pitting (a slight increase in current) and then pore ordering and barrier layer thickening (a slow monotonic decrease in anodization current), as explained in chapter 2 [74-76]. Thus, observation of the anodization current transient provides an effective means to understand, monitor and optimize the TNTA growth process. However, in the solid-state electrolytes used in this study, an unusual featureless plateau in the anodization transient was observed for the growth of TNTAs (see Fig. 3.7a and Fig. 3.7b). Thus, the fundamental processes and dynamic equilibria governing the formation of TNTAs in $LiClO_4$-containing solid polymer electrolytes could be somewhat different from the situation in liquid electrolytes, and require further study and elucidation. It is also well-established that the initial stages of the anodic growth of TNTAs in liquid electrolytes are limited by the solid-state transport of ions through the barrier layer [41]. Mass transport limitations are known to occur later in the anodization process when the nanotube length is already significant (> 1 µm) due to which the diffusion of fluoride ions

to the barrier layer as well as the diffusion of freshly created protons (Ti + 2H$_2$O → TiO$_2$ + 4H$^+$) away from the barrier layer, becomes the rate limiting step. In the all-solid-state anodic synthesis of TiO$_2$ nanotubes, the higher viscosity and concomitantly lower ionic mobility in solid polymer electrolytes may generate mass-transport limited growth much earlier than in liquid electrolytes. A detailed study of the mechanism(s) governing all-solid-state growth of TNTAs is outside the scope of the present study but is planned in follow-up work.
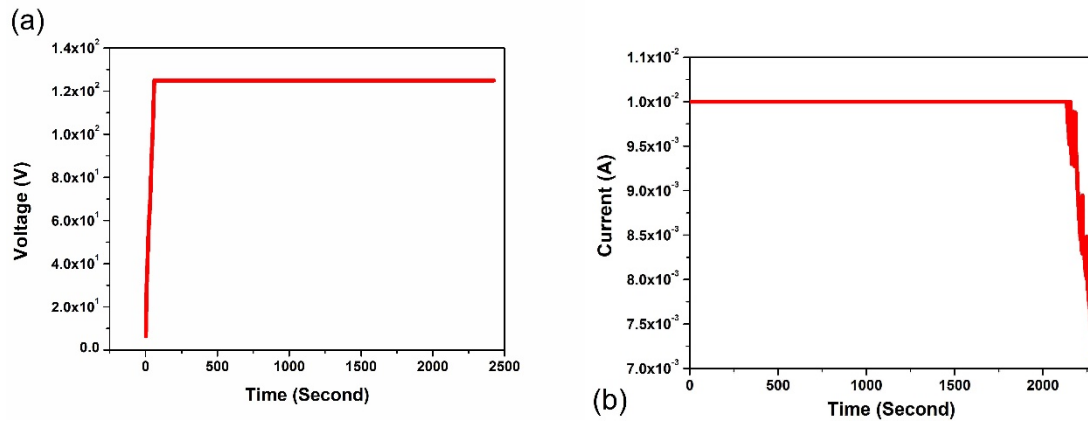
Figure 3. 7 (a) Potential difference between the cathode and the anode monitored during the galvanostatic all-solid-state anodization of Ti foil with the compliance set to 125 V and (b) Cell current monitored during the potentiostatic all-solid-state anodization of Ti foil at 80 V with the compliance set to 10 mA.

UV-Vis diffuse reflectance spectra of TNTAs show a sharp absorption band around 360 nm due to transition of electrons from valence band to conduction band (O1s→Ti3d) (Figure 3.8a). The UV-Vis diffuse reflectance spectrum of TNTAs was used to generate a Tauc Plot, from which the bandgap of the TNTAs was determined to be 3.05 eV (Figure 3.8a; Inset). The long band tail in the UV-Vis spectra indicates the presence of defects remaining after the calcination step [60].

The grown TNTAs were tested for photoelectrochemical measurements in 0.1 M KOH (pH-13) electrolyte to validate the applicability in solar energy harvesting. For the measurement, TNTAs and Pt were used as the working and counter electrode and the obtained photocurrents were measured with respect to Ag/AgCl reference electrode. The TNTA photoanode was irradiated with light from different LEDs. After absorption of light of sufficient energy, electron hole pairs are produced in TiO_2, which is an n-type semiconductor. The photogenerated electrons in the conduction band of TiO_2 are extracted by the positive anode and migrate to Pt cathode via the external circuit where they generate hydrogen at cathode. The photogenerated holes in the valence band are used for the oxidation of water or OH^- to generate oxygen, electrons at the anode.

$TiO_2 \rightarrow TiO_2\ (h^+ + e^-)$ (Photoexcitation)

$OH^- + 4h^+ \rightarrow O_2 + 2H_2O$ at Anode

$4H_2O + 4e^- \rightarrow 2H_2 + 4OH^-$ at Cathode

Figure 3.8b shows linear sweep voltammograms of TNTAs measured at different incident optical wavelengths while maintaining identical illumination intensity (47.7 W cm^{-2}) under irradiation with different LEDs. Under dark conditions a very miniscule current density was observed. The highest current density was observed for the 365 nm wavelength, which was 0.85 mA cm^{-2} at 0.6 V applied bias (vs Ag/AgCl). Significant photocurrents were observed even at higher wavelengths, which might originate from defect-mediated excitation. Applied bias photoconversion efficiency (ABPCE %) values for TNTA samples at various wavelengths were calculated and plotted against applied

potential at reversible hydrogen electrode (RHE) scale – this is shown in the inset of Figure 3.8b.
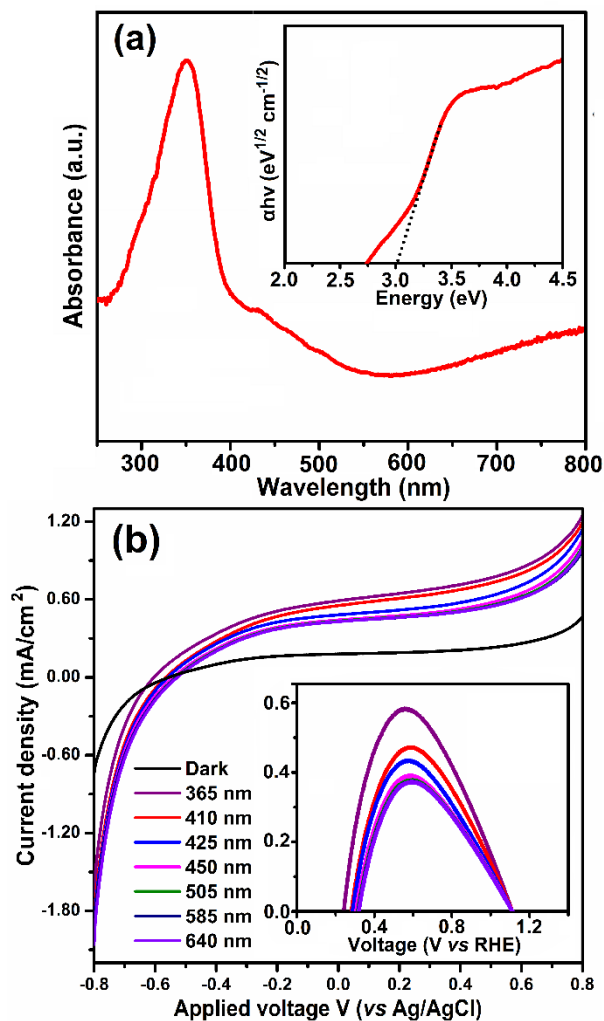
Figure 3. 8 (a) UV-Vis DRS spectra of TNTAs, inset shows Tauc plot for band gap determination (b) Plot of photocurrent density as a function of applied voltage (vs Ag/AgCl) for illumination by LEDs of different wavelengths having a power density 47.7 mW cm^{-2} at the sample. Inset shows plot of PCE (%) vs potential at RHE scale for different LED wavelengths – dark (black), 365 nm (purple), 410 nm (red), 425 nm (blue), 450 nm (magenta), 505 nm (green), 585 nm (navy blue) and 640 nm (violet).

3.4 Conclusion

Conclusively, we have demonstrated a solid-state anodization strategy to fabricate TNTAs in a solid electrolyte containing $LiClO_4$, PVA and PVP. $LiClO_4$ salt works as etchant and facilitates nanotube formation while PVA and PVP provide dissolved moisture and hydroxyl groups for oxidation while also enabling the transport of ions in the solid state. The TNTAs obtained in solid electrolyte system were well developed and composed of the anatase phase as confirmed by FE-SEM, HR-TEM, XRD and Raman etc. The solid state anodized TNTAs exhibited comparable morphological and crystalline feature as for TiO_2 nanotubes grown in solution-based electrolyte. Compactness of fabrication apparatus, highly efficient use of reagents, easy handling and processing, use of less toxic inorganic salts and the possibility of use of a biodegradable polymer matrix, makes the process more versatile and environment-friendly. The applicability of grown nanotubes arrays was probed by photoelectrochemical water splitting using various wavelengths' LEDs. The solid state grown TNTAs exhibited promising photocurrent response, which demonstrate viability of solid-state anodization process for future applications.

Chapter 4 Investigation of PbS Quantum Dot Thin Films Grown by SILAR Method on TiO₂ Nanostructures for Photocatalytic Dye Degradation

The main aim for this chapter is to research the fabrication of TiO$_2$ nanotube/nanowires decorated by PbS quantum dot heterostructures (TNTAs/PbS and TNWAs/PbS) and subsequent application in decolorization of different dyes as model for waste water treatment. Firstly, we will provide an introduction of structural and optical features of TiO$_2$ nanotube/PbS quantum dot heterostructure and their emphasis in photocatalytic dye degradation. The detailed insights to the SILAR method for growing PbS quantum dot on the TiO$_2$ nanotube, characterization of heterostructures using various advanced techniques like, FE-SEM, UV-Vis, XRD, Kevin Probe Force Microscopy (KPFM) and mechanism of dye degradation will be discussed.

The results presented in this chapter enabling the successful formation of visible light absorbing 1D/0D heterojunction of TiO_2 nanostructure by using low band gap chalcogenide quantum dots i.e. PbS. The potent application of their heterojunction composite in pollutant degradation along with visible light responsive devices was envisaged for future application.

4.1 Introduction

The demands for organic dyes has increased significantly due to their vast application in different industries such as cosmetics, paints, colorant and so on. The disposal of untreated water in water bodies has created a serious problem of water pollution and extinction of aquatic flora and fauna. As most of the disposed organic dyes absorb visible light and reduce the visibility and light penetration depth resulting disturbance of aquatic ecosystem. So, treatment of waste water prior to disposing in water bodies is vital for heathy ecosystem. Dye degradation is a major process, which should be considered to obtain a dye free harmless environment for safe and clean water [1]. Although, different approaches such as filtration, coagulation, adsorption on porous absorbents and so on has been employed to obtain a dye free/and or decontaminated water [2-4]. However, these methods have some innate drawbacks such as transformation of the dyes to other toxic phases, permeability of low molecular weight fragments of degraded dyes through the filtration membrane and much more [5]. In recent year photocatalytic dye degradation

using various inorganic semiconductors is gaining popularity due to their robustness, nontoxicity, no input of energy and high efficiency. Due to the destructive characteristic of advanced oxidation processes (AOPs), we will employ this technique for photodegradation of dye in this study. The best photoactive devices should satisfy the criteria of being cost effective and extensive for solar light absorbers.

TiO_2 1D nanostructure (nanotube and nanowire) has attracted great attention for different applications such as water splitting, gas sensing, CO_2 reduction and environmental purification [6-11]. It is also considered as a good photocatalyst eliminating a variety of organic contaminant [12-14] due to its remarkable characteristics including being highly photoactive, cost-effective, non-toxic, earth abundant nature, resiliency and so more [15]. The large effective surface-to-volume ratio, radial direction size confinement for highly ordered array for tubular or wire shape structure are important factors for improving the photoactivity of material, made TiO_2 nanostructure a great candidate for photoactivity [16, 17].

It is recommended to use solid support substrates to grow TiO_2 nanostructure on top of that to achieve an immobilized system. The immobilized 1D structures are desirable because of following three factors 1) problematic nature for long-lasting systems, 2) particles aggregation and 3) the critical demand for separation or filtration steps followed by photodegradation reaction [18, 19]. It worth to mention that the 1D nanostructures provide active surface for the immobilization of other substrates/semiconductors which overcome the deficiency of low total active surface area of immobilized catalyst and recyclability [20].

Electrochemical anodization in liquid electrolytes, is the most facile and quick method to obtain highly ordered and self organized TiO_2 nanotube arrays [21]. Anodization potential and annealing temperature are two important factors in running steps of anodization process to achieve different tube diameter and crystalline phases, respectively [22, 23], which have great impact on photocatalytic behavior of nanotube arrays [24, 25]. To fabricate TiO_2 nanowire arrays, hydrothermal growth is the best method to achieve great control over the composition on large area good-quality samples.

Illuminating the TiO_2 nanostructure by UV light carrying energy equal or greater than the semiconductor bandgap results in the electron (e^-) and hole (h^+) pairs generation on the catalyst surface, which are reductant and oxidant respectively. Later, the photogenerated charge carriers engage in direct redox reactions with present organic contaminants. As the result of the aforementioned steps of TiO_2 irradiation, charge separation and redox reaction, the present organic pollutants photocatalytically get degraded. The photogenerated charge carriers also can have react with water, oxygen and OH^-, which leads in the formation of a highly reactive family such as superoxide ($O_2^{\bullet-}$) radical anions and hydroxyl radicals ($\bullet OH$), resulting in oxidation and reduction of present contaminants.

Many groups studied the effect of sunlight for dye degradation using TiO_2 nanostructures [26, 27]. There is a big issue related to applying solar light for TiO_2 as photocatalyst is its wide band gap, which is 3.2 eV so it can absorb only in UV light. Since, the UV light is high cost and dangerous. So, there is a strong need to develop visible light absorbing catalyst. One way to develop the photocatalytic behavior of TiO_2 is to sensitize or making heterojunction of TiO_2 with low bandgap semiconductors [28, 29].

This could be approached towards applying different metal chalcogenide nanoparticles or quantum dots (QDs) such as CdS, CdTe, CdSe, PbSe, $CuInS_2$ and PbS. Among these, Lead sulfide (PbS) nanoparticles have great potential to be applied in different applications such as infrared electrodevices, solar light absorbers and photoconductors [30, 31]. PbS quantum dots could increase the photocatalytic behavior of TiO_2 due to different factors including multiple exciton generation, strong separation of photogenerated electron-hole and suppressing the recombination process [32].

Its wide ranging direct band gap covers the variation from 0.41 eV (at 300 K) to 2.3 eV [30, 31] and it absorption coefficient increases over the wide spectrum range through visible from infrared. PbS quantum-dots (QDs) also carry great potentials due to their large Bohr radius of 18 nm, high absorption coefficient, multiple exciton generation, large dipole moment and wide range bandgap as mentioned above [30, 33-35]. Numerous methods could be applied to deposit PbS chalcogenides including electrodeposition [36], chemical bath deposition (CBD) [37], successive ionic layer adsorption and reaction (SILAR) [38, 39], gas phase atomic layer deposition [40] and spin coating, which greatly influence properties of PbS [41]. Among the mentioned methods SILAR has benefits such as being facile synthesis, low cost, safe, eco-friendly, facile, excellent reproducibility.

There are two methods to deposit PbS QDs on TiO_2 nanostructure, ex-situ and in-situ. Ex-situ is the method to deposit the synthesized colloidal PbS QDs on TiO_2 nanostructure [42, 43], where as by in-situ method the QDs grow right on the TiO_2 nanostructure by SILAR or CBD method [44-46].

This work mainly focuses on the PbS quantum dot growth on different nanostructures of

TiO$_2$ by the SILAR method as well as studying the photocatalytic behavior of fabricated heterojunction of TiO$_2$ anatase phase nanotube (TNTAs) and rutile phase nanowire (TNWs) with PbS quantum dot for dye degradation. The obtained TiO$_2$/PbS heterostructure was characterized by different tools of scanning electron microscopy (SEM), Kelvin probe force microscopy (KPFM), ultraviolet photoelectron spectroscopy (UPS), photoluminescence (PL) and X-ray diffraction (XRD) etc. The photocatalytic activity of TiO$_2$ nanostructure/PbS heterostructure was tested for the photodegradation of rhodamine B (RhB) and crystal violet (CV) under solar simulator.

4.1.1 Introduction to Heterogeneous Photochemistry of Dye Degradation Using TiO$_2$ Photocatalyst

The photocatalytic dye degradation reaction uses the heterogeneous photochemistry in order to reduce the present dye using the semiconducting properties of the involved semiconductor, and is dependent on wavelength or light (photon) energy and the present catalyst. Generally, the catalysts are semiconducting materials, which sensitize the light irradiation leading in redox processes.

Solid semiconductors have different electrons conduction that isolated atoms, due to their closely packed molecular orbital in energy, which could be mentioned as bands of energy compared to the present discrete energy levels regarding their atomic orbital. The high-energy conduction band and low-energy valance band are separated with the band gap energy of the material.

In semiconductors, the electrons which occupied the valance band moves to the non-occupied conduction band by means of photoexcitation and leaves a vacancy or hole behind in the valance band. These generated electron and hole either can react with dye molecule directly to reduce and oxidize dye molecule respectively, leading to their degradation or reacts with dissolved oxygen and water molecules to create highly active superoxide anions and hydroxide radicals, which oxidize dye molecule. It is interesting that generated superoxide radicals can react with proton/water and generate hydroxyl radical (•OH). The present electron and holes experience successive steps of oxidation and reduction with adsorbed species on the semiconductor surface. The schematic of the mentioned steps for a semiconductor material is presented in Fig. 4.1.

In fact, the dye degradation process involves chemically breaking the large dye molecules to obtain products including carbon dioxide, water and/or mineral byproducts. Mere breaking of chromophore bonds in dye molecule leads to decolorization of water. However, small molecule (benzene derivatives) still exists in water, which might be more toxic than original dye for aquatic environment. So, complete degradation of dye molecules (also called mineralization) is desirable for sustainable water treatment.
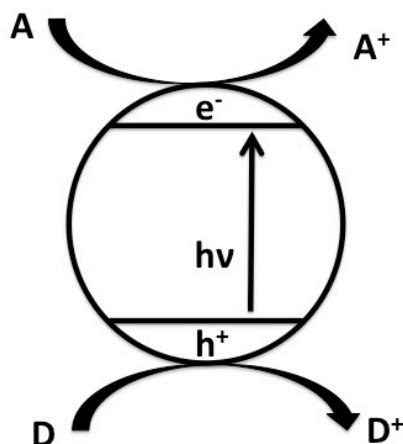
Figure 4. 1 The schematic for the photoexcitation of electron from valance band to the conduction band of the semiconductor and participating in redox reactions.

The absorbed water on the surface of the photocatalyst is oxidized due to the presence of photogenerated holes to generate hydroxyl (•OH) radicals, which have excellent oxidative decomposing power and react with the react with adsorbed organics dye leading to decomposition. The existence of oxygen and their reaction with electrons leads in radical chain reactions creating intermediate radicals like superoxide ($O_2^{•-}$), hydroxy peroxyl (•OOH), H_2O_2 and finally •OH radical. These steps cause the decomposition of the organic material to water and carbon dioxide [47-49].

The accompanying reaction, which is an alternative for the hydrogen generation, is the reduction of oxygen present in the air [48]. The photogenerated electrons and the dissolved oxygen species react and form the superoxide anions. Later, the anions attach to the intermediate products of oxidative reaction and result in peroxide formation or either a change to hydrogen peroxide and consequently to water. The reduction process is more probable in organic material rather than in water and highly concentrated organic

materials increase the number of present positive holes. It results in the lower carrier recombination rate and higher photocatalytic activity rate [47, 49]. Figure 4.2 presents the radical generation and organic dye degradation of a metal oxide semiconductore by photoirradiation.
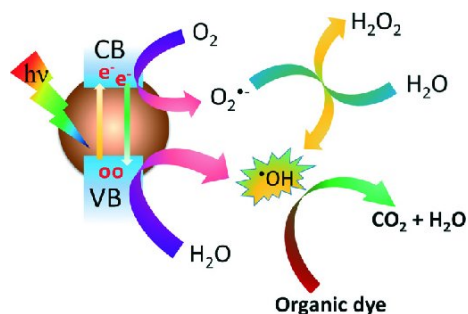
Figure 4. 2 Radical generation and organic dye degradation of a metal oxide semiconductore by photoirradiation. Reprinted with permission from ref. [51] Royal Society of Chemistry 2015.

The valence band of TiO_2 is significantly deeper than the water oxidation potential to generate •OH radicals. So, the produced hydroxyl radical has more oxidative character. TiO_2 is more preferred to be used as oxidizing agents rather than reducing agent, since the hole oxidizing power is significantly more compared to the reducing power of electrons [52].

The photocatalytic oxidation reactions of semiconductor material, which leads in mineralization of toxic organic pollutants, got a vast attention to study deeply on [52, 53].

4.1.2 Introduction to the Successive Ionic Layer Adsorption and Reaction (SILAR) Method

Successive ionic layer adsorption and reaction (SILAR) method is a facile fabrication process with a variety of advantages compared to the other thin film fabrication methods [54, 55]. These benefits include great control over the deposition rate and film thickness, obtaining almost uniforms films independent of the substrate material, being non-vacuum, cost-effective and low temperature.

The new method of SILAR, which is a revised form of chemical bath deposition (CBD) method, is used to grow a thin film of different materials [56, 57]. These thin films are binary chalcogenide groups of I–VI, II–VI, III–VI, V–VI, VIII–VI and ternary chalcogenides of I–III–VI, II–II–VI, II–III–VI, II–VI–VI and II–V–VI. Figure 4.3 presents the schematic for the SILAR method. The method includes the ion adsorption and reaction from solution and rinsing step following each reaction to prevent the possible homogeneous precipitation in the solution.
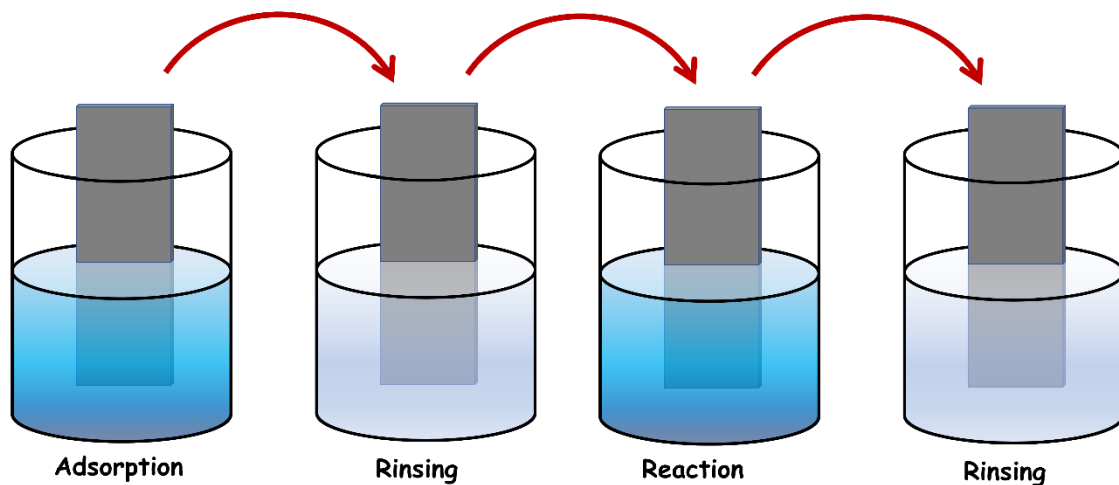
Figure 4. 3 Schematic illustration for the SILAR method.

Adsorption is the first step of SILAR method. The basic idea behind this method, is collecting the substance on the surface of the other substrate surface, and due to contact of two materials with different phase. Adsorption is the outcome for the reaction between the substrate surface and present ions in solution originating from the attractive holding them together, which could be chemical, van-der Walls or cohesive attraction. The cations of the precursor solution adsorb to the substrate surface. It is followed by the rinsing step of the loosely adsorbed cations away from the surface. The third step of SILAR is the reaction between the anions from anionic solution and adsorbed cations resulting in film formation. The final step is rinsing the excess species, unreacted species and the byproducts away from the surface.

The processes in all these steps are affected by different factors including solution temperature, solution pH concentration, the nature of the substrate and its area, dipping and rinsing time etc. [54]. Temperature plays a key role in dissociation of complex and the anion present in the compound. A higher temperature results in greater dissociation, higher concentration for anions and cations and consequently higher deposition rate of the grown thin film. The compound concentration has a direct relation with cation and anion concentration and therefore film thickness, but the further increase of concentration above a certain value results in precipitation and consequently lowering the thickness. The film growth rate would increase by controlling the release or adsorption of metal ions via using a complexing agent. Uniform films of SILAR, which could be achieved by equal adsorption and reaction time, results in a consistent growth of film. Rinsing is also an important factor to decreases and eliminates the precipitation in the reaction bath and

giving enough time for rinsing causes the loosely bounded pieces on the substrate to be peeled off.

Along these lines, SILAR method takes place by cations adsorption and their reaction with adsorbed anions during the following step. This results in thin film formation of the desired material.

4.1.3 Introduction to Kevin Probe Force Microscopy

There are different methods to measure the surface potential or work function of the material including Kelvin probe (KP), scanning electron microscopy (SEM) with electron beam induced current (EBIC) and photoelectron spectroscopy (PES) and Kelvin probe force microscopy (KPFM).

Comparing the KPFM to KP, their working mechanism is close whereas the KPFM is a mapping method but the KP is averaging technique and supplies the averaging for contact potential difference (CPD) values of the whole material. SEM would measure the EBIC and provide the local electronic structure for the surface of semiconductor [58]. PES counts the energy of the photo-stimulated electrons, which are free from the surface. In literature, there is a detailed study of advantageous and disadvantageous of these method [59]. KPFM has coincident mapping of potential or work function and topography, which make it special enough tool for electrical characterization of the nanostructure with semiconductor and metal nature. However, we used KPFM to study the topography and surface potential of the TNTAs/PbS and TNWAs/PbS samples.

KPFM is first introduced in 1991 by Nonnenmacher et al. [60] and is vastly used for

characterizing the nanoscale electrical and electronic characteristics of metal, semiconductor surfaces, semiconductor devices and electrical characteristics of organic, biological materials, organic devices [61-63] by imaging the material surface potential in nanoscale range. Its operation is based on measuring the local contact potential difference of the tip for conducting atomic force microscopy (AFM) and the present sample, which is mainly mapping the surface potential or work function of the sample by applying high spatial resolution. Recently KPFM is applied to image the potential distributions on the material or device surface with resolutions in the order of sub-nanometer, which make KPFM a great method to electrically characterize the nanostructures. KPFM measures the present CPD, which is highly sensitive to the force between tip and material, of the tip and material surface. The working mechanism for intermediate and non-contact mode is based on the cantilever oscillation at its resonance frequency or close to that, whereas the resonance frequency and oscillation amplitude (intermediate mode) depends on the tip-sample interaction as a function of their distance to each other. The topography of the sample surface for intermediate and non-contact mode, which are introduced as amplitude modulation (AM) and frequency modulation (FM) operation modes respectively, are attained by monitoring the amplitude and frequency variations corresponding to the reference amplitude and frequency. The energy loss due to the oscillation, which determines the quality factor (Q) of the vibrating cantilever, is the main factor to define the AFM resolution [63] and ultra high vacuum operated FM mode results in an increased Q and accordingly higher AFM resolution [59]. The ultra high vacuum prevents the system from contamination that causes a perturbation in potential profiles. The KPFM determines the CPD (V_{CPD}) present between the sample material and

conducting AFM tip, which depends on the tip and sample work function [59]. The formed electric force between the sample material surface and AFM tip is the result of bringing the tip close enough to the material surface to cause a difference in Fermi energy level of the material surface and tip. Later, the material surface and the tip will be charged resulting in a formation of V_{CPD}. At this step, the KPFM can measure the material work function by imposing a combination of AC voltage and DC voltage to the AFM tip, which forms and nullifies the oscillating electrical force between AFM tip and material surface respectively. The AM mode in KPFM has similar mechanism to AM and FM modes of AFM and identifies the electrostatic force by cantilever oscillation, whereas the KPFM FM mode finds the gradient of electrostatic force by frequency change in cantilever oscillation and it results in a higher spatial resolution for the FM mode of KPFM [65, 66].

4.2 Experimental and Discussion

4.2.1 Electrochemical Anodization of TiO$_2$ Nanotube, Hydrothermal Growth of TiO$_2$ Nanowire and PbS Quantum Dots Growth by SILAR Method

TiO$_2$ nanotube arrays were grown by using electrochemical anodization method and the details are given elsewhere [67]. A 500 nm sputtered Ti metal film was subjected to anodization in a highly conductive electrolyte, 0.3% NH$_4$F in ethylene glycol (EG) + 4%

H_2O, and the anodization voltage is about 40 V. The as-anodized TNTAs have amorphous nature and undergo a two-hour heat treatment step at temperatures around 500^0C. TiO_2 nanowire arrays were grown by hydrothermal growth method. The solution contains 5 mL of deionized (DI) water, 2.5 mL hydrochloric acid, and 2.5 mL acetic acid and 0.2 mL titanium (IV) butoxide (97%, Sigma Aldrich). They all were loaded to a Parr autoclave followed by heating at 180 ºC for 2 h. FTO was placed into the autoclave as well. As the result, small diameter vertically oriented TNWAs were grown on FTO. The TNWAs were taken out, rinsed with DI and dried under nitrogen blow, once the autoclave reaches the room temperature.

PbS thin film composed of smaller sized quantum dot into and on the substrates by using SILAR method at room temperature. The same concentration of 20 mM lead (II) iodide and sodium sulfide (Na_2S) dissolved in methanol (MeOH) were used as cationic and anionic precursor respectively. The TiO_2 nanostructure present on the FTO substrate was immersed in cationic and anionic precursor respectively for 6 cycles each for 60 sec. Each step was followed by a rinsing step with MeOH for 90 sec; the TNTAs/PbS and TNWAs/PbS samples were dried in air and kept in an air tight container.

4.2.2 Structural and Morphological Characterization

The bare TiO_2 nanostructures, TNTAs/PbS and TNWAs/PbS samples were imaged using the field emission scanning electron microscope (FESEM, Zeiss Sigma), equipped with Gemini column, operating at the acceleration voltage of 5 keV. Figure 4.4 represents the top- and cross sectional view for TNTAs, TNWAs, TNTAs/PbS and TNWAs/PbS. The top-view FE-SEM images of bare TiO_2 nanotubes represents that they have open top end

which makes the surface to be easily accessible for potential PbS growth (Figure 4.4 (a).

The SEM images for TNWAs show the highly compact and vertically oriented TiO_2 nanowires, which lets the PbS grow on top and seldomly between the wires (Figure 4.4 (a)). The top- and cross-sectional images of TNTAs/PbS and TNWAs/PbS represents the presence of PbS quantum dot thin film on top of both nanostructure, and quantum dots, and clusters between neighboring tubes and wires.

X-ray diffractograms (Bruker D8 Discover instrument), which has a sealed Cu Kα X-ray source (40 kV, λ = 0.15418 nm) and is equipped with a LynxEYE 1-dimensional detector, was used to perform the crystallinity characterization. The XRD analysis given in Figure 4.5 (a) show the formation of multi-phase anatase/rutile phase for TNTAs and rutile phase for TNWAs. There in no extra pattern observed for PbS coated TNTAs/PbS and TNWAs/PbS samples which could be due to the low amount of PbS quantum dot on both nanostructure, and the PbS pattern may be submerged by background noise [68, 69].

The optical absorption properties of TNTAs/PbS and TNWAs/PbS heterostructures were determined with Ultraviolet-visible spectroscopy (UV-Vis) performed by using a Perkin Elmer Lambda-1050 UV–Vis-NIR spectrophotometer, which is equipped with an integrating sphere accessory. Ultraviolet photoemission spectroscopy (UPS) performed with a 21.21 eV He lamp source was used to determine the work function and valence band maxima of samples.
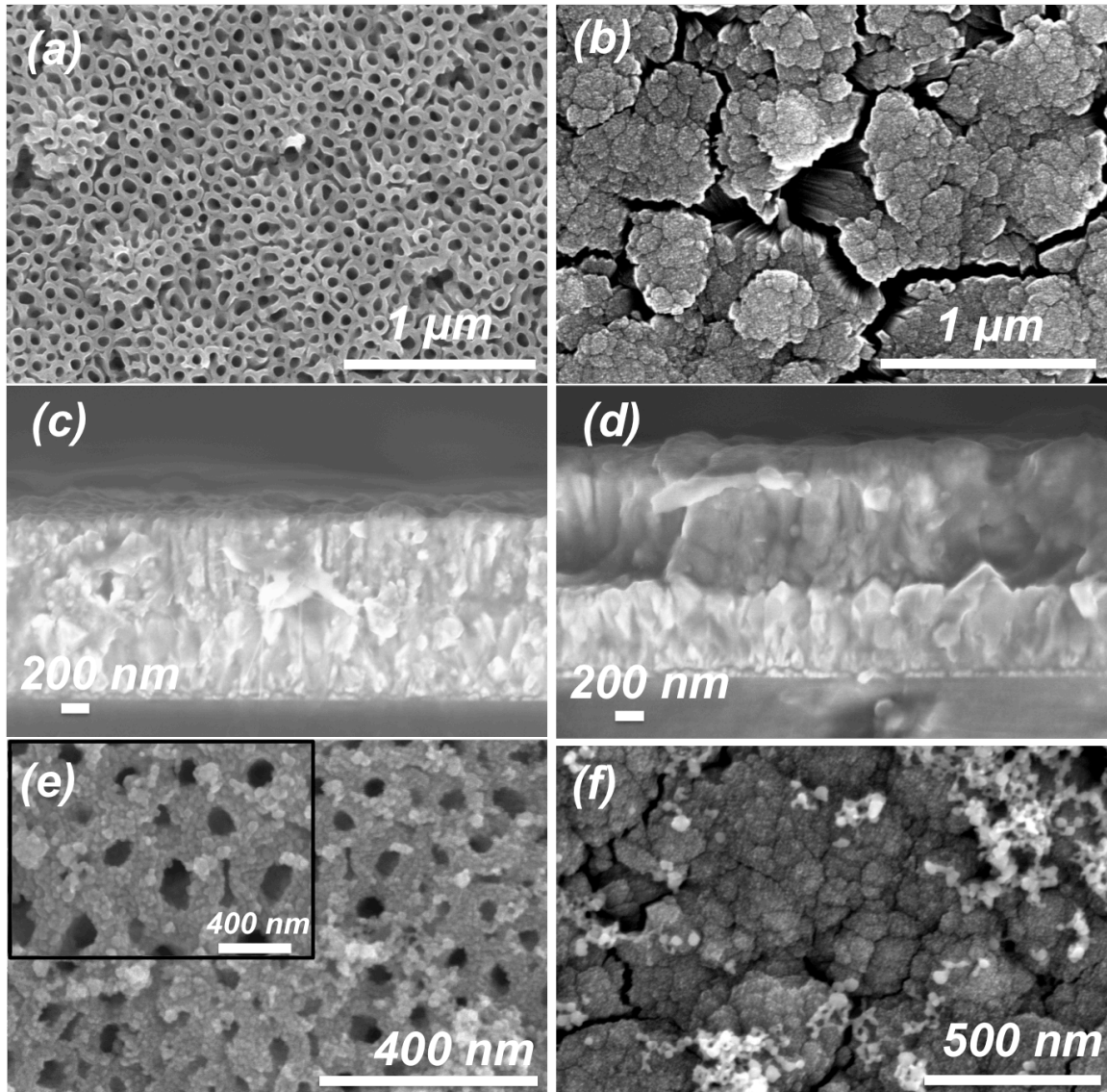
Figure 4. 4 Top-view SEM images (a) TNTAs and (b) TNWAs, cross sectional images of (c) TNTAs/PbS and (d) TNWAs/PbS (d) Top-view SEM images (d) TNTAs/PbS, (e) TNWAs/PbS.

As it is observed in Fig 4.5 (b) the TNTAs and TNWAs highly transmit the visible light at the wavelength above 400 nm. The presence of PbS dramatically decreases the UV light transmission and enhances the absorption due to the low band gap of PbS. So, the PbS quantum dots are great candidates to furnish the TiO_2 nanostructures to harvest the visible light.
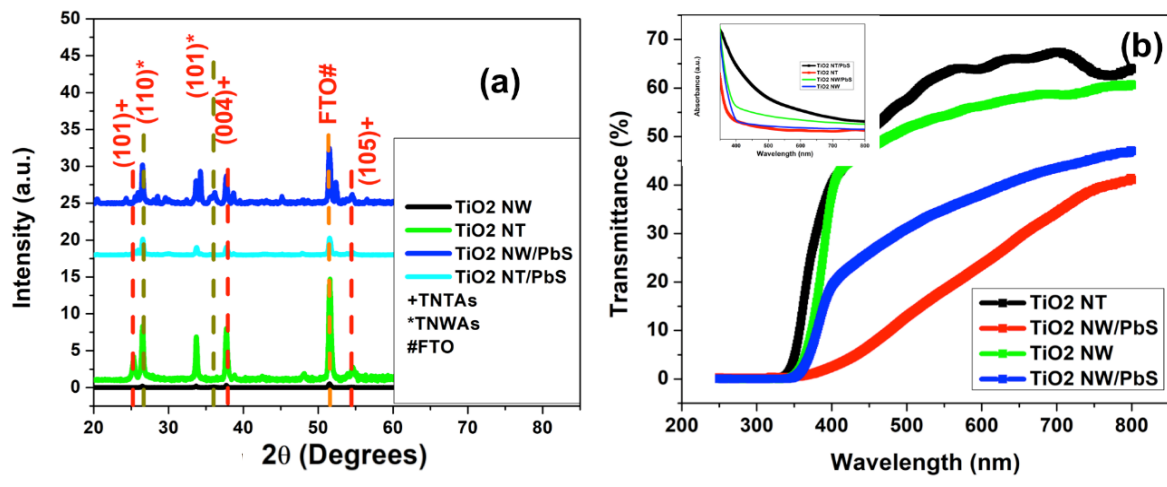
Figure 4. 5 (a) XRD spectra and (b) Transmittance UV-Vis spectra of bare TNTAs and TNWs/TNTAs structure.

To investigate the electronic band structure of PbS quantum dots modified nanotube structure ultraviolet photoelectron spectroscopy (UPS) work function (WF) spectra was measured. The value of work function was calculated from work function spectra by using following expression WF $(\phi) = 21.21 - E_{cut-off}$, where 21.21 eV is the energy of the incident, He I laser light, and $E_{cut-off}$ is the cut-off energy of emitted secondary electrons. The intersecting point by extrapolation of linear region of graph in horizontal and vertical axis gives the value of cut-off energy of secondary electrons ($E_{cut-off}$). The $E_{cut-off}$ for compact PbS/TiO$_2$ (TNTAs) was found to be 17.05 eV and the value of WF was calculated to be 4.16 eV (Figure 4. 6). The obtained value of WF was slightly higher than the value for pristine anatase phase TiO$_2$ (4.04 eV) demonstrating Fermi level get slightly uplifted after adding PbS quantum dots. Further, the low energy region of WF spectra give important information about the position of valance band. The intersecting point of

extrapolated linear region in low energy cut-off region gives the value of valance band (Figure 4.6 a). From the graph the valance band position of PbS/TNTAs was determined to be 3.17 eV below the Fermi level. The obtained value of VB slightly lower than TiO_2 (3.2 eV) suggesting reduced band gap of hybrid materials.
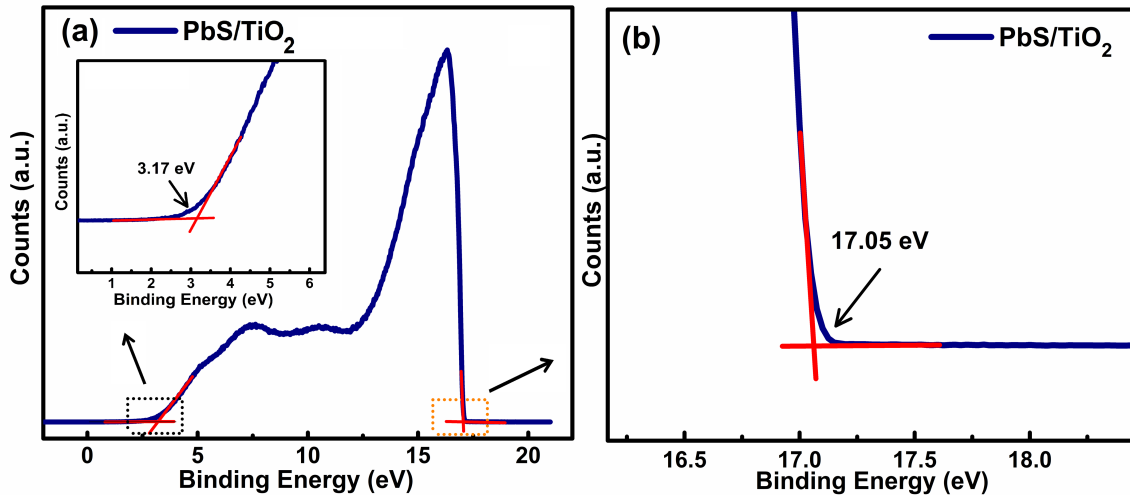
Figure 4. 6 (a) UPS work function spectra of PbS/TiO_2; Inset showing valance band position below Fermi level obtained by extrapolation linear regions in low energy cut-off region and (b) Enlarged UPS work function spectra of PbS/TiO_2 showing value of work function; The work function (WF) were determined from the UPS work function spectra by using the equation: WF (ϕ) = 21.21 − $E_{cut-off}$, where 21.21 eV is the energy of the incident He laser used for UPS. Insets on top right show UPS valance band spectra illustrating the estimated values of valence band maximums, below Fermi level.

4.2.3 KPFM Topographical Characterization

Peak force KPFM experiments were conducted on PbS-TiO_2 nanotubes and nanowires using Bruker Dimension Fast Scan AFM equipment, as it is shown in Figure 4.7. Pt coated SCM-PIT cantilever (from App Nano, Santa Barbara) was used to carry out

KPFM experiments. The frequency of the cantilever while doing KPFM was kept at 2 kHz frequencies and the imaging was done at a scan speed of 0.5 Hz and of 3x1.5 cm^2 area. The samples were grounded using copper conducting tape.

While doing AFM two channels were used to collect the data. One is the topography and the other one is the surface potential. The surface potential of the two different samples i.e. PbS-TiO$_2$ nanowire and PbS-TiO$_2$ nanotubes were collected without and with light. Three different wavelength lights (i.e. 450 nm, 520 nm and 635 nm) were used to collect the data and the average surface potential of the area was plotted with and without light. The work function of the Pt tip was calibrated by using the standard graphite sample and it was found to be 5.05 eV.

The topographical image of PbS/TNWAs demonstrates several nanoparticles morphology with an average roughness of 11 nm while the average roughness of PbS/TNTAs was found to be approx. 3 nm. Further images demonstrate the nanoparticles were more agglomerated on the TiO$_2$ nanowires in comparison to TiO$_2$ nanotubes. The surface potential map under dark condition depicts uniform distribution of charge on both PbS/TNWAs and PbS/TNTAs samples. However, after irradiation with light the average distribution of blue spots was increase demonstrating charge generation on the surface of samples under irradiation conditions. The value of surface potential measured by KPFM under dark conditions for PbS/TNWAs was found to be ~ +80 mV demonstrating slightly positive surface which might be due to presence of surface adsorbed Pb^{2+} ions. After irradiating with 450 nm light the SP was negatively shifted (~ 90 mV) which demonstrate generation of charge and accumulation of electrons on the surface of the sample. However, under 520 and 635 nm irradiation the SP does not change significantly which

demonstrate negligible contribution of low band gap PbS in charge generation on PbS/TNWAs samples. Further, the observed SP shift at 450 nm was assumed due to low band gap of rutile phase TiO₂ nanowire which can absorb certain fraction of 450 nm light due to presence of defects. Contrarily, PbS/TNWAs samples also displayed +220 mV surface positive charge under dark condition, however under 450 nm irradiation a drastic negative shift of approx. 480 mV was observed which demonstrate excellent charge generation. Further, under 635 nm almost same negative shift (471 mV) was observed which clearly reveal PbS quantum dots are playing an important role in charge generation leading to better photocatalytic performance of later as confirmed from dye degradation results.
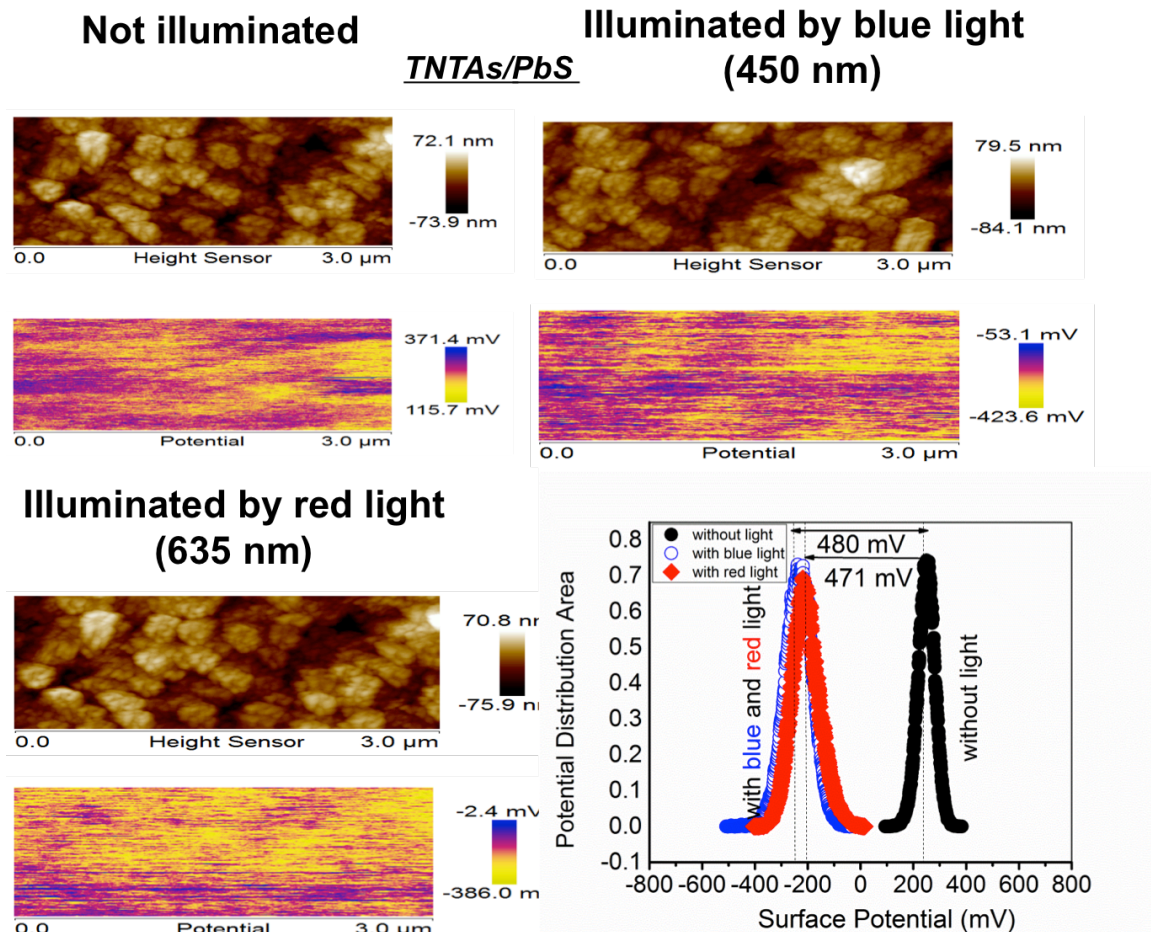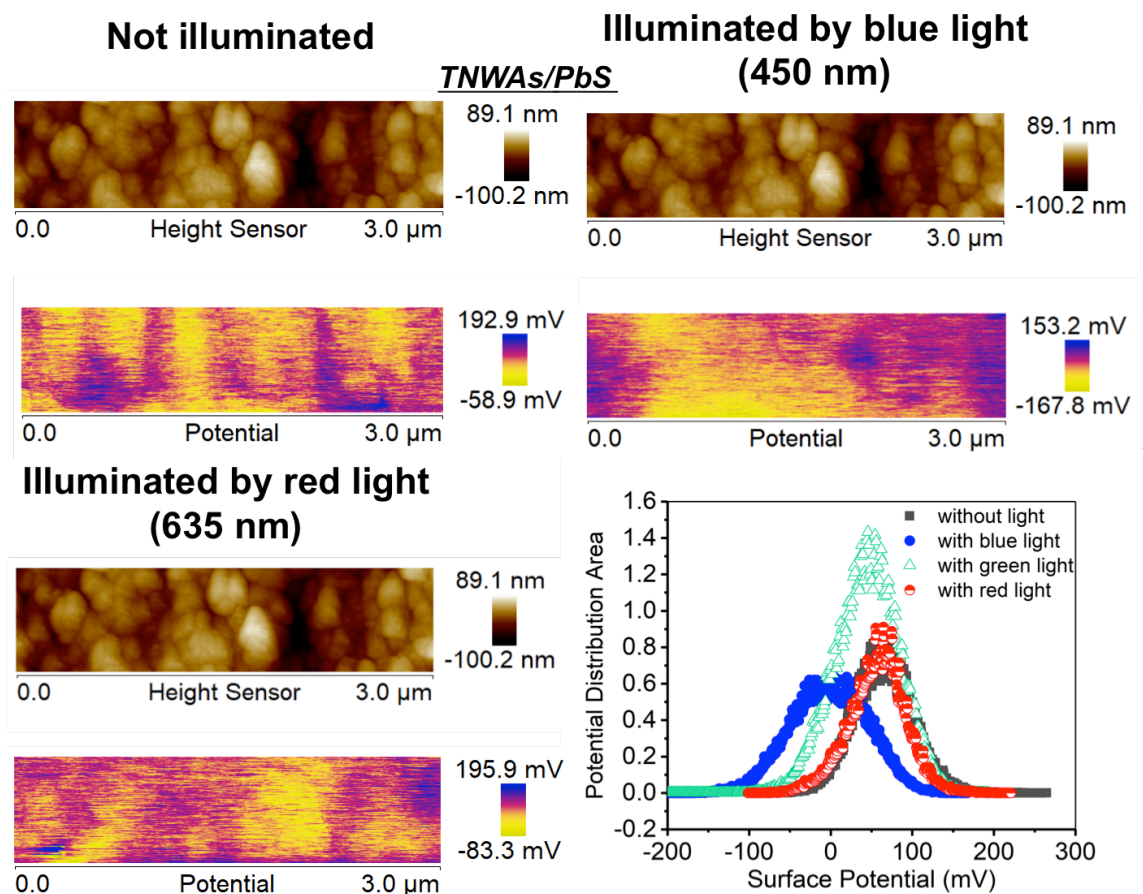
Figure 4. 7 Topographical AFM images and surface potentials (SP) map under dark, and under illumination with 450 and 635 nm laser Top: TNWAs/PbS; Bottom: TNTAs/PbS   Right top: Surface potential distribution of TNWAs/PbS; Right bottom: Surface potential distribution of TNTAs/PbS under dark, and under illumination with 450, 520 and 635 nm laser.

4.2.4 Dye degradation test

To check the viability of developed structures photocatalytic dye degradation experiment were carried out using rhodamine B and crystal violet as model substrate. A set of photocatalytic degradation experiments of rhodamine B (RhB) and crystal violet (CV) dye were performed under a solar simulator light source (Newport Class A solar simulator with AM1.5 G radiation) positioned at distance of 10 cm from the solid

sample/dye solution beaker and the intensity of light on the surface of the solution was 100 mW cm^{-2}. The photocatalytic activity tests of FTO/TiO$_2$/PbS photocatalyst, were performed at room temperature using different nanostructures of TiO$_2$ including TiO$_2$ nanowire arrays and TiO$_2$ nanotube arrays as the substrate for lead sulfide (PbS) growth. The TNTAs/PbS and TNWAs/ PbS photocatalyst structures were placed at the bottom of the beaker with dimensions of 1×1 cm^2 and 2.5×2.5 cm^2 respectively. 25 mL of the dye solution with an initial concentration of 1 ppm was introduced into the beaker.

Firstly, the reactor was in dark condition for 60 min to ensure that the adsorption/desorption equilibrium on the surface of the photocatalyst has been reached. Later, the light source was switched-on for 100 min. During the first 60 min, samples were taken from the reactor with 30 min intervals, where as for the rest 100 min the interval of withdrawing the samples was 20 min. Decomposition of the dye was easily monitored by analyzing the light absorption of samples using Perkin Elmer Lambda spectrophotometer. The identical procedure was used to study the dye degradation mechanism of FTO/TNTAs/PbS photocatalyst in presence of the radical scavengers (methanol and EDTA) using rhodamine B and crystal violet dyes and radical scavengers (50 mmol) in the solution. The photodegradation of different dyes was analyzed by monitoring the $\frac{C}{C_0}$ versus time, where C_0 and C are the original and residual concentration of the applied dye present in the solution respectively.

The photocatalytic degradation of RhB and V dyes for different nanostructures of TiO$_2$ was measured under solar simulator irradiation and is presented in Figure 4.8.

It can be seen from the graph that TiO$_2$ nanotube represented better photocatalytic activity toward the degradation of both RhB and CV dye in comparison to nanorod

structure and PbS incorporation greatly improved the photocatalytic activity. The best photocatalytic behavior was obtained for TiO$_2$ NT/PbS photocatalyst for crystal violet dye degradation. The TiO$_2$ NT/PbS photocatalyst has almost complete degradation (95%) of crystal violet dye within 100 min under solar simulator radiation. For pristine nanotubes only 70 and 20% degradation of RhB and CV were afforded. For pristine nanowire and PbS decorated TiO$_2$ nanowires, almost no degradation was observed. After decoration of PbS quantum dots on nanotubes, almost complete degradation of both RhB and CV was observed which demonstrates that nanotubes are specific for the optimal degradation of dye which might be due to the deeper valence band and better charge separation in PbS/TNTAs hybrid due to formation of a heterojunction.

Dye degradation can be promoted via various active radical species generated during photoirradiation. To investigate the possible mechanism of dye degradation and to identify active species responsible for dye degradation, a series of dye degradation experiments were carried out on TiO$_2$ NT/PbS/V and TiO$_2$ NT/PbS/RhB system using methanol and ethylenediamine tetraacetic acid (EDTA) as hole scavengers. It is observed from Fig. 5.7 that the photodegradation performance of TiO$_2$ NT/PbS structures significantly decreased in presence of both hole scavengers. The obtained results clearly demonstrate the great role of holes, which generates active •OH radical. So, the role of PbS in the process can be defined as photosensitizer (light absorber) which increase the visible light reactivity of TiO$_2$ nanotubes structure leading to enhanced dye degradation performance. The overall process can be represented as follows:

PbS/TNTAs + hν → e$^-$ (CB) + h$^+$ (VB) PbS/TNTAs

h$^+$ (VB) PbS/TNTAs + dye → oxidation (degraded dye) …………..…………Major path

h^+ (VB) PbS/TNTAs + H_2O → •OH radicals

•OH radicals + dye → degraded dye (oxidation) ……………………………..Major path

O_2 (ads) + e^- (CB) → $O_2^{•-}$ (ads)

$2H_2O + h^+$ (VB) → $4H^+ + O_2 + 4e^-$ (transferred in VB of TiO_2)

$O_2^{•-}$ (ads) + dye → degraded dye (including •OOH, •OH etc.) ………………Minor path
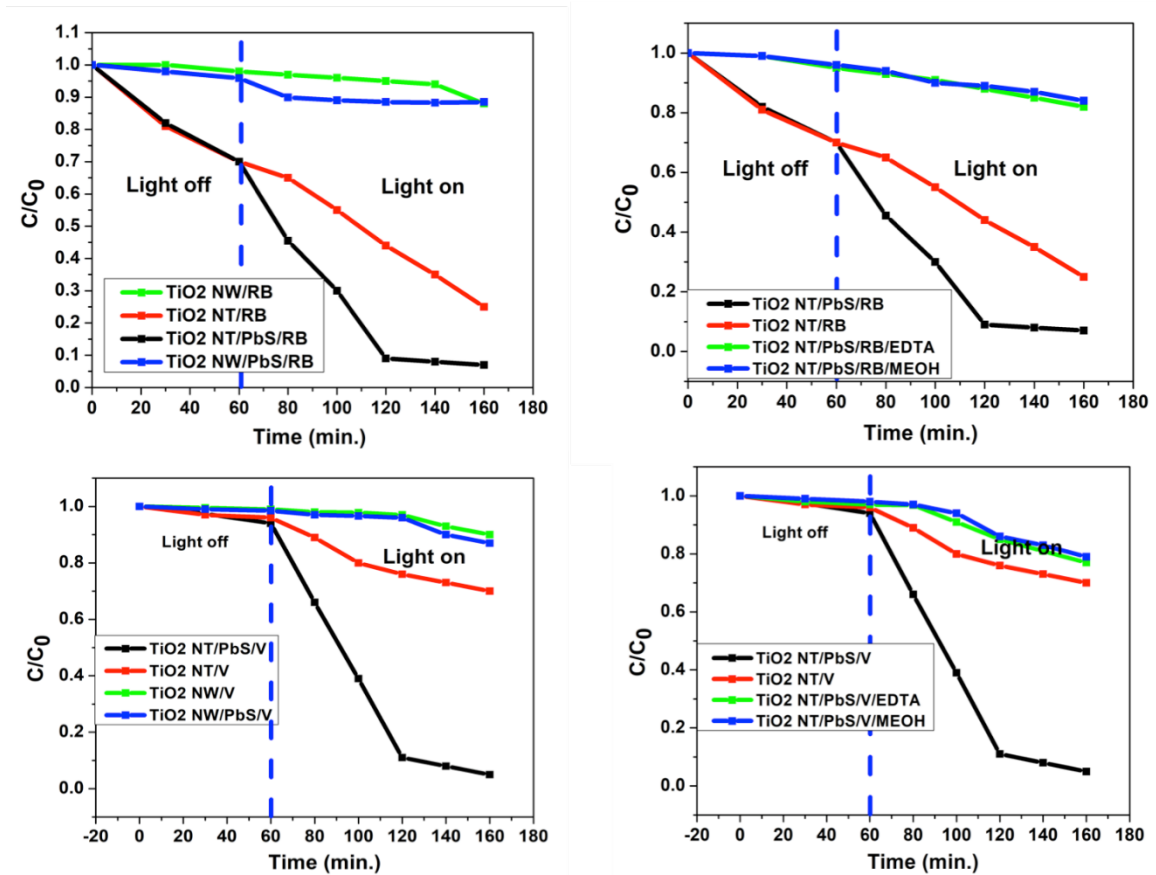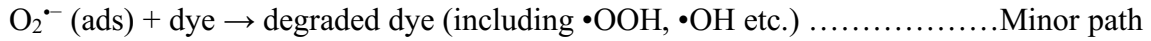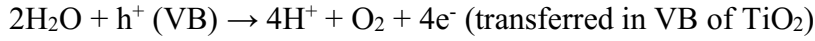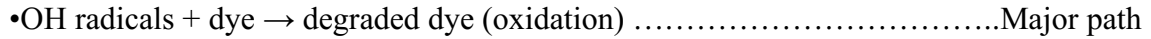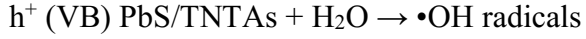
Figure 4. 8 Photocatalytic degradation of RhB and CV as a function of time using TiO_2 NT/PbS, TiO_2 NW/PbS, and TiO_2 NT/PbS in the presence of MeOH, EDTA scavenger.

4.3 Conclusion

The present chapter demonstrates successful deposition of PbS quantum dots on the TiO_2 nanotubes and nanowire structures using SILAR method. The SILAR approach gives a uniform coating of PbS quantum dots all over the 1D nanotubes and nanowire structure. The prepared PbS nanotubes and nanowire heterostructures were characterized with various tools to validate the presence of quantum dots. SEM showing agglomerated nanoparticles were deposited on the nanotubes in a uniform manner. The XRD characterization of materials didn't gave any signature peak of PbS which was attributed due the vary thin film of PbS quantum dots and most of the signal comes from the underlying TiO_2 substrate. UV-Vis clearly demonstrate the increase in visible light absorption profile of materials all over the visible range. UPS WF spectra show that the WF of PbS/TNTAs was reduced slightly comparing to pristine TiO_2 nanotube which was corroborated due to the uplifting of Fermi level. Further, the position of valence band was found to be 3.17 eV below the Fermi level and depicts oxidative valance band needed for efficient dye degradation. KPFM data support successful charge generation and migration at 450 nm for PbS/TNWAs which PbS/TNTAs structure show better charge transport dyenamic even at 635 nm. The applicability of developed PbS/TNTAs and PbS/TNWAs nanostructure was explored for the degradation of RhB and CV dyes which demonstrate excellent dye degradation performance of PbS/TNTAs nanostructures. The excellent performance of PbS/TNTAs nanostructures was assumed due to successful formation of heterojunction between PbS and anatase phase TiO_2 in nanotubes. Further, high surface area, better decoration of quantum dots on nanotubes structure was supposed to be responsible for the enhanced dye degradation performance. Scavenger test further

verified that hole was the main active species responsible for the dye degradation, which clearly demonstrate relevance of oxidative valance band. We believe finding in the present chapter will be of great importance to wide scientific audience to future development of more active and resilient heterostructure via benign process for pollutant degradation and environmental remediation.

Chapter 5 Summary and Future Work

In this thesis the background information, experimental methods, characterizations and application for different nanostructure of TiO_2, and their hierarchical structure are studied in detail.

In first part of this study, the novel hierarchical structure of TNTAs/TNWAs on Ti foil is fabricated by decorating TNWAs in and on top of electrochemically anodized TNTAs. The surface was modified by applying ODPA SAMs to adjust the materials wetting properties as hydrophobic. The hierarchical ODPA/TNWAs/TNTAs nanostructure presented superhydrophobic behavior. As the future work the developed heterostructure could be employed for environmental remediation and visible light driven photocatalysis.

Next, we presented the new fluoride-free solid-state method for TiO_2 nanotube preparation. The fabricated TNTAs presented similar morphological, crystalline feature and promising photocurrent response as for TiO_2 nanotubes grown in solution-based electrolyte. This environment-friendly method, which uses less toxic inorganic salts, is easy handling, processing and has a compact fabrication apparatus. The envisaged application of solid-state anodization process may lead to deployment of nontoxic environmental benign protocol for fabrication of TiO_2 nanotubes on compact surfaces. As the future work we will use the fabricated TiO_2 nanotube for dye degradation application to validate its promising photocatalytic behavior.

In last phase of this study the uniform coating of PbS quantum dots were grown on different nanostructures of TiO_2 by the SILAR method. The applicability of developed PbS/TNTAs and PbS/TNWAs nanostructure was explored for the RhB and CV dye

degradation, which presents great dye degradation performance of PbS/TNTAs nanostructures concluding better photocatalytic behavior in the junction of PbS/TNTAs. For future studies, we will optimize the solution temperature, adsorption, reaction and rinsing time to optimize the PbS growth by SILAR method to achieve higher photocatalytic dye degradation performance.

References

Chapter 1

1. Riyas, S., V.A. Yasir, and P.M. Das, Crystal structure transformation of TiO_2 in presence of Fe_2O_3 and NiO in air atmosphere. Bulletin of Materials Science, 2002. 25(4): p. 267-273.
2. Chen, X. and S.S. Mao, Titanium dioxide nanomaterials: synthesis, properties, modifications, and applications. Chemical reviews, 2007. 107(7): p. 2891-2959.
3. Zaleska, A., Doped-TiO_2: a review. Recent patents on engineering, 2008. 2(3): p. 157-164.
4. Roy, P., S. Berger, and P. Schmuki, TiO_2 nanotubes: synthesis and applications. Angewandte Chemie International Edition, 2011. 50(13): p. 2904-2939.
5. González, A.J. and S.G. Santiago, Structural and optoelectronic characterization of TiO_2 films prepared using the sol–gel technique. Semiconductor science and technology, 2007. 22(7): p. 709.
6. Welte, A., et al., Application of optical absorbance for the investigation of electronic and structural properties of sol–gel processed TiO_2 films. Thin Solid Films, 2008. 516(20): p. 7256-7259.
7. Singh, M., et al., Sol gel spin coated TiO_2 films for transparent window applications. Journal of Optoelectronics and Advanced Materials, 2012. 14(7): p. 624.
8. Landmann, M., E. Rauls, and W. Schmidt, The electronic structure and optical response of rutile, anatase and brookite TiO_2. Journal of physics: condensed matter, 2012. 24(19): p. 195503.
9. Könenkamp, R., P. Hoyer, and A. Wahi, Heterojunctions and devices of colloidal semiconductor films and quantum dots. Journal of applied physics, 1996. 79(9): p. 7029-7035.
10. Ji, Y., heoretical Studies on the MolecularMechanisms of Photo-Catalytic Reactions on TiO2 Surfaces. 2014, Royal Institute of Technology Stockholm. p. 82.
11. Li, J.G., et al., Monodispersed Spherical Particles of Brookite‐Type TiO_2: Synthesis, Characterization, and Photocatalytic Property. Journal of the American Ceramic Society, 2004. 87(7): p. 1358-1361.
12. Sankar, S. and K. Gopchandran, Effect of annealing on the structural, electrical and optical properties of nanostructured TiO_2 thin films. Crystal Research and Technology: Journal of Experimental and Industrial Crystallography, 2009. 44(9): p. 989-994.
13. Hossein-Babaei, F., et al., A resistive gas sensor based on undoped p-type anatase. Sensors and Actuators B: Chemical, 2005. 110(1): p. 28-35.
14. Jiang, K.-J., et al., Dye-sensitized solar cells using brookite nanoparticle TiO2 films as electrodes. Chemistry letters, 2002. 31(9): p. 872-873.

15. Francioso, L., et al., Automotive application of sol–gel TiO$_2$ thin film-based sensor for lambda measurement. Sensors and Actuators B: Chemical, 2003. 95(1-3): p. 66-72.

16. Ao, C., et al., Photodegradation of formaldehyde by photocatalyst TiO$_2$: effects on the presences of NO, SO$_2$ and VOCs. Applied catalysis B: environmental, 2004. 54(1): p. 41-50.

17. Yu, J., et al., Effects of calcination temperature on the photocatalytic activity and photo-induced super-hydrophilicity of mesoporous TiO$_2$ thin films. New Journal of Chemistry, 2002. 26(5): p. 607-613.

18. Hsien, Y.-H., et al., Photodegradation of aromatic pollutants in water over TiO$_2$ supported on molecular sieves. Applied Catalysis B: Environmental, 2001. 31(4): p. 241-249.

19. Carp, O., C.L. Huisman, and A. Reller, Photoinduced reactivity of titanium dioxide. Progress in solid state chemistry, 2004. 32(1-2): p. 33-177.

20. Li, P., et al., The role of hydrated silica, titania, and alumina in inducing apatite on implants. Journal of biomedical materials research, 1994. 28(1): p. 7-15.

21. Han, Y., S.-H. Hong, and K. Xu, Synthesis of nanocrystalline titania films by micro-arc oxidation. Materials Letters, 2002. 56(5): p. 744-747.

22. Tobaldi, D., et al., Nanosized titania modified with tungsten and silver: Microstructural characterisation of a multifunctional material. Applied Surface Science, 2013. 287: p. 276-281.

23. Zhou, X., et al., Hydrothermal fabrication of Ti^{3+} self-doped TiO$_2$ nanorods with high visible light photocatalytic activity. Materials Letters, 2013. 112: p. 145-148.

24. Kiran, V. and S. Sampath, Facile synthesis of carbon doped TiO$_2$ nanowires without an external carbon source and their opto-electronic properties. Nanoscale, 2013. 5(21): p. 10646-10652.

25. Nam, C.T., W.-D. Yang, and D. Le Minh, Study on photocatalysis of TiO$_2$ nanotubes prepared by methanol-thermal synthesis at low temperature. Bulletin of Materials Science, 2013. 36(5): p. 779-788.

26. Wang, Y., et al., Path-directed and maskless fabrication of ordered TiO$_2$ nanoribbons. Nanoscale, 2012. 4(5): p. 1545-1548.

27. Chen, J., et al., Role of one-dimensional ribbonlike nanostructures in dye-sensitized TiO$_2$-based solar cells. The Journal of Physical Chemistry C, 2011. 115(14): p. 7104-7113.

28. Murakoshi, K., et al., Fabrication of solid-state dye-sensitized TiO$_2$ solar cells combined with polypyrrole. Solar Energy Materials and Solar Cells, 1998. 55(1-2): p. 113-125.

29. Lu, J., Solution precursor chemical vapor deposition of titanium oxide thin films. Thin Solid Films, 1991. 204: p. L13-L17.

30. Nabavi, M., et al., Sol-gel synthesis of electrochromic films. Materials Science and Engineering: B, 1989. 3(1-2): p. 203-207.

31. Morris, H.B., Method of depositing titanium dioxide (rutile) as a gate dielectric for MIS device fabrication. 1980, Google Patents.

32. Schiller, S., et al., Influence of deposition parameters on the optical and structural properties of TiO$_2$ films produced by reactive dc plasmatron sputtering. Thin Solid Films, 1981. 83(2): p. 239-245.

33.   Suhail, M., G.M. Rao, and S. Mohan, dc reactive magnetron sputtering of titanium ‐ structural and optical characterization of TiO_2 films. Journal of Applied Physics, 1992. 71(3): p. 1421-1427.

34.   Lottiaux, M., et al., Morphology and structure of TiO_2 thin layers vs. thickness and substrate temperature. Thin solid films, 1989. 170(1): p. 107-126.

35.   Schroder, H., Physics of Thin Films: Advances in Research and Developments 5, edited by G. Hass and RE Thun. 1969, Academic Press, New-York.

36.   Heald, E.F. and C.W. Weiss, Kinetics and mechanism of anatase/rutile transformation, as catalyzed by ferric oxide and reducing conditions. American Mineralogist, 1972. 57(1-2): p. 10-&.

37.   Zhang, H. and J.F. Banfield, New kinetic model for the nanocrystalline anatase-to-rutile transformation revealing rate dependence on number of particles. American Mineralogist, 1999. 84(4): p. 528-535.

38.   Li, W., et al., Size dependence of thermal stability of TiO_2 nanoparticles. Journal of Applied Physics, 2004. 96(11): p. 6663-6668.

39.   Kominami, H., M. Kohno, and Y. Kera, Synthesis of brookite-type titanium oxide nano-crystals in organic media. Journal of Materials chemistry, 2000. 10(5): p. 1151-1156.

40.   Ye, X., et al., Thermoanalytical characteristic of nanocrystalline brookite-based titanium dioxide. Nanostructured materials, 1997. 8(7): p. 919-927.

41.   Chen, C.-J. and J.-M. Wu, The effect of niobium, calcium and lanthanum dopants on the crystallite growth of TiO_2 powders. Materials Science and Engineering: B, 1990. 5(3): p. 377-383.

42.   Cheng, P., et al., Preparation and characterization of silica-doped titania photocatalyst through sol–gel method. Materials Letters, 2003. 57(20): p. 2989-2994.

43.   Xiong, G., et al., Preparation and Characterization of Al_2O_3–TiO_2 Composite Oxide Nanocrystals. Journal of Solid State Chemistry, 1998. 141(1): p. 70-77.

44.   Calleja, G., et al., Mesostructured SiO_2-doped TiO_2 with enhanced thermal stability prepared by a soft-templating sol–gel route. Microporous and Mesoporous Materials, 2008. 111(1-3): p. 429-440.

45.   Yasir, V.A., P. MohanDas, and K. Yusuff, Preparation of high surface area TiO_2 (anatase) by thermal hydrolysis of titanyl sulphate solution. International Journal of Inorganic Materials, 2001. 3(7): p. 593-596.

46.   Reyes-Coronado, D., et al., Phase-pure TiO_2 nanoparticles: anatase, brookite and rutile. Nanotechnology, 2008. 19(14): p. 145605.

47.   Swamy, V., et al., Finite-size and pressure effects on the Raman spectrum of nanocrystalline anatase TiO_2. Physical Review B, 2005. 71(18): p. 184302.

48.   Han, H. and R. Bai, Buoyant photocatalyst with greatly enhanced visible-light activity prepared through a low temperature hydrothermal method. Industrial & Engineering Chemistry Research, 2009. 48(6): p. 2891-2898.

49.   Diebold, U., The surface science of titanium dioxide. Surface science reports, 2003. 48(5-8): p. 53-229.

50.   Thompson, T.L. and J.T. Yates, Surface science studies of the photoactivation of TiO2 new photochemical processes. Chemical Reviews, 2006. 106(10): p. 4428-4453.

51. Jones, A.C. and P.R. Chalker, Some recent developments in the chemical vapour deposition of electroceramic oxides. Journal of Physics D: Applied Physics, 2003. 36(6): p. R80.

52. Sakka, S., The Outline of Applications of the Sol–Gel Method. Handbook of Sol-Gel Science and Technology, 2016: p. 1-33.

53. Cushing, B.L., V.L. Kolesnichenko, and C.J. O'Connor, Recent advances in the liquid-phase syntheses of inorganic nanoparticles. Chemical reviews, 2004. 104(9): p. 3893-3946.

54. Pathan, H. and C. Lokhande, Deposition of metal chalcogenide thin films by successive ionic layer adsorption and reaction (SILAR) method. Bulletin of Materials Science, 2004. 27(2): p. 85-111.

55. Nicolau, Y., M. Dupuy, and M. Brunel, ZnS, CdS, and $Zn_{1-x}Cd_xS$ thin films deposited by the successive ionic layer adsorption and reaction process. Journal of the Electrochemical Society, 1990. 137(9): p. 2915-2924.

Chapter 2

1. Suhail, M., G.M. Rao, and S. Mohan, dc reactive magnetron sputtering of titanium structural and optical characterization of TiO2 films. Journal of Applied Physics, 1992. 71(3): p. 1421-1427.

2. Pulker, H. and H. Pulker, Coatings on glass. Vol. 20. 1999: Elsevier.

3. Kulkarni, M., et al., Titanium nanostructures for biomedical applications. Nanotechnology, 2015. 26(6): p. 062002.

4. Shankar, K., TiO 2 Nanotube Arrays: Growth and Application, in Encyclopedia of Nanotechnology. 2012, Springer. p. 2742-2755.

5. Hosseini, A., et al., Radial Heterojunction Solar Cell Consisting of n-Type Rutile Nanowire Arrays Infiltrated by p-Type CdTe. Journal of Nanoscience and Nanotechnology, 2017. 17(7): p. 5119-5123.

6. Kim, S.W., et al., Wetting and Photocatalytic Properties of TiO2 Nanotube Arrays Prepared via Anodic Oxidation of E-Beam Evaporated Ti Thin Films. International Journal of Photoenergy, 2015. 2015.

7. Ottone, C., et al., Wetting behavior of hierarchical oxide nanostructures: TiO2 nanotubes from anodic oxidation decorated with ZnO nanostructures. Journal of The Electrochemical Society, 2014. 161(10): p. D484-D488.

8. Mohammadpour, A., et al., Majority carrier transport in single crystal rutile nanowire arrays. physica status solidi (RRL)–Rapid Research Letters, 2014. 8(6): p. 512-516.

9. Xi, J. and L. Jiang, Biomimic superhydrophobic surface with high adhesive forces. Industrial & Engineering Chemistry Research, 2008. 47(17): p. 6354-6357.

10. Barthlott, W. and C. Neinhuis, Purity of the sacred lotus, or escape from contamination in biological surfaces. Planta, 1997. 202(1): p. 1-8.

11.   Shen, Y., et al., Nanostructures in superhydrophobic Ti6Al4V hierarchical surfaces control wetting state transitions. Soft Matter, 2015. 11(19): p. 3806-3811.

12.   Ma, M. and R.M. Hill, Superhydrophobic surfaces. Current opinion in colloid & interface science, 2006. 11(4): p. 193-202.

13.   Chen, Y., et al., Transparent superhydrophobic/superhydrophilic coatings for self-cleaning and anti-fogging. Applied Physics Letters, 2012. 101(3): p. 033701.

14.   Chen, Y., et al., Fabrication and anti‐corrosion property of superhydrophobic hybrid film on copper surface and its formation mechanism. Surface and Interface Analysis: An International Journal devoted to the development and application of techniques for the analysis of surfaces, interfaces and thin films, 2009. 41(11): p. 872-877.

15.   Boinovich, L.B. and A.M. Emelyanenko, Anti-icing potential of superhydrophobic coatings. Mendeleev Communications, 2013. 1(23): p. 3-10.

16.   Wenzel, R.N., Resistance of solid surfaces to wetting by water. Industrial & Engineering Chemistry, 1936. 28(8): p. 988-994.

17.   Pfleging, W., et al., Control of wettability of hydrogenated amorphous carbon thin films by laser-assisted micro-and nanostructuring. Applied Surface Science, 2011. 257(18): p. 7907-7912.

18.   Wang, R., et al., Light-induced amphiphilic surfaces. Nature, 1997. 388(6641): p. 431.

19.   Lai, Y., et al., Designing superhydrophobic porous nanostructures with tunable water adhesion. Advanced Materials, 2009. 21(37): p. 3799-3803.

20.   Shen, Y., et al., Icephobic/anti-icing potential of superhydrophobic Ti6Al4V surfaces with hierarchical textures. Rsc Advances, 2015. 5(3): p. 1666-1672.

21.   Passoni, L., et al., Multiscale effect of hierarchical self-assembled nanostructures on superhydrophobic surface. Langmuir, 2014. 30(45): p. 13581-13587.

22.   Boinovich, L., A.M. Emelyanenko, and A.S. Pashinin, Analysis of long-term durability of superhydrophobic properties under continuous contact with water. ACS applied materials & interfaces, 2010. 2(6): p. 1754-1758.

23.   Chu, C., et al., Micro-nano hierarchical porous titania modified with ZnO nanorods for biomedical applications. Surface and Coatings Technology, 2013. 232: p. 68-74.

24.   Lv, P., et al., Performance improvement by using ammonia water-synthesized TiO 2 nanotubes with nanowire porous film mixed nanostructures. Journal of Materials Chemistry A, 2015. 3(31): p. 16089-16096.

25.   Lin, Z., et al., Simple preparation of nanoporous few-layer nitrogen-doped graphene for use as an efficient electrocatalyst for oxygen reduction and oxygen evolution reactions. Carbon, 2013. 53: p. 130-136.

26.   Feng, X. and L. Jiang, Design and creation of superwetting/antiwetting surfaces. Advanced Materials, 2006. 18(23): p. 3063-3078.

27.   Shoute, L.C., et al., Threshold hydrophobicity for inhibition of salt scale formation on SAM-modified titania nanotube arrays. Applied Surface Science, 2019. 473: p. 282-290.

28.   Rosario, R., et al., Lotus effect amplifies light-induced contact angle switching. The Journal of Physical Chemistry B, 2004. 108(34): p. 12640-12642.

29.   Marmur, A., The lotus effect: superhydrophobicity and metastability. Langmuir, 2004. 20(9): p. 3517-3519.

30.   Tsujii, K., et al., Super oil‐repellent surfaces. Angewandte Chemie International Edition in English, 1997. 36(9): p. 1011-1012.

31.   Verplanck, N., et al., Wettability switching techniques on superhydrophobic surfaces. Nanoscale Research Letters, 2007. 2(12): p. 577.

32.   Kumar, P., R. Boukherroub, and K. Shankar, Sunlight-driven water-splitting using two dimensional carbon based semiconductors. Journal of Materials Chemistry A, 2018.

33.   Wetting, D.Q., Roughness. Annual Review of Materials Research, 2008. 38: p. 71-99.

34.   De Gennes, P.-G., Wetting: statics and dynamics. Reviews of modern physics, 1985. 57(3): p. 827.

35.   Berg, J.C., An introduction to interfaces & colloids: the bridge to nanoscience. 2010: World Scientific.

36.   Li, H., et al., Templated synthesis of TiO 2 nanotube macrostructures and their photocatalytic properties. Nano Research, 2015. 8(3): p. 900-906.

37.   Mor, G.K., et al., A review on highly ordered, vertically oriented TiO2 nanotube arrays: Fabrication, material properties, and solar energy applications. Solar Energy Materials and Solar Cells, 2006. 90(14): p. 2011-2075.

38.   Mor, G.K., et al., Transparent highly ordered TiO2 nanotube arrays via anodization of titanium thin films. Advanced Functional Materials, 2005. 15(8): p. 1291-1296.

39.   Prakasam, H.E., et al., A new benchmark for TiO2 nanotube array growth by anodization. The Journal of Physical Chemistry C, 2007. 111(20): p. 7235-7241.

40.   Roy, P., S. Berger, and P. Schmuki, TiO2 nanotubes: synthesis and applications. Angewandte Chemie International Edition, 2011. 50(13): p. 2904-2939.

41.   Macak, J.M., et al., TiO2 nanotubes: Self-organized electrochemical formation, properties and applications. Current Opinion in Solid State and Materials Science, 2007. 11(1-2): p. 3-18.

42.   Regonini, D., et al., Effect of heat treatment on the properties and structure of TiO2 nanotubes: phase composition and chemical composition. Surface and Interface Analysis: An International Journal devoted to the development and application of techniques for the analysis of surfaces, interfaces and thin films, 2010. 42(3): p. 139-144.

43.   Taveira, L., et al., Initiation and growth of self-organized TiO2 nanotubes anodically formed in NH4F/(NH4) 2SO4 electrolytes. Journal of the Electrochemical Society, 2005. 152(10): p. B405-B410.

44.   Thompson, G., et al., Anodic oxidation of aluminium. Philosophical Magazine B, 1987. 55(6): p. 651-667.

45.   Byrappa, K. and M. Yoshimura, 2 - History of Hydrothermal Technology, in Handbook of Hydrothermal Technology (Second Edition). 2013, William Andrew Publishing: Oxford. p. 51-73.

46.   Hosono, E., et al., Growth of submicrometer-scale rectangular parallelepiped rutile TiO2 films in aqueous TiCl3 solutions under hydrothermal conditions. Journal of the American Chemical Society, 2004. 126(25): p. 7790-7791.

47.   Weng, C.-C., K.-F. Hsu, and K.-H. Wei, Synthesis of arrayed, TiO2 needlelike nanostructures via a polystyrene-block-poly (4-vinylpyridine) diblock copolymer template. Chemistry of materials, 2004. 16(21): p. 4080-4086.

48.   Kakiuchi, K., et al., {111}-faceting of low-temperature processed rutile TiO 2 rods. Journal of crystal growth, 2006. 293(2): p. 541-545.

49.   Feng, X., J. Zhai, and L. Jiang, The fabrication and switchable superhydrophobicity of TiO2 nanorod films. Angewandte Chemie International Edition, 2005. 44(32): p. 5115-5118.

50.   Liu, B. and E.S. Aydil, Growth of oriented single-crystalline rutile TiO2 nanorods on transparent conducting substrates for dye-sensitized solar cells. Journal of the American Chemical Society, 2009. 131(11): p. 3985-3990.

51.   Kumar, A., A.R. Madaria, and C. Zhou, Growth of aligned single-crystalline rutile TiO2 nanowires on arbitrary substrates and their application in dye-sensitized solar cells. The Journal of Physical Chemistry C, 2010. 114(17): p. 7787-7792.

52.   Demazeau, G. Impact of high pressures in solvothermal processes. in Journal of Physics: Conference Series. 2010. IOP Publishing.

53.   Demazeau, G., Solvothermal and hydrothermal processes: the main physico-chemical factors involved and new trends. Research on Chemical Intermediates, 2011. 37(2-5): p. 107-123.

54.   Steele, A., I. Bayer, and E. Loth, Inherently superoleophobic nanocomposite coatings by spray atomization. Nano letters, 2008. 9(1): p. 501-505.

55.   Ulman, A., Formation and structure of self-assembled monolayers. Chemical reviews, 1996. 96(4): p. 1533-1554.

56.   Mekla, V., C. Juisuwannathat, and U. Tipparach. The Growth of TiO2 Nanostructures Prepared by Anodization in Combination with Hydrothermal Method on the Ti Foil. in MATEC Web of Conferences. 2015. EDP Sciences.

57.   Zhou, Q., et al., Rutile nanowire arrays: tunable surface densities, wettability and photochemistry. Journal of Materials Chemistry, 2011. 21(39): p. 15806-15812.

58.   Mohammadpour, A., et al., 100-fold improvement in carrier drift mobilities in alkanephosphonate-passivated monocrystalline TiO2 nanowire arrays. Nanotechnology, 2017. 28(14): p. 144001.

59.   Liu, G., K. Du, and K. Wang, Surface wettability of TiO2 nanotube arrays prepared by electrochemical anodization. Applied Surface Science, 2016. 388: p. 313-320.

60.   Tan, A., et al., Osteogenic potential of in situ TiO2 nanowire surfaces formed by thermal oxidation of titanium alloy substrate. Applied Surface Science, 2014. 320: p. 161-170.

61.   Watanabe, T., et al., Photocatalytic activity and photo-induced wettability conversion of TiO2 thin film prepared by sol-gel process on a soda-lime glass. Journal of Sol-Gel Science and Technology, 2000. 19(1-3): p. 71-76.

Chapter 3

1. Chu, S. and A. Majumdar, Opportunities and challenges for a sustainable energy future. Nature, 2012. 488(7411): p. 294.
2. Lewis, N.S. and D.G. Nocera, Powering the planet: Chemical challenges in solar energy utilization. Proceedings of the National Academy of Sciences, 2006. 103(43): p. 15729-15735.
3. Tachibana, Y., L. Vayssieres, and J.R. Durrant, Artificial photosynthesis for solar water-splitting. Nature Photonics, 2012. 6(8): p. 511.
4. Kudo, A. and Y. Miseki, Heterogeneous photocatalyst materials for water splitting. Chemical Society Reviews, 2009. 38(1): p. 253-278.
5. Walter, M.G., et al., Solar water splitting cells. Chemical Reviews, 2010. 110(11): p. 6446-6473.
6. Hunge, Y., A. Yadav, and V. Mathe, Ultrasound assisted synthesis of WO_3-ZnO nanocomposites for brilliant blue dye degradation. Ultrasonics sonochemistry, 2018. 45: p. 116-122.
7. Hunge, Y., A. Yadav, and V. Mathe, Oxidative degradation of phthalic acid using TiO_2 photocatalyst. Journal of Materials Science: Materials in Electronics, 2018. 29(8): p. 6183-6187.
8. Ali, T., Y.M. Hunge, and A. Venkatraman, UV assisted photoelectrocatalytic degradation of reactive red 152 dye using spray deposited TiO_2 thin films. Journal of Materials Science: Materials in Electronics, 2018. 29(2): p. 1209-1215.
9. Izumi, Y., Recent advances in the photocatalytic conversion of carbon dioxide to fuels with water and/or hydrogen using solar energy and beyond. Coordination Chemistry Reviews, 2013. 257(1): p. 171-186.
10. Kondratenko, E.V., et al., Status and perspectives of CO_2 conversion into fuels and chemicals by catalytic, photocatalytic and electrocatalytic processes. Energy & Environmental Science, 2013. 6(11): p. 3112-3135.
11. Habisreutinger, S.N., L. Schmidt‑Mende, and J.K. Stolarczyk, Photocatalytic reduction of CO_2 on TiO_2 and other semiconductors. Angewandte Chemie International Edition, 2013. 52(29): p. 7372-7408.
12. Tang, J., J.R. Durrant, and D.R. Klug, Mechanism of photocatalytic water splitting in TiO_2. Reaction of water with photoholes, importance of charge carrier dynamics, and evidence for four-hole chemistry. Journal of the American Chemical Society, 2008. 130(42): p. 13885-13891.
13. Hunge, Y., et al., Degradation of organic dyes using spray deposited nanocrystalline stratified WO_3/TiO_2 photoelectrodes under sunlight illumination. Optical Materials, 2018. 76: p. 260-270.
14. Kumar, P., et al., A novel Ru/TiO_2 hybrid nanocomposite catalyzed photoreduction of CO_2 to methanol under visible light. Nanoscale, 2015. 7(37): p. 15258-15267.
15. Park, J.H., S. Kim, and A.J. Bard, Novel carbon-doped TiO_2 nanotube arrays with high aspect ratios for efficient solar water splitting. Nano Letters, 2006. 6(1): p. 24-28.

16.   Ge, M., et al., One‑dimensional TiO$_2$ Nanotube Photocatalysts for Solar Water Splitting. Advanced Science, 2017. 4(1): p. 1600152.

17.   Cho, I.S., et al., Highly efficient solar water splitting from transferred TiO$_2$ nanotube arrays. Nano Letters, 2015. 15(9): p. 5709-5715.

18.   Roy, P., S. Berger, and P. Schmuki, TiO$_2$ nanotubes: synthesis and applications. Angewandte Chemie International Edition, 2011. 50(13): p. 2904-2939.

19.   Chen, H.M., et al., Nano-architecture and material designs for water splitting photoelectrodes. Chemical Society Reviews, 2012. 41(17): p. 5654-5671.

20.   Gong, D., et al., Titanium oxide nanotube arrays prepared by anodic oxidation. Journal of Materials Research, 2001. 16(12): p. 3331-3334.

21.   Roy, P., S. Berger, and P. Schmuki, TiO$_2$ Nanotubes: Synthesis and Applications. Angewandte Chemie-International Edition, 2011. 50(13): p. 2904-2939.

22.   Albu, S.P., et al., Self-organized, free-standing TiO$_2$ nanotube membrane for flow-through photocatalytic applications. Nano Letters, 2007. 7(5): p. 1286-1289.

23.   Galstyan, V., et al., TiO$_2$ nanotubular and nanoporous arrays by electrochemical anodization on different substrates. RSC Advances, 2011. 1(6): p. 1038-1044.

24.   Farsinezhad, S., et al., Transparent Anodic TiO$_2$ Nanotube Arrays on Plastic Substrates for Disposable Biosensors and Flexible Electronics. Journal of Nanoscience and Nanotechnology, 2013. 13(4): p. 2885-2891.

25.   Mun, K.S., et al., A Stable, Label-free Optical Interferometric Biosensor Based on TiO$_2$ Nanotube Arrays. ACS Nano, 2010. 4(4): p. 2070-2076.

26.   Lin, J., K. Liu, and X.F. Chen, Synthesis of Periodically Structured Titania Nanotube Films and Their Potential for Photonic Applications. Small, 2011. 7(13): p. 1784-1789.

27.   Zou, J.P., et al., Ultraviolet Photodetectors Based on Anodic TiO$_2$ Nanotube Arrays. Journal of Physical Chemistry C, 2010. 114(24): p. 10725-10729.

28.   Galstyan, V., et al., TiO$_2$ Nanotubes: Recent Advances in Synthesis and Gas Sensing Properties. Sensors, 2013. 13(11): p. 14813-14838.

29.   Farsinezhad, S., H. Sharma, and K. Shankar, Interfacial band alignment for photocatalytic charge separation in TiO$_2$ nanotube arrays coated with CuPt nanoparticles. Physical Chemistry Chemical Physics, 2015. 17(44): p. 29723-29733.

30.   Zarifi, M.H., et al., Selective microwave sensors exploiting the interaction of analytes with trap states in TiO$_2$ nanotube arrays. Nanoscale, 2016. 8(14): p. 7466-7473.

31.   Qin, P., et al., Stable and Efficient Perovskite Solar Cells Based on Titania Nanotube Arrays. Small, 2015. 11(41): p. 5533-5539.

32.   Kim, S., et al., Broad Spectrum Light Harvesting in TiO$_2$ Nanotube Array - Hemicyanine Dye - P3HT Hybrid Solid-State Solar Cells. IEEE Journal of Selected Topics in Quantum Electronics, 2010. 16(6): p. 1573-1580.

33.   Yip, C.T., et al., Direct and Seamless Coupling of TiO$_2$ Nanotube Photonic Crystal to Dye-Sensitized Solar Cell: A Single-Step Approach. Advanced Materials (Weinheim, Germany), 2011. 23(47): p. 5624-+.

34.   Kar, P., et al., Enhanced CH$_4$ yield by photocatalytic CO$_2$ reduction using TiO$_2$ nanotube arrays grafted with Au, Ru, and ZnPd nanoparticles. Nano Research, 2016. 9(11): p. 3478-3493.

35. Kongkanand, A., et al., Quantum dot solar cells. Tuning photoresponse through size and shape control of CdSe-TiO$_2$ architecture. Journal of the American Chemical Society, 2008. 130(12): p. 4007-4015.

36. Paulose, M., et al., TiO$_2$ nanotube arrays of 1000 μm length by anodization of titanium foil: Phenol red diffusion. Journal of Physical Chemistry C, 2007. 111(41): p. 14992-14997.

37. Popat, K.C., et al., Titania nanotubes: A novel platform for drug-eluting coatings for medical implants? Small, 2007. 3(11): p. 1878-1881.

38. Oh, S., et al., Stem cell fate dictated solely by altered nanotube dimension. Proceedings of the National Academy of Sciences of the United States of America, 2009. 106(7): p. 2130-2135.

39. Wang, N., et al., Effects of TiO$_2$ nanotubes with different diameters on gene expression and osseointegration of implants in minipigs. Biomaterials, 2011. 32(29): p. 6900-6911.

40. Mor, G.K., et al., Transparent highly ordered TiO$_2$ nanotube arrays via anodization of titanium thin films. Advanced Functional Materials, 2005. 15(8): p. 1291-1296.

41. Prakasam, H.E., et al., A New Benchmark for TiO$_2$ Nanotube Array Growth by Anodization. The Journal of Physical Chemistry C, 2007. 111(20): p. 7235-7241.

42. Kanbara, T., M. Inami, and T. Yamamoto, New solid-state electric double-layer capacitor using poly(vinyl alcohol)-based polymer solid electrolyte. Journal of Power Sources, 1991. 36(1): p. 87-93.

43. De Paoli, M.A., et al., All polymeric solid state electrochromic devices. Electrochimica Acta, 1999. 44(18): p. 2983-2991.

44. Stergiopoulos, T., et al., Binary polyethylene oxide/titania solid-state redox electrolyte for highly efficient nanocrystalline TiO$_2$ photoelectrochemical cells. Nano Letters, 2002. 2(11): p. 1259-1261.

45. Rajendran, S., M. Sivakumar, and R. Subadevi, Li-ion conduction of plasticized PVA solid polymer electrolytes complexed with various lithium salts. Solid State Ionics, 2004. 167(3): p. 335-339.

46. Zhu, Z., et al., All-solid-state lithium organic battery with composite polymer electrolyte and pillar [5] quinone cathode. Journal of the American Chemical Society, 2014. 136(47): p. 16461-16464.

47. Zhou, H., T. Fan, and D. Zhang, An insight into artificial leaves for sustainable energy inspired by natural photosynthesis. ChemCatChem, 2011. 3(3): p. 513-528.

48. Chemisana, D., Building integrated concentrating photovoltaics: a review. Renewable and Sustainable Snergy Reviews, 2011. 15(1): p. 603-611.

49. El Chaar, L. and N. El Zein, Review of photovoltaic technologies. Renewable and Sustainable Energy Reviews, 2011. 15(5): p. 2165-2175.

50. Montoya, J.H., et al., Materials for solar fuels and chemicals. Nature Materials, 2017. 16(1): p. 70.

51. Fujishima, A. and K. Honda, Electrochemical photolysis of water at a semiconductor electrode. Nature, 1972. 238(5358): p. 37.

52. Nozik, A.J. and M.D. Archer, Nanostructured and Photoelectrochemical Systems for Solar Photon Conversion. 2008: Imperial College Press.

53.   Memming, R., Semiconductor Electrochemistry. 2001. Weinheim: Wiley-VCH.

54.   Vayssieres, L., On solar hydrogen and nanotechnology. 2010: John Wiley & Sons.

55.   Bak, T., et al., Photo-electrochemical hydrogen generation from water using solar energy. Materials-related aspects. International Journal of Hydrogen Energy, 2002. 27(10): p. 991-1022.

56.   Grätzel, M., Photoelectrochemical cells. Nature, 2001. 414(6861): p. 338.

57.   Kumar, P., R. Boukherroub, and K. Shankar, Sunlight-driven water-splitting using two dimensional carbon based semiconductors. Journal of Materials Chemistry A, 2018.

58.   Subbaraman, R., et al., Trends in activity for the water electrolyser reactions on 3d M (Ni, Co, Fe, Mn) hydr (oxy) oxide catalysts. Nature Materials, 2012. 11(6): p. 550.

59.   Mirzakulova, E., et al., Electrode-assisted catalytic water oxidation by a flavin derivative. Nature Chemistry, 2012. 4(10): p. 794.

60.   Murdoch, M., et al., The effect of gold loading and particle size on photocatalytic hydrogen production from ethanol over Au/TiO_2 nanoparticles. Nature Chemistry, 2011. 3(6): p. 489.

61.   Mohammadpour, A., et al., 100-fold improvement in carrier drift mobilities in alkanephosphonate-passivated monocrystalline TiO_2 nanowire arrays. Nanotechnology, 2017. 28(14): p. 144001.

62.   Warren, E.L., H.A. Atwater, and N.S. Lewis, Silicon microwire arrays for solar energy-conversion applications. The Journal of Physical Chemistry C, 2013. 118(2): p. 747-759.

63.   Maeda, K., Z-scheme water splitting using two different semiconductor photocatalysts. ACS Catalysis, 2013. 3(7): p. 1486-1503.

64.   Rui, Y., et al., In-situ construction of three-dimensional titania network on Ti foil toward enhanced performance of flexible dye-sensitized solar cells. Applied Surface Science, 2016. 380: p. 210-217.

65.   Almeida, L.C. and M.V. Zanoni, Decoration of Ti/TiO_2 nanotubes with Pt nanoparticles for enhanced UV-Vis light absorption in photoelectrocatalytic process. Journal of the Brazilian Chemical Society, 2014. 25(3): p. 579-588.

66.   Yeniyol, S., et al., Antibacterial activity of As-annealed TiO_2 nanotubes doped with Ag nanoparticles against periodontal pathogens. Bioinorganic chemistry and applications, 2014. 2014.

67.   Mohammadpour, A., Synthesis and Characterization of TiO_2 Nanowire and Nanotube Arrays for Increased Optoelectronic Functionality. 2014, University of Alberta.

68.   Chen, X., et al., Formation of Oxynitride as the Photocatalytic Enhancing Site in Nitrogen‐Doped Titania Nanocatalysts: Comparison to a Commercial Nanopowder. Advanced Functional Materials, 2005. 15(1): p. 41-49.

69.   Wang, H., Y. Wu, and B.-Q. Xu, Preparation and characterization of nanosized anatase TiO_2 cuboids for photocatalysis. Applied Catalysis B: Environmental, 2005. 59(3): p. 139-146.

70.   Ohsaka, T., F. Izumi, and Y. Fujiki, Raman spectrum of anatase, TiO2. Journal of Raman spectroscopy, 1978. 7(6): p. 321-324.

71. Orendorz, A., et al., Phase transformation and particle growth in nanocrystalline anatase TiO_2 films analyzed by X-ray diffraction and Raman spectroscopy. Surface Science, 2007. 601(18): p. 4390-4394.

72. Fang, J., et al., Spectroscopic studies of interfacial structures of CeO_2–TiO_2 mixed oxides. Applied Surface Science, 2007. 253(22): p. 8952-8961.

73. Tian, F., et al., Raman spectroscopy: a new approach to measure the percentage of anatase TiO_2 exposed (001) facets. The Journal of Physical Chemistry C, 2012. 116(13): p. 7515-7519.

74. Mor, G.K., et al., A review on highly ordered, vertically oriented TiO_2 nanotube arrays: Fabrication, material properties, and solar energy applications. Solar Energy Materials and Solar Cells, 2006. 90(14): p. 2011-2075.

75. Farsinezhad, S., A.N. Dalrymple, and K. Shankar, Toward single-step anodic fabrication of monodisperse TiO_2 nanotube arrays on non-native substrates. physica status solidi (a), 2014. 211(5): p. 1113-1121.

76. Mohammadpour, A. and K. Shankar, Magnetic field- assisted electroless anodization: TiO_2 nanotube growth on discontinuous, patterned Ti films. Journal of Materials Chemistry A, 2014. 2(34): p. 13810-13816.

Chapter 4

1. Assadi, M.M., et al., Decolorization of textile wastewater by Phanerochaete chrysosporium. Desalination, 2001. 141(3): p. 331-336.

2. Kim, T.-H., et al., Decolorization of disperse and reactive dyes by continuous electrocoagulation process. Desalination, 2002. 150(2): p. 165-175.

3. Azbar, N., T. Yonar, and K. Kestioglu, Comparison of various advanced oxidation processes and chemical treatment methods for COD and color removal from a polyester and acetate fiber dyeing effluent. Chemosphere, 2004. 55(1): p. 35-43.

4. Haroun, M. and A. Idris, Treatment of textile wastewater with an anaerobic fluidized bed reactor. Desalination, 2009. 237(1-3): p. 357-366.

5. Pagga, U. and K. Taeger, Development of a method for adsorption of dyestuffs on activated sludge. Water Research, 1994. 28(5): p. 1051-1057.

6. Macak, J.M., et al., Self‐organized TiO2 nanotube layers as highly efficient photocatalysts. small, 2007. 3(2): p. 300-304.

7. Su, J., et al., Self-assembly graphitic carbon nitride quantum dots anchored on TiO2 nanotube arrays: An efficient heterojunction for pollutants degradation under solar light. Journal of hazardous materials, 2016. 316: p. 159-168.

8. Cai, J., J. Huang, and Y. Lai, 3D Au-decorated BiMoO 6 nanosheet/TiO 2 nanotube array heterostructure with enhanced UV and visible-light photocatalytic activity. Journal of Materials Chemistry A, 2017. 5(31): p. 16412-16421.

9. Zhang, Y., et al., Three‐Dimensional CdS–Titanate Composite Nanomaterials for Enhanced Visible‐Light‐Driven Hydrogen Evolution. Small, 2013. 9(7): p. 996-1002.

10. Ge, M., et al., One‑dimensional TiO2 Nanotube Photocatalysts for Solar Water Splitting. Advanced Science, 2017. 4(1): p. 1600152.

11. Varghese, O.K., et al., Extreme changes in the electrical resistance of titania nanotubes with hydrogen exposure. Advanced Materials, 2003. 15(7‑8): p. 624-627.

12. Chiou, C.-S., et al., Degradation of di-n-butyl phthalate using photoreactor packed with TiO2 immobilized on glass beads. Journal of hazardous materials, 2006. 137(2): p. 1123-1129.

13. Achilleos, A., et al., Factors affecting diclofenac decomposition in water by UV-A/TiO2 photocatalysis. Chemical Engineering Journal, 2010. 161(1-2): p. 53-59.

14. Chen, J., et al., Photocatalyzed oxidation of alcohols and organochlorides in the presence of native TiO2 and metallized TiO2 suspensions. Part (I): photocatalytic activity and pH influence. Water Research, 1999. 33(3): p. 661-668.

15. Linsebigler, A.L., G. Lu, and J.T. Yates Jr, Photocatalysis on TiO2 surfaces: principles, mechanisms, and selected results. Chemical reviews, 1995. 95(3): p. 735-758.

16. Liu, Z., et al., Highly ordered TiO2 nanotube arrays with controllable length for photoelectrocatalytic degradation of phenol. The Journal of Physical Chemistry C, 2008. 112(1): p. 253-259.

17. Tian, J., et al., 3D Bi2MoO6 nanosheet/TiO2 nanobelt heterostructure: enhanced photocatalytic activities and photoelectochemistry performance. ACS Catalysis, 2015. 5(8): p. 4530-4536.

18. Sopyan, I., et al., An efficient TiO2 thin-film photocatalyst: photocatalytic properties in gas-phase acetaldehyde degradation. Journal of Photochemistry and Photobiology A: Chemistry, 1996. 98(1-2): p. 79-86.

19. Arabatzis, I., et al., Silver-modified titanium dioxide thin films for efficient photodegradation of methyl orange. Applied Catalysis B: Environmental, 2003. 42(2): p. 187-201.

20. Rachel, A., M. Subrahmanyam, and P. Boule, Comparison of photocatalytic efficiencies of TiO2 in suspended and immobilised form for the photocatalytic degradation of nitrobenzenesulfonic acids. Applied Catalysis B: Environmental, 2002. 37(4): p. 301-308.

21. Gong, D., et al., Titanium oxide nanotube arrays prepared by anodic oxidation. Journal of Materials Research, 2001. 16(12): p. 3331-3334.

22. Macak, J.M., et al., TiO2 nanotubes: Self-organized electrochemical formation, properties and applications. Current Opinion in Solid State and Materials Science, 2007. 11(1-2): p. 3-18.

23. Roy, P., S. Berger, and P. Schmuki, TiO2 nanotubes: synthesis and applications. Angewandte Chemie International Edition, 2011. 50(13): p. 2904-2939.

24. Zhuang, H.-F., et al., Some critical structure factors of titanium oxide nanotube array in its photocatalytic activity. Environmental science & technology, 2007. 41(13): p. 4735-4740.

25. Smith, Y.R., A. Kar, and V. Subramanian, Investigation of physicochemical parameters that influence photocatalytic degradation of methyl orange over TiO2 nanotubes. Industrial & Engineering Chemistry Research, 2009. 48(23): p. 10268-10276.

26. Neppolian, B., et al., Solar light induced and TiO2 assisted degradation of textile dye reactive blue 4. Chemosphere, 2002. 46(8): p. 1173-1181.

27. Nogueira, R.F. and W.F. Jardim, Photodegradation of methylene blue: Using solar light and semiconductor (TiO2). Journal of chemical education, 1993. 70(10): p. 861.

28. Brahimi, R., et al., Improvement of eosin visible light degradation using PbS-sensititzed TiO2. Journal of Photochemistry and Photobiology A: Chemistry, 2008. 194(2-3): p. 173-180.

29. Kukovecz, Á., et al., Complex-assisted one-step synthesis of ion-exchangeable titanate nanotubes decorated with CdS nanoparticles. Chemical physics letters, 2005. 411(4-6): p. 445-449.

30. Preetha, K., et al., Effect of cationic precursor pH on optical and transport properties of SILAR deposited nano crystalline PbS thin films. Current Applied Physics, 2012. 12(1): p. 53-59.

31. Göde, F., et al., Synthesis, structural, optical, electrical and thermoluminescence properties of chemically deposited PbS thin films. Journal of Luminescence, 2014. 147: p. 41-48.

32. Nozik, A.J., Multiple exciton generation in semiconductor quantum dots. Chemical Physics Letters, 2008. 457(1-3): p. 3-11.

33. Karki, K., KJ Karki, JR Widom, J. Seibt, I. Moody, MC Lonergan, T. Pullerits, and AH Marcus, Nat. Commun. 5, 5869 (2014). Nat. Commun., 2014. 5: p. 5869.

34. McDonald, S.A., et al., Solution-processed PbS quantum dot infrared photodetectors and photovoltaics. Nature materials, 2005. 4(2): p. 138.

35. Jung, S.W., et al., Two-step annealed CdS/CdSe co-sensitizers for quantum dot-sensitized solar cells. Current applied physics, 2013. 13(7): p. 1532-1536.

36. Saloniemi, H., et al., Electrochemical quartz crystal microbalance study on cyclic electrodeposition of PbS thin-films. Thin Solid Films, 2001. 386(1): p. 32-40.

37. Nair, P. and M. Nair, PbS solar control coatings: safety, cost and optimisation. Journal of Physics D: Applied Physics, 1990. 23(2): p. 150.

38. Puišo, J., et al., Growth of PbS thin films on silicon substrate by SILAR technique. Thin Solid Films, 2002. 403: p. 457-461.

39. Kanniainen, T., et al., Growth of strongly orientated lead sulfide thin films by successive ionic layer adsorption and reaction (SILAR) technique. Journal of Materials Chemistry, 1996. 6(2): p. 161-164.

40. Nykänen, E., et al., Growth of PbS thin films from novel precursors by atomic layer epitaxy. Journal of Materials Chemistry, 1994. 4(9): p. 1409-1412.

41. Pawar, S., et al., Recent status of chemical bath deposited metal chalcogenide and metal oxide thin films. Current Applied Physics, 2011. 11(2): p. 117-161.

42. Jiao, S., et al., Surface engineering of PbS quantum dot sensitized solar cells with a conversion efficiency exceeding 7%. Journal of Materials Chemistry A, 2016. 4(19): p. 7214-7221.

43. Li, X., et al., Pre-synthesized monodisperse PbS quantum dots sensitized solar cells. Electrochimica Acta, 2014. 144: p. 71-75.

44. Jumabekov, A.N., et al., Passivation of PbS quantum dot surface with l-glutathione in solid-state quantum-dot-sensitized solar cells. ACS applied materials & interfaces, 2016. 8(7): p. 4600-4607.

45. Zhang, Z., et al., Combination of short-length TiO2 nanorod arrays and compact PbS quantum-dot thin films for efficient solid-state quantum-dot-sensitized solar cells. Applied Surface Science, 2017. 410: p. 8-13.

46. Heo, J.H., et al., Formation of uniform PbS quantum dots by a spin-assisted successive precipitation and anion exchange reaction process using PbX 2 (X= Br, I) and Na 2 S precursors. RSC Advances, 2017. 7(6): p. 3072-3077.

47. Khan, M.M., S.F. Adil, and A. Al-Mayouf, Metal oxides as photocatalysts. 2015, Elsevier.

48. Rehman, S., et al., Strategies of making TiO2 and ZnO visible light active. Journal of hazardous materials, 2009. 170(2-3): p. 560-569.

49. Fujishima, A. and K. Honda, Electrochemical photolysis of water at a semiconductor electrode. nature, 1972. 238(5358): p. 37.

50. Nakata, K. and A. Fujishima, TiO2 photocatalysis: Design and applications. Journal of photochemistry and photobiology C: Photochemistry Reviews, 2012. 13(3): p. 169-189.

51. Ganguly, A., et al., Oxide-based nanostructures for photocatalytic and electrocatalytic applications. CrystEngComm, 2015. 17(47): p. 8978-9001.

52. Fox, M.A. and M.T. Dulay, Heterogeneous photocatalysis. Chemical reviews, 1993. 93(1): p. 341-357.

53. Hoffmann, M.R., et al., Environmental applications of semiconductor photocatalysis. Chemical reviews, 1995. 95(1): p. 69-96.

54. Pathan, H. and C. Lokhande, Deposition of metal chalcogenide thin films by successive ionic layer adsorption and reaction (SILAR) method. Bulletin of Materials Science, 2004. 27(2): p. 85-111.

55. Nicolau, Y., M. Dupuy, and M. Brunel, ZnS, CdS, and Zn1− x Cd x S thin films deposited by the successive ionic layer adsorption and reaction process. Journal of the Electrochemical Society, 1990. 137(9): p. 2915-2924.

56. Patake, V. and C. Lokhande, Chemical synthesis of nano-porous ruthenium oxide (RuO2) thin films for supercapacitor application. Applied Surface Science, 2008. 254(9): p. 2820-2824.

57. Salunkhe, R., et al., Structural, electrical and optical studies of SILAR deposited cadmium oxide thin films: annealing effect. Materials Research Bulletin, 2009. 44(2): p. 364-368.

58. Leamy, H., Charge collection scanning electron microscopy. Journal of Applied Physics, 1982. 53(6): p. R51-R80.

59. Melitz, W., et al., Kelvin probe force microscopy and its application. Surface science reports, 2011. 66(1): p. 1-27.

60. Nonnenmacher, M., M. o'Boyle, and H.K. Wickramasinghe, Kelvin probe force microscopy. Applied physics letters, 1991. 58(25): p. 2921-2923.

61. Hallam, T., et al., A scanning Kelvin probe study of charge trapping in zone-cast pentacene thin film transistors. Nanotechnology, 2008. 20(2): p. 025203.

62. Clack, N.G., K. Salaita, and J.T. Groves, Electrostatic readout of DNA microarrays with charged microspheres. Nature biotechnology, 2008. 26(7): p. 825.

63. Hoppe, H., et al., Kelvin probe force microscopy study on conjugated polymer/fullerene bulk heterojunction organic solar cells. Nano letters, 2005. 5(2): p. 269-274.

64. Garcıa, R. and R. Perez, Dynamic atomic force microscopy methods. Surface science reports, 2002. 47(6-8): p. 197-301.

65. Glatzel, T., S. Sadewasser, and M.C. Lux-Steiner, Amplitude or frequency modulation-detection in Kelvin probe force microscopy. Applied surface science, 2003. 210(1-2): p. 84-89.

66. Zerweck, U., et al., Accuracy and resolution limits of Kelvin probe force microscopy. Physical Review B, 2005. 71(12): p. 125424.

67. Mohammadpour, A., Synthesis and Characterization of TiO2 Nanowire and Nanotube Arrays for Increased Optoelectronic Functionality. 2014.

68. Du, K., et al., PbS quantum dots sensitized TiO2 nanotubes for photocurrent enhancement. Journal of The Electrochemical Society, 2015. 162(10): p. E251-E257.

69. Matsuda, A., S. Sreekantan, and W. Krengvirat, Well-aligned TiO2 nanotube arrays for energy-related applications under solar irradiation. Journal of Asian Ceramic Societies, 2013. 1(3): p. 203-219.